POLITECNICO DI TORINO

Collegio di Ingegneria Chimica e dei Materiali

Master of science course in Materials Engineering

Master of science thesis

"An exploratory study of anodes for potassium batteries"

Supervisors:
Prof. Federico Bella
Dott. Daniele Versaci
Dott. Lucia Fagiolari

Candidate:

Federica Di Berardino

July 2021

Introduzione

Questo lavoro di tesi si colloca nell'ambito di ricerca sulle batterie al Potassio. Queste ultime rappresentano un'alternativa sempre più promettente alle batterie agli ioni di Litio, in particolare in tutti quegli ambiti dove l'energia specifica gravimetrica non è il fattore più importante (vd. l'accumulo energetico stazionario). Si è deciso quindi di seguire la trattazione nel seguente modo: il primo capitolo sarà un'introduzione allo scenario energetico per comprendere il ruolo delle batterie e le relative sfide. Il secondo capitolo rappresenta il corpo teorico del lavoro. In questo, è presente la descrizione del funzionamento del dispositivo e la presentazione dello stato dell'arte sui materiali con particolare attenzione per l'elettrodo anodico e l'elettrolita in quanto oggetti della ricerca sperimentale. Il terzo capitolo descrive la strumentazione usata e la procedura eseguita per realizzare gli elettrodi. A completare questo capitolo verranno indicate le varie prove eseguite con i relativi set-up. Il quarto capitolo infine, è il corpo sperimentale del lavoro: verranno infatti presentati i risultati ottenuti con relativa discussione. I capitoli suddetti verrano brevemente ripercorsi nelle sezioni seguenti così da fornire un quadro, seppur non esaustivo, del lavoro svolto.

La sempre crescente domanda di energia elettrica, coniugata all'esigenza di ridurre le emissioni rendono necessario un cambiamento: il passaggio da energie fossili ad energie rinnovabili è una delle vie percorribili per attuare il processo di decarbonizzazione. Nonostante i vantaggi in termini ecologici, le risorse rinnovabili rappresentano ancora una sfida per quanto riguarda la loro immissione e cooperazione con quella che è la rete preesistente: infatti il loro carattere intermittente, rende l'integrazione non sempre agevole. Al fine di ovviare a questa problematica i sistemi di accumulo risultano una valida strategia.
Attualmente, la tecnologia più usata è quella delle batterie agli ioni di litio. I vantaggi a livello tecnico sono molteplici: alta densità energetica, basso peso ed un elevato sviluppo industriale. Al contempo le risorse di litio non sono molte (si attesta che la presenza sulla crosta terrestre è del 0.0017%) ed estremamente localizzate nel globo: entrambi fattori che non ne rendono stabile l'approviggionamento ed i costi. Risulta quindi necessario trovare alternative valide che permettano la sostituzione, almeno in alcuni ambiti. Tra le varie alternative, il potassio presenta una densità energetica volumetrica subito inferiore a quella del litio (vd. Figura 1), risulta quindi un buon candidato per i sistemi di accumulo energetico. In aggiunta, il potassio pur avendo un raggio ionico maggiore, in soluzione presenta un raggio di Stokes minore, garantendo quindi una diffusione nell'elettrolita liquido molto elevata. In aggiunta, il potenziale K^+/K è più elevato rispetto alla coppia Na^+/Na. Rispetto al sodio ha il vantaggio di formare composti stabili quando intercala nella grafite. Tutti questi fattori concorrono a rendere le batterie al potassio un'alternativa valida al litio.

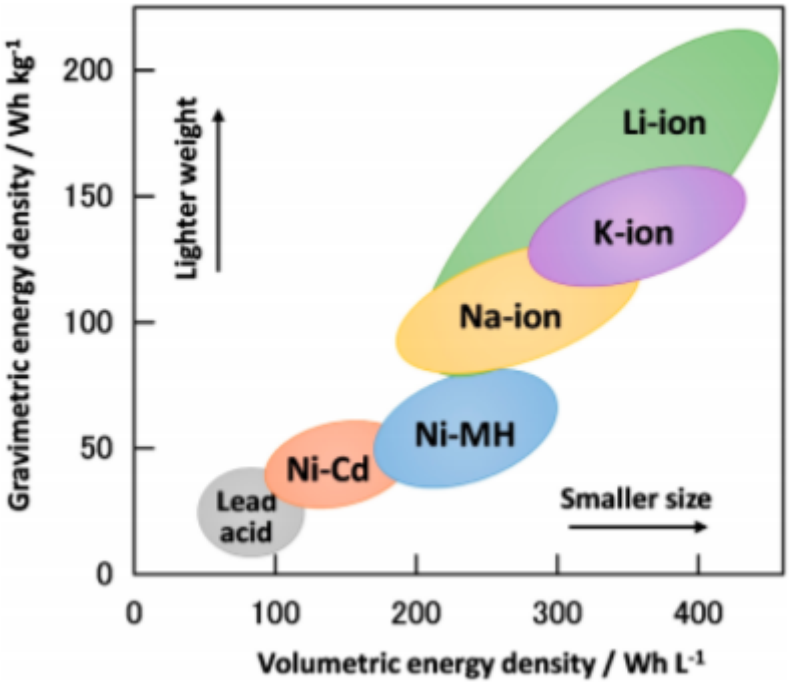

Figure 1: Comparazione di diversi sistemi di accumulo rispetto alla densità di energia gravimetrica e volumetrica

Una batteria è un dispositivo che si occupa della conversione, quasi reveresibile, di energia chimica in energia elettrica, (questo è vero se le batterie sono di tipo secondario cioè ricaricabili). Gli elementi cardini di questo sistema sono tre:

- Anodo;
- Catodo;
- Elettrolita.

Il meccanismo di funzionamento viene definito "rocking chair" perchè gli ioni potassio si muovono avanti ed indietro tra anodo e catodo durante il processo di carica/scarica come mostrato in Figura 2.

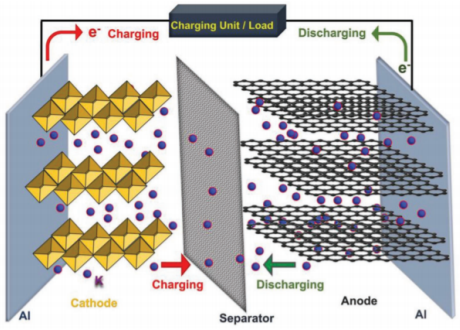

Figure 2: Schema di funzionamento di una batteria al potassio.

I materiali anodici vengono distinti in tre categorie che riflettono i meccanismi attraverso

cui il potassio viene accumulato. Ci sono quindi materiali ad intercalazione, conversione e per formazione di leghe. I primi sono costituiti da materiali con una struttura a strati tra i quali si va ad inserire lo ione. Questi sono ad esempio la grafite, i carboni amorfi, i dicalcogenuri metallici. Il raggio ionico più elevato fa sì che ci sia un'espansione notevole in ogni ciclo di intercalazione e de-intercalazione che porta ad una rapida degradazione del materiale. Varie strategie sono state adottate per limitare il fenomeno e garantire una stabilità alla ciclazione maggiore. Tra le varie alternative sono state utilizzate delle grafiti espanse o carboni amorfi che riescono più facilmente a tollerare l'espansione. I materiali che sfruttano reazioni di conversione sono ad esempio i dicalcogenuri metallici e gli ossidi, dove è possibile la reazione

$$MX + nK^+ + ne^- \rightarrow K_nX + M \tag{1}$$

dove M è un metallo di transizione ed X un non metallo (ad esempio O, S, Cl).
I materiali per formazione di lega invece possono legare con gli elementi del gruppo 14 e 15 (come Sb, Sn, P, Bi), attraverso una reazione reversibile che garantisce l'accumulo di potassio garantendo elevate capacità specifiche. La reazione attraverso cui avviene ciò è descritta di seguito

$$xA + yM^+ + ye^- \rightarrow A_xM_y \tag{2}$$

dove A è l'elemento legante ed M è il metallo alcalino dalla cui reazione si formano composti (A_xM_y). Questi materiali soffrono di espansioni elevatissime. Per questo sono necessarie strategie di controllo della struttura a livello di nanostruttura per evitare processi di polverizzazione.

Un altro componente fondamentale per il corretto funzionamento delle batterie è l'elettrolita. Questo è composto da un sale ed un solvente. I sali più comuni sono il KPF_6 ed il KFSI (che verranno studiati nella parte sperimentale). Per quanto riguarda i solventi si hanno molteplici possibilità. In questo lavoro sono stati usati solventi organici. Questi si dividono in carbonati ed eteri. Tra i primi ci sono il DEC, EC, PC; mentre nei secondi DME.
Un componente fondamentale che garantisce il corretto funzionamento del sistema è il SEI (interfase elettrolitica solida) ed è l'interfaccia che si viene a formare tra elettrodo anodico ed elettrolita. Ad oggi le ricerche relative al potassio sono ancora poche e si basano più sulla caratterizzazione morfologica che sul meccanismo di formazione e trasporto ionico. Come interfaccia infatti ha la caratteristica di permettere il passaggio degli ioni ma di isolare gli elettroni. La formazione del SEI dipende fortemente dalla scelta dell'elettrolita: l'utilizzo di KFSI in DME per esempio porta alla formazione al prodotto FSI^- che forma uno strato inorganico denso. Nel sistema con EC/DEC come solvente ci sono più reazioni di decomposizione che portano ad un SEI più spesso. Il lavoro sperimentale è stato svolto presso il DISAT nel gruppo di Elettrochimica. Il progetto si prefigge l'obiettivo di valutare le performance di diversi sistemi anodo-elettrolita.
In particolare si è iniziato con la fabbricazione degli elettrodi anodici. Questi sono costituiti di base da un materiale attivo, da un binder e da un materiale conduttivo. Il materiale attivo è quantitativamente e qualitativamente l'elemento fondamentale. Durante questa attività sono stati analizzati 4 differenti materiali attivi. Il binder è il componente che garantisce coesione e stabilità meccanica in quanto il materiale attivo si presenta sottoforma di polvere. Il materiale conduttivo invece serve a migliorare il passaggio di elettroni nel materiale attivo. Gli elettrodi vengono portati all'interno della camera in atmosfera

protetta (glovebox) dove sono assemblati. Le due configurazioni di celle utilizzate in questo lavoro sono le coin cell e le T-cell.

I sistemi analizzati in tutto sono 7, frutto della combinazione di 4 materiali attivi diversi con due differenti elettroliti. I materiali suddetti sono: la grafite, il disolfuro di molibdeno e due carboni non grafitici conosciuti con i nomi commerciali di SuperP e C45. Le composizioni in peso vengono presentate di seguito.

Materiale	Percentuale (%)
MoS_2	80
C45	10
CMC	10

Table 1: Composizione dell'elettrodo con MoS_2 come materiale attivo.

Materiale	Percentuale (%)
Graphite	90
C45	5
CMC	5

Table 2: Composizione dell'elettrodo con grafite come materiale attivo.

Materiale	Percentuale (%)
SuperP	80
PVDF	20

Table 3: Composizione dell'elettrodo con SuperP come materiale attivo.

Materiale	Percentuale (%)
C45	90
CMC	10

Table 4: Composizione dell'elettrodo con C45 come materiale attivo.

La scelta degli elettroliti invece ricade sul sistema KPF_6 0.8M in EC:DEC e KFSI 0.8M in DME. Le prime caratterizzazioni elettrochimiche sono state la ciclovoltammetria e cicli di carica-scarica. Questi test appartengono rispettivamente a test potenziostatici e galvanostatici. Nella ciclovoltammetria si applica un certo scan rate, mantenuto costante durante la prova; lo strumento misura quindi la corrente e il plot corrente vs. potenziale è conosciuto come voltammogramma. Da questo si possono ricavare informazioni circa la reversibilità delle reazioni, i potenziali a cui avvengono reazioni di ossido-riduzione e l'influenza dei parametri quali temperatura e scan rate. In questo contesto , le prove sono state effettuate ad uno scan rate fisso di 0.1 mV/s nel range 0.01-3V, quindi si è valutato il potenziale per le relative reazioni. La capacità specifica è stata invece testata con dei cicli di carica e scarica con varie condizioni di densità di corrente. Le informazioni ricavate

sono utili per correlare le performance alle diverese velocità e la stabilità alle ciclazioni. In base ai risultati ottenuti si è deciso di proseguire o meno: elettrodi con buone capacità sono stati quindi testati al fine di capire e il comportamento ad elevato numero di cicli e la formazione dell' interfaccia solida con l'elettrolita attraverso delle prove di impedenza elettrochimica (EIS).
Al fine di perseguire questo intento, nel primo caso si è impostato il programma di scarica a 0.1 A/g con numero di cicli pari a 500. Contemporaneamente per ricavare informazioni circa un'eventuale degradazione, ogni 100 cicli è stata svolta una prova EIS (tra 100kHz ed 10mHz con il potenziale di 0.1mV come input). Una volta effettuato il test, è stato utilizzato il software ZView per costruire il circuito equivalente e poter effettuare il fitting.
Inoltre analisi EIS sono state condotte per analizzare i fenomeni relativi ai primi cicli, durante i quali si realizza la formazione dell'interfaccia. Il set-up utilizzato prevede 10 cicli a 0.05 A/g intervallati da un EIS.
Per quanto riguarda caratterizzazioni morfologiche il FE-SEM è stato lo strumento principalmente utilizzato. Fatto questo preambolo, verranno qui di seguito mostrati i risultati ottenuti dalle varie prove.

Risultati

MoS_2+KFSI

Il sistema MoS_2 con l'elettrolita KFSI in DME ha pessime performance, non riuscendo a completare i cicli preposti. Dal voltammogramma si vede come la presenza di picchi cambia molto dal primo al secondo ciclo indice del fatto che i meccanismi coinvolti sono diversi. Nel primo si ha un picco a 0.8 V che può esser dovuto alla decomposizione del sale e alla formazione del SEI. Il picco a 0.11 V e quello a 0.01 V sono nel range del meccanismo di conversione. Nel corrispondente ciclo anodico si ha un picco poco definito a 1.4 V mentre uno molto definito ed esteso intorno a 2.3 V. In letteratura quest' ultimo è stato assegnato alla reazione di ossidazione. Andando ad esaminare la micrografia si nota la mancanza di coesione meccanica, evidenziata nella zona fratturata. Si nota inoltre che la superficie dell'elettrodo ciclato presenza delle differenze rispetto all'elettrodo non ciclato.

MoS_2+KPF_6

Il sistema testato con l'elettrolita KPF_6 in EC:DEC presenta performance migliori rispetto a quelle con il KFSI. I valori vengono presentati nella tabella (in particolare ci si riferisce ai valori in scarica al ciclo 15, 100 e 200) con la relativa CE (vd. in Appendice).

Cell	ma	D-cap 15	CE(%)	D-cap 100	CE(%)	D-cap 200	CE(%)
1	0.003371g	87.65	99.98	91.36	100	88.99	99.98
2	0.003211g	81.15	100	89	99.8	88.72	99.73
3	0.005211g	103.41	99.35	97.13	99.7	92.52	99.89

Table 5: Performance di tutte le celle testate nella prova di carica-scarica con relativa CE per MoS_2 con KPF_6.

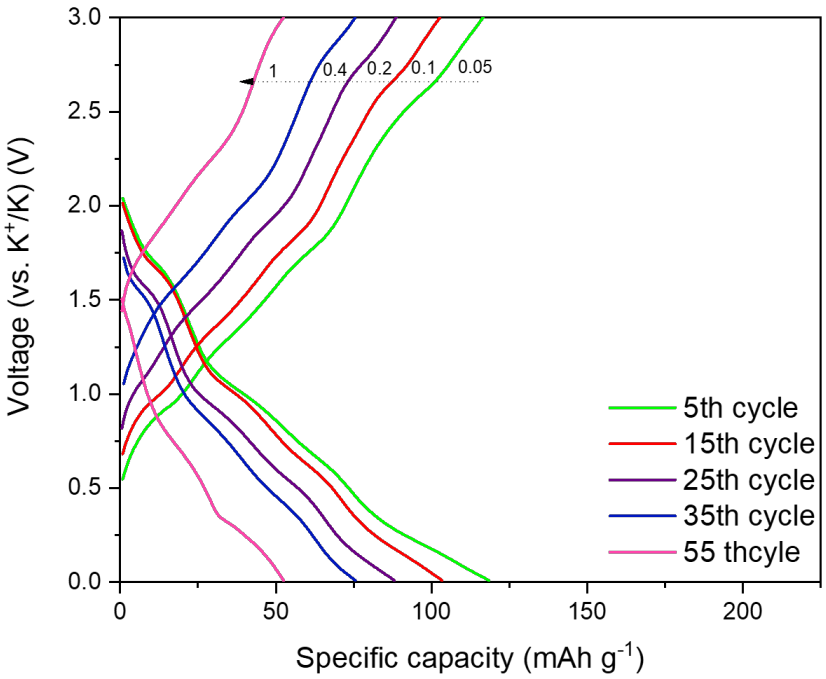

Figure 3: Curve CD a diverse densità di corrente per MoS_2 con KPF_6.

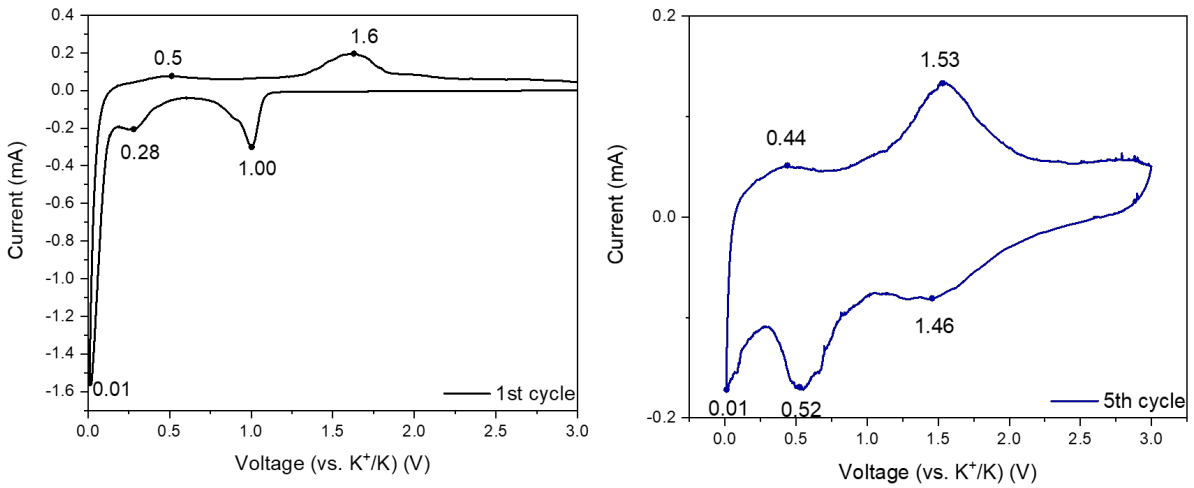

Figure 4: Voltammogramma del ciclo 1 e 5 con relativi picchi indicizzati per il sistema MoS_2 con KPF_6.

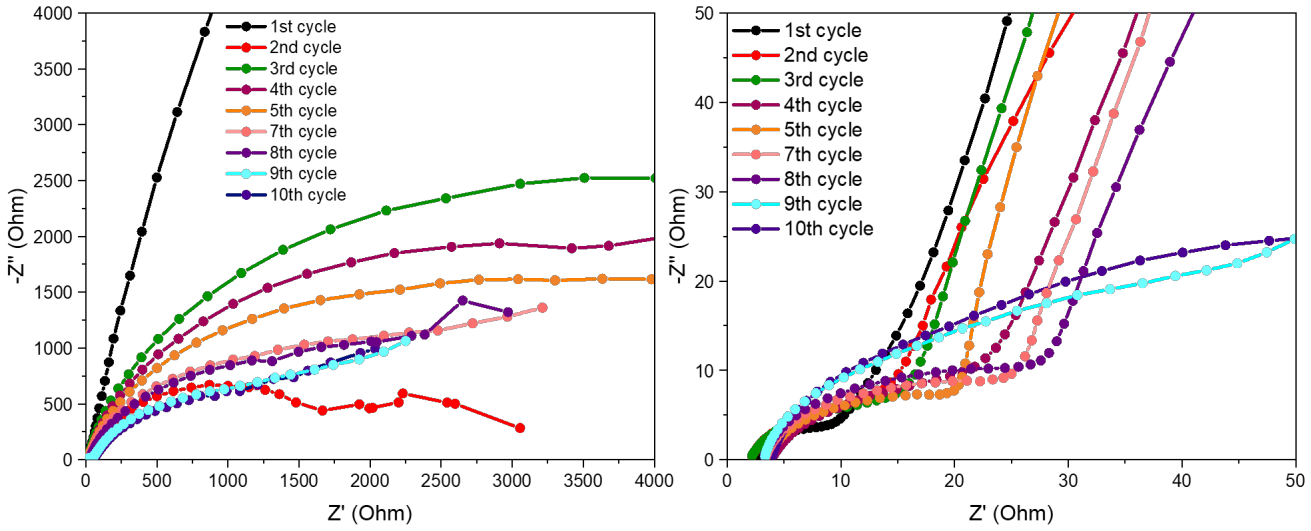

Figure 5: Diagramma di Nyquist per il sistema MoS_2 con KPF_6, a sx si mostra l'andamento in tutto il range di frequenze; a dx andamento ad alte e medie frequenze, analisi del forming.

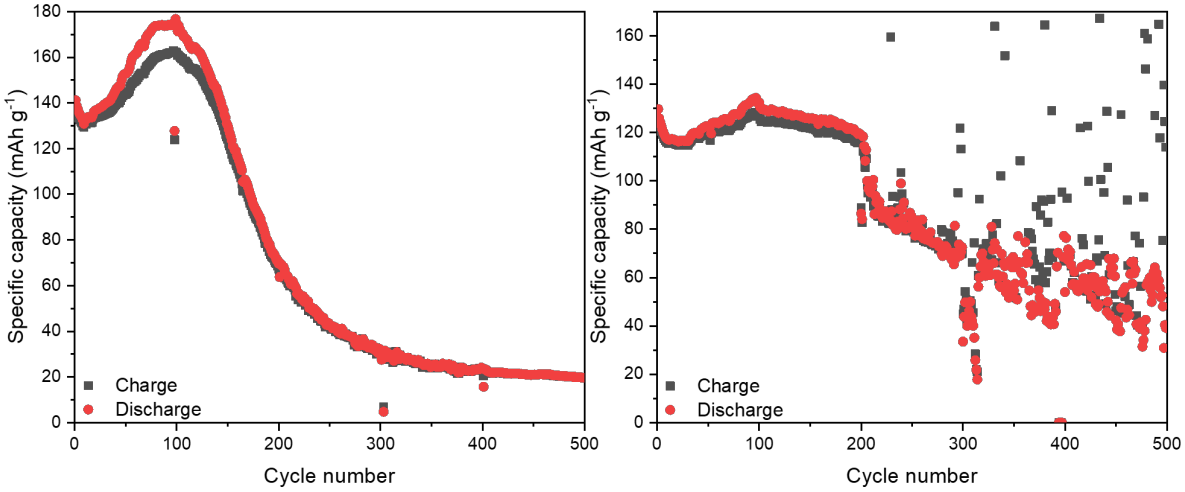

Figure 6: Capacità specifica vs. numero di cicli per il sistema MoS_2 con KPF_6, test di invecchiamento a 0.1 A/g per 500 cicli.

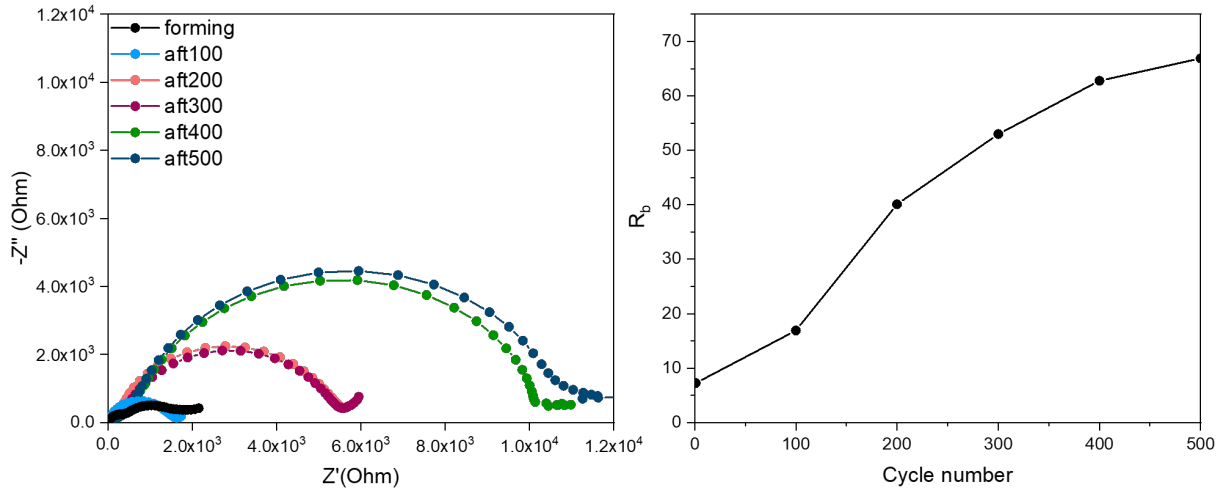

Figure 7: Diagramma di Nyquist per il sistema MoS_2 con KPF_6, a sx si mostra l'andamento in tutto il range di frequenze; a dx andamento della resistanza del sistema vs. nuemero di cicli.

Grafite-KPF_6

La grafite presa in considerazione è una grafite commerciale. Nel sistema con KPF_6 come sale ha come risultati in carica e scarica un decadimento rapido delle performance. Il primo ciclo ha una capacità di 80 mAh/g, mentre poi raggiunge un valore intorno ai 10 mAh/g. Comparando questi risultati con quelli teorici, risultano estremamente più bassi infatti, Il valore teorico si attesa intorno ai 279 mAh/g con il composto KC_8. L'analisi della ciclovoltammetria presenta nel ramo catodico i picchi a 0.1V mentre in quello catodico a 0.5. Questi range di voltaggio sono attestati in letteratura e sono relativi ai processi di intercalazione e de-intercalazione. Il sistema soffre di un notevole fenomeno di polarizzazione (si nota sia dall'allontanamento delle curve di CD che dalla distanza dei picchi in CV).

Grafite-KFSI

Il sistema con il sale KFSI non è in grado di effettuare più cicli di carica-scarica ed anche la ciclovoltammetria dà risultati estremamente rumorosi che non sono stati riportati. L'incompatibilità del sistema materiale attivo-elettrolita è riscontrabile anche nelle micrografie (in Figura 8). Si nota infatti la presenza di una superficie non perfettamente liscia come quella del materiale non ciclato. A confermare ciò anche la micrografia a più alto ingrandimento dove si nota una morfologia tipica delle grafiti espanse, con i piani grafitici separati ed una superficie meno omogenea e più rugosa. Il meccanismo di intercalazione nei sistemi eteri a bassa concentrazione è attraverso la co-intercalazione, per cui l'inserzione avviene con lo ione potassio solvatato quindi con un raggio maggiore. Questo è quello che si pensa possa essere accaduto. Il sistema KFSI in DME è ritenuto migliore ma andrebbe testato a più elevate concentrazioni.

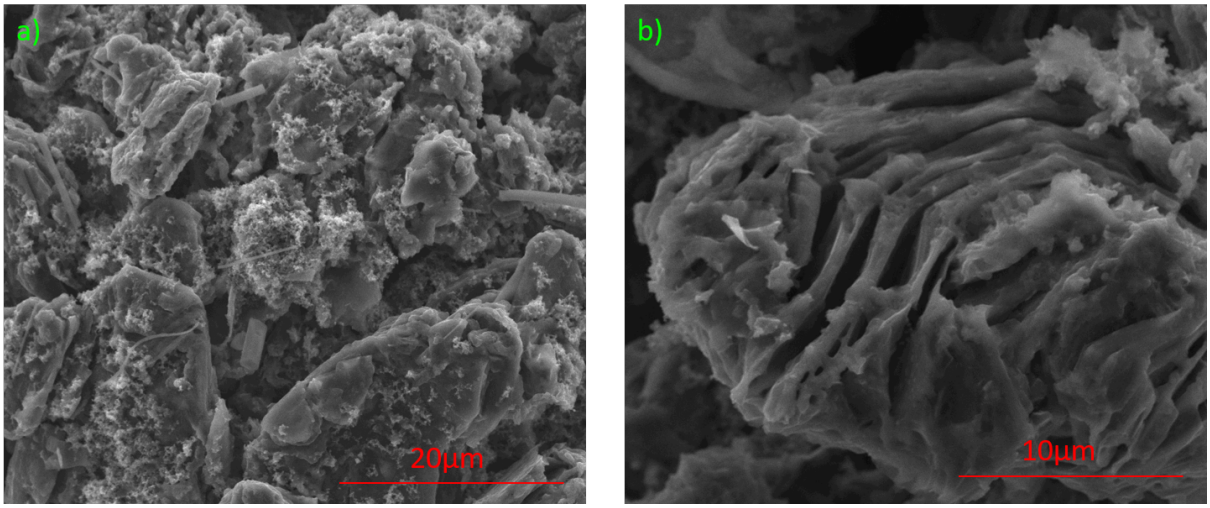

Figure 8: Immagini al FE-SEM a diversi ingrandimenti per il sistema grafite con KFSI.

SuperP

Cell	M_a	D-cap 15	CE(%)	D-cap 100	CE(%)	D-cap 200	CE(%)
1	0.001531g	140.15	91.79	118.41	96.77	107.65	98.91
2	0.001451g	143.23	91.84	118.89	96.73	110.44	98.71

Table 6: Performance di tutte le celle testate nella prova di carica-scarica con relativa CE per SuperP con KPF_6.

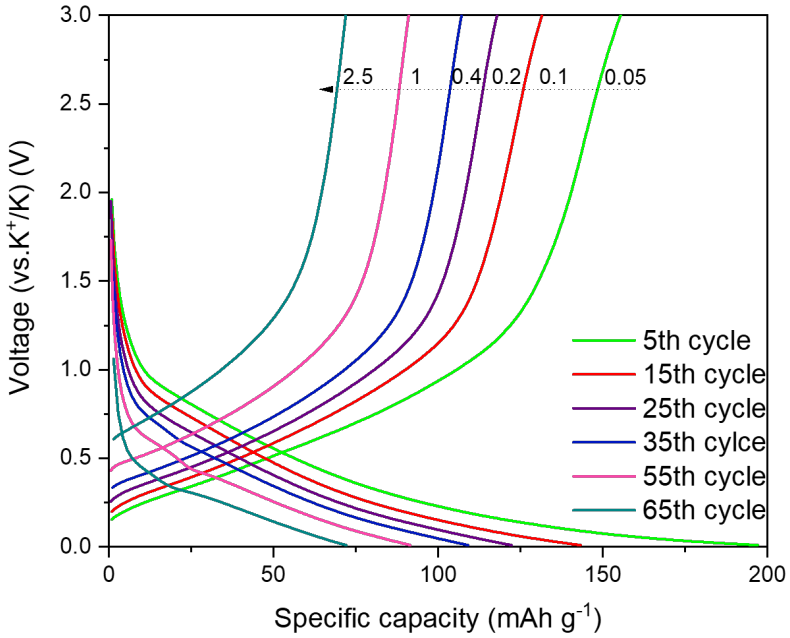

Figure 9: Curve CD a diverse densità di corrente per SuperP con KPF_6.

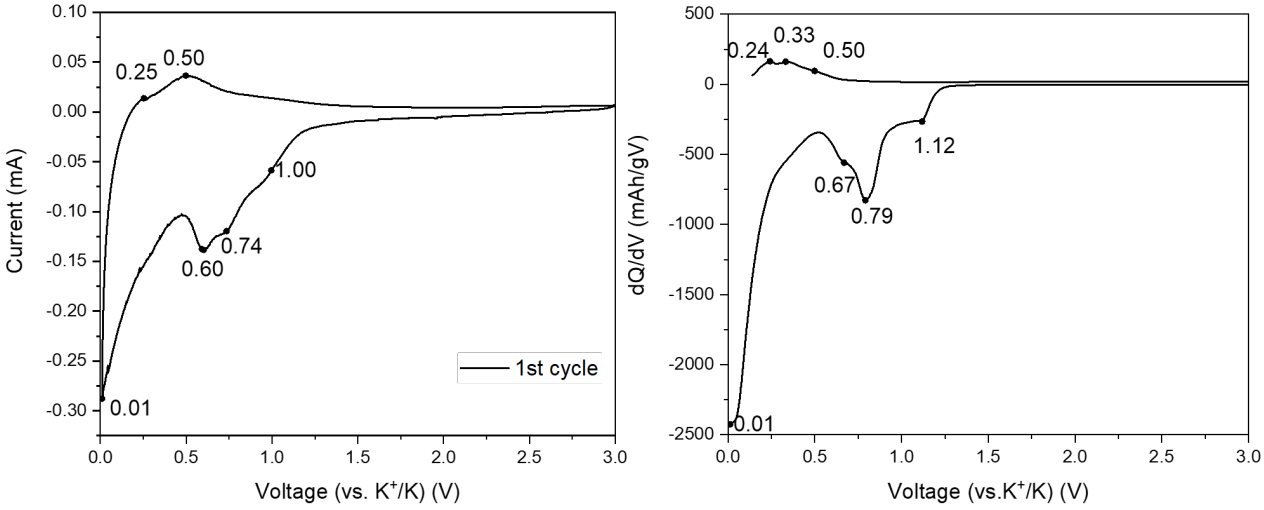

Figure 10: Voltammogramma del ciclo 1 e relativa dQ/dV con relativi picchi indicizzati per il sistema SuperP con KPF_6.

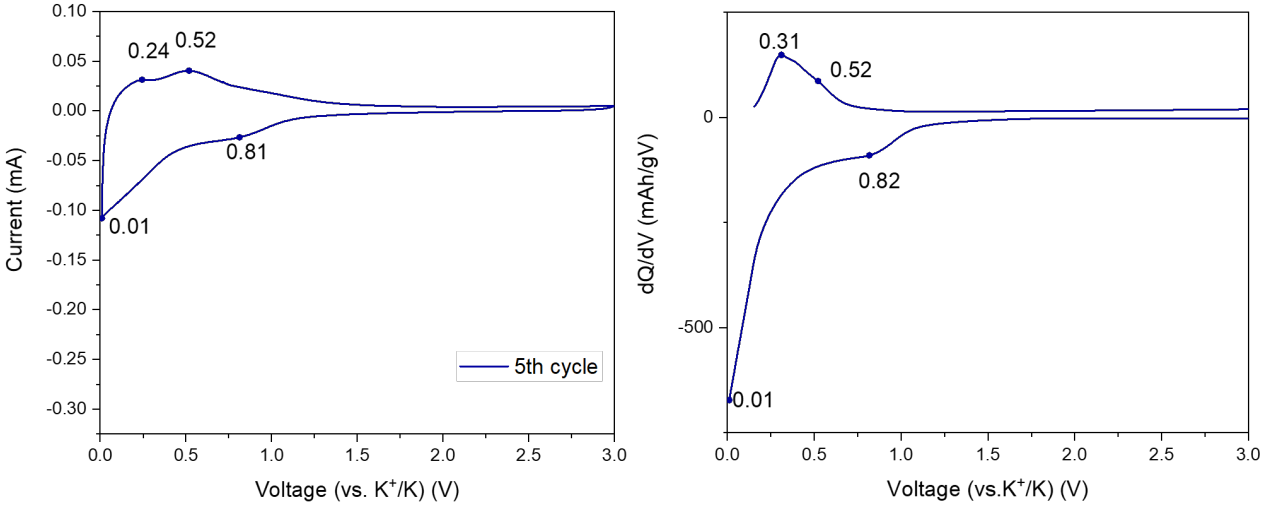

Figure 11: Voltammogramma del ciclo 5 e relativa dQ/dV con relativi picchi indicizzati per il sistema SuperP con KPF_6.

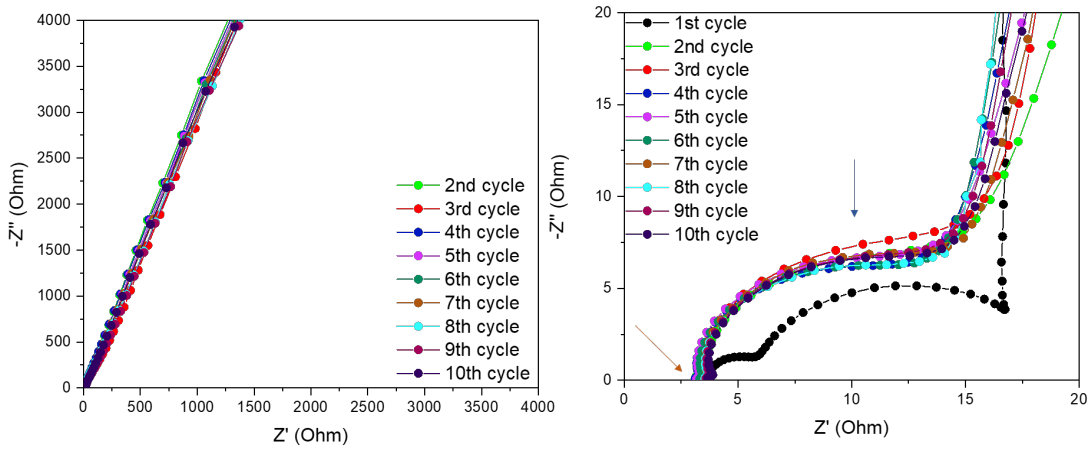

Figure 12: Diagramma di Nyquist per il sistema MoS_2 con KPF_6, a sx si mostra l'andamento in tutto il range di frequenze; a dx andamento ad alte e medie frequenze, analisi del forming.

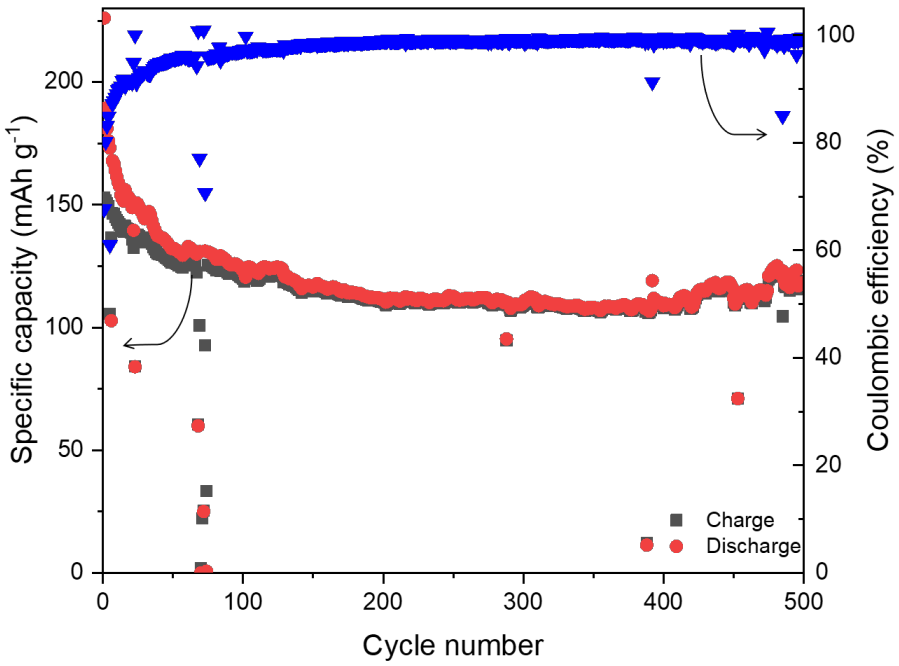

Figure 13: Capacità specifica vs. numero di cicli per il sistema SuperP con KPF_6, test di invecchiamento a 0.1 A/g per 500 cicli.

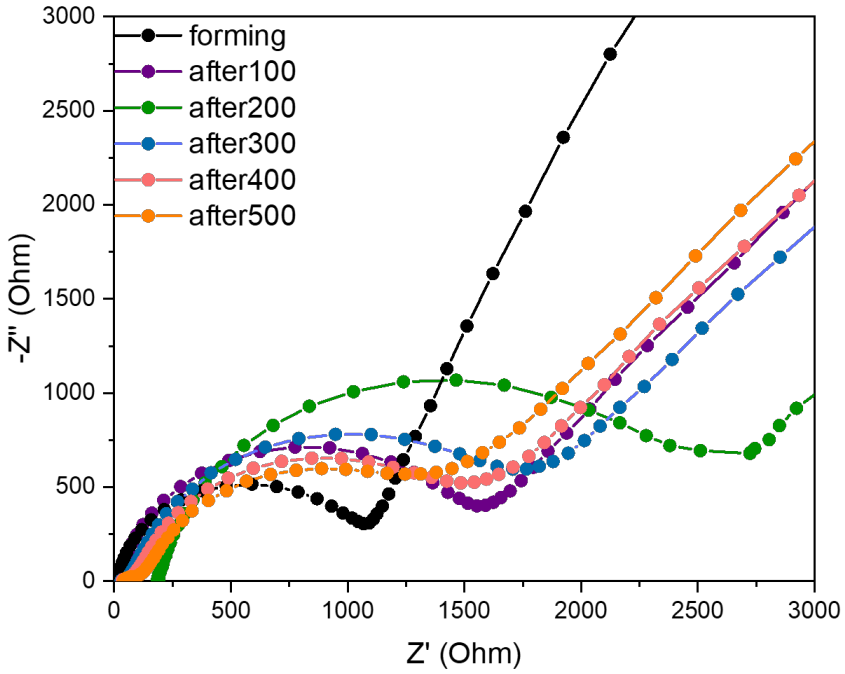

Figure 14: Diagramma di Nyquist registrato ogni 100 cicli durante il test di invecchiamento per SuperP con KPF_6.

C45-KPF_6

Cell	ma	D-cap 15	CE(%)	D-cap 100	CE(%)	D-cap 200	CE(%)
1	0.001633g	169.82	93.44	144.07	97.33	130.86	98.85
2	0.001453g	214.57	94.09	177.18	97.24	141.55	98.91

Table 7: Performance di tutte le celle testate nella prova di carica-scarica con relativa CE per C45 con KPF_6.

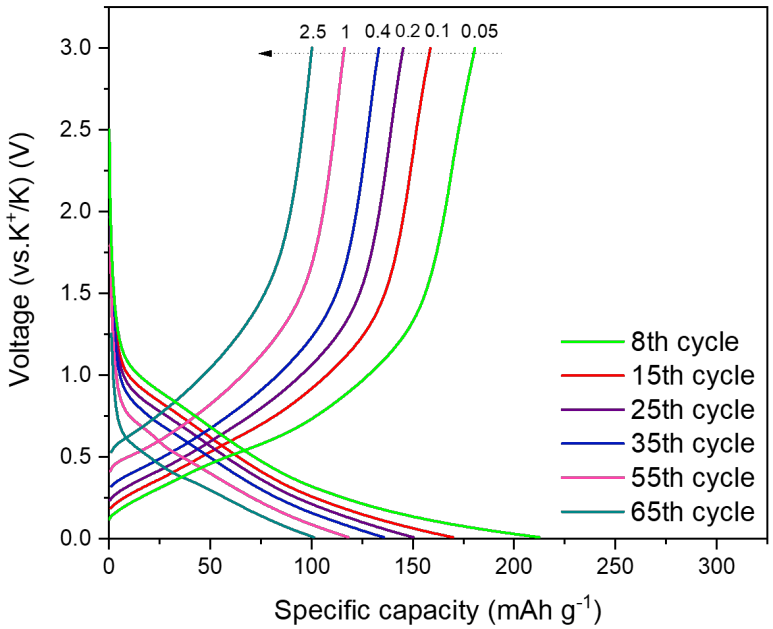

Figure 15: Curve CD a diverse densità di corrente per C45 con KPF_6.

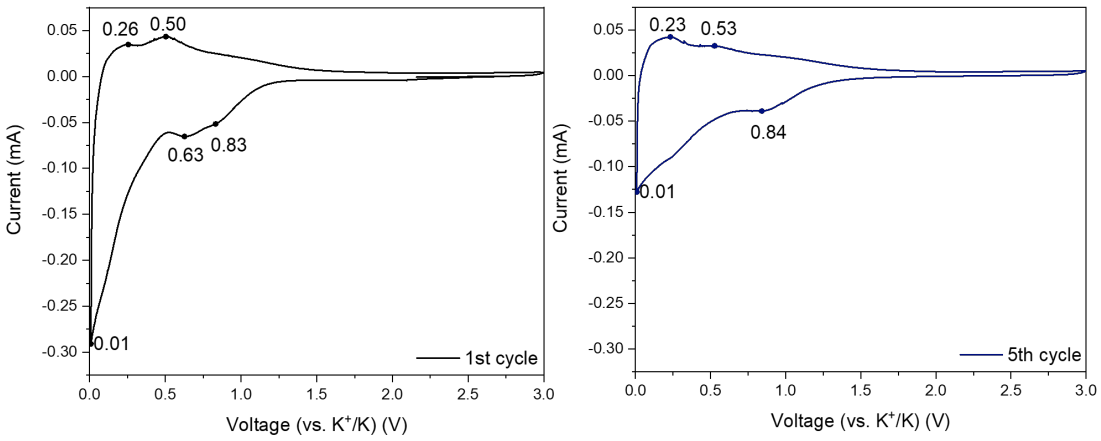

Figure 16: Voltammogramma del ciclo 1 e 5 con relativi picchi indicizzati per il sistema C45 con KPF_6.

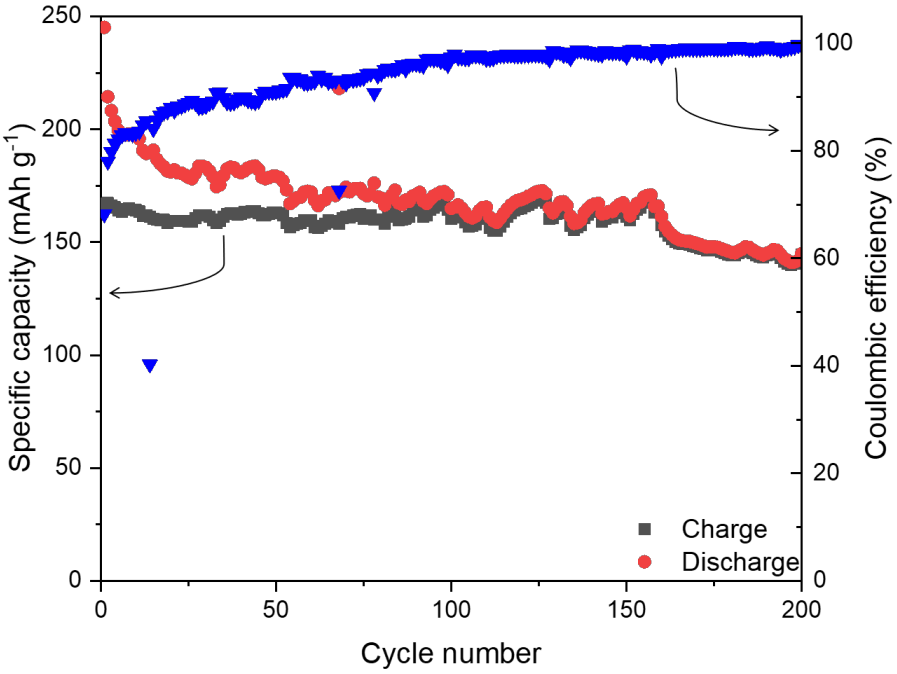

Figure 17: Capacità specifica vs. numero di cicli per il sistema C45 con KPF_6, test di invecchiamento a 0.1 A/g per 200 cicli.

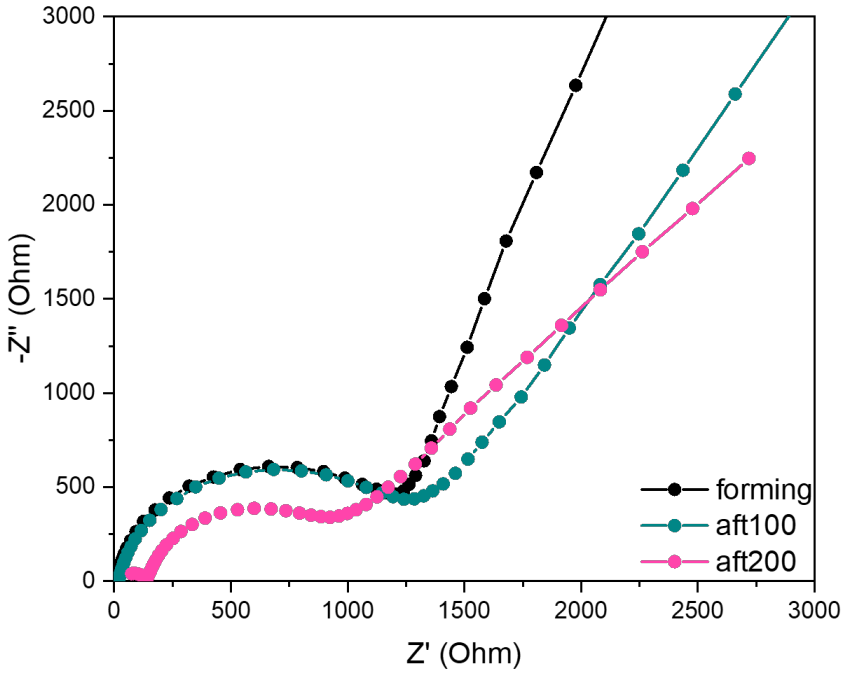

Figure 18: Diagramma di Nyquist registrato ogni 100 cicli durante il test di invecchiamento per C45 con KPF_6.

Discussione e conclusioni

In questa sezione verranno comparati i risultati ottenuti. Nel grafico in Figura 19 viene mostrata la capacità al variare della densità di corrente per i diversi sistemi. Le migliori performances sono del materiale C45, seguito dal SuperP ed infine dal MoS_2. Risulta interessante notare come la CE invece ha un andamento differente. Il superP ed il C45 presentano una CE inferiore a più bassa densità di corrente mentre MoS_2 la mostra più bassa ad alta densità.

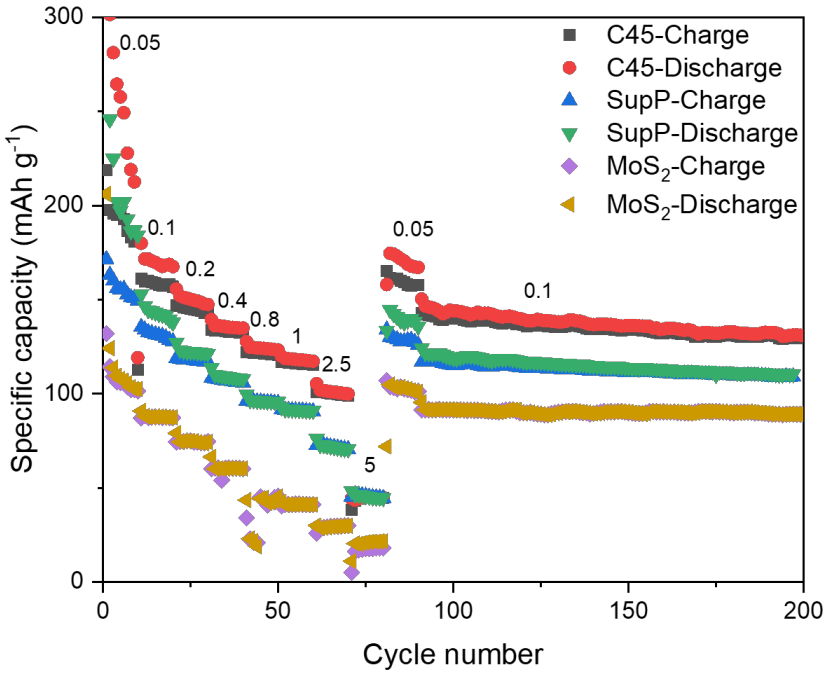

Figure 19: Capacità specifica vs. numero di cicli per i sistemi SuperP, C45 and MOS_2 with KPF_6 in EC:DEC.

La comprensione dei meccanismi di funzionamento rappresenta la sfida più grande in quanto si tratta di materiali non ancora esplorati. Per quanto riguarda il disolfuro di molibdeno la finestra di voltaggio scelta fa sì che sia presente sia un meccanismo di intercalazione che di conversione. Detto ciò i range in cui avvengono e le relative trasformazioni nel dettaglio non sono ancora note, in particolare nella zona relativa alla conversione; poco esplorata in quanto ritenuta causa di una veloce degradazione del materiale. Per quanto riguarda i carboni conduttivi invece risulta controverso stabilire quale delle due zone sia responsabile del meccanismo di intercalazione e quale di quello di adsorbimento superficiale. In letteratura la questione sugli hard carbon, che vengono presi come esempio, è ancora aperta. Sembrerebbe plausibile la teoria adsorbimento-intercalazione, per cui nel range di tensione più alto il potassio adsorbe sulla superficie per poi intercalare. Per quanto riguarda il comportamento all'aging si è visto che il sistema MoS_2 presenta un andamento non regolare con peggioramento delle performances in entrambe le celle testate.

Le motivazioni potrebbero risiedere nella degradazione dell'elettrolita (in figura si vede la presenza di fenomeni ossidativi) e nell'elettrodo in sè che non risulta meccanicamente stabile. Diverso è il caso del sistema SuperP-KPF_6, dove e in termini di performance elettrochimiche e dai diagrammi di Nyquist si nota che il sistema rimane estremamente stabile. Il C45, nel test di aging, mostra un andamento leggermente meno stabile rispetto al SuperP, come si nota anche dai diagrammi di Nyquist.

In linea con quanto trovato in letteratura, questo lavoro dimostra l'importanza dell'elettrolita e nel meccanismo e nelle performance. Risulta inoltre importante il carattere cristallino o disordinato come anche le dimensioni delle particelle infatti pur essendo materiali carboniosi il SuperP ed il C45 presentano performance del tutto diverse dalla grafite.

In futuro, riguardo i materiali testati, dovrebbero essere svolte ulteriori analisi. In particolare, per il disolfuro di molibdeno sarebbe interessante capire il meccanismo di funzionamento separando i vari contributi di intercalazione e conversione attraverso la scelta di cut-off voltage diversi e relative analisi ex-situ XRD. Per quanto riguarda l'ottimizzazione delle performance si potrebbe controllare la struttura (da micro a nano) o la fase infatti la struttura 1T-MoS_2 presenta un carattere metallico che migliorerebbe la conduzione nell'elettrodo. Per quanto riguarda la grafite bisognerebbe provare ad usare un materiale attivo diverso e valutare un elettrolita base etere con concentrazioni maggiori che da letteratura sembra essere più performante. I carboni conduttivi risultano essere, da questa ricerca, i materiali più promettenti. Al contempo non sono stati ancora indagati per il potassio; risulta quindi importante procedere con ulteriori test per comprendere il meccanismo di funzionamento e da qui ottimizzarlo. A tal proposito potrebbe essere utile effettuare delle voltammetrie a diversi scan rate.

In conclusione, in questo lavoro sono stati valutati con successo diversi sistemi i quali giustificano un proseguo nella ricerca al fine di chiarire i meccanismi di funzionamento dai quali partire per ottimizzare le performance.

List of Figures

List of Tables

Contents

List of Abbreviations

BTM	Behind the meter
CD	Charge-discharge
CE	Coulombic efficiency
CMC	Carboxymethylcellulose
DEC	Diethyl carbonate
DME	Dimethyl ether
EC	Ethylene carbonate
ESS	Energy storage systems
GIC	Graphite intercalation compound
HOMO	Highest occupied molecular orbital
KFSI	Potassium bis(fluorosulfonyl)imide
KPF_6	Potassium hexafluorophosphate
LIB	Lithium ion battery
LUMO	Lowest unoccupied molecular orbital
PIB	Potassium ion battery
SEI	Solid electrolyte interphase
SIB	Sodium ion battery

Chapter 1

Energy system and storage

This chapter introduces the energetic scenario and related challenges. A second part will explain different alternatives in energy storage, outlining the role of alkaline-ion batteries. It was deemed exciting and necessary for the inner multidisciplinarity of the topic to focus not only on technical aspects, but also on social impacts these innovations can bring about.

1.1 Energy consumption and climate change: XXI century challenge

Global warming is a severe issue of this 21th-century world, and it is our responsibility to improve the situation. The actual data present an increase of 1.18 ℃ from the previous decades. The temperature rise has been related to the growing presence of some components such as carbon dioxide, fluorides, nitrogen oxide and methane for their heat-trapping role [1].

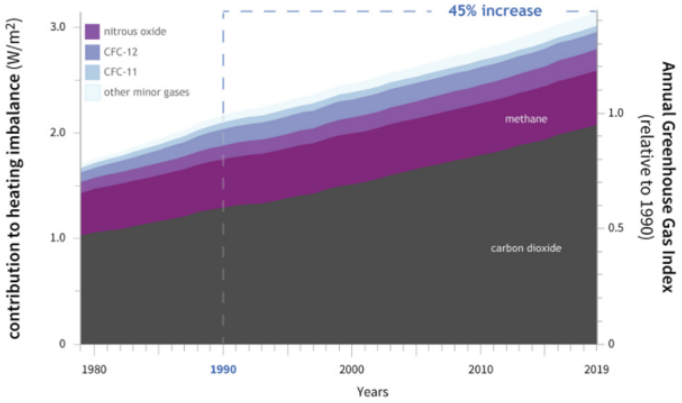

Figure 1.1: CO_2 level measured by ESRL. Adapted and reprinted with permission from [2].

Looking at the graph in Figure.1.1, the CO_2 is quantitatively the highest contributor. Moreover, the global emission levels related to the power sector are 42% [3] of the whole. Hence, it is the first one intended to be limited. A way to accomplish this task is to make

a transition from fossil fuel-based energy to renewable energies. These comprise wind, solar, tidal and hydro energy sources. While representing a solution, their inner character is the intermittency, which does not correspond to the demand. To balance this aspect, storage devices help accumulate energy overproduction and return it when needed. In addition, they can stabilise the grid. In recent years, governments are increasingly aware of the seriousness of the problem: Paris Agreement is part of the willingness of 195 states to cooperate to achieve a maximum temperature increment of 1.5 ℃ by 2050. The topic has reached public opinion too, thanks to movements such as "Friday for future", which has taken root globally with 14M strikes to date [4].

Lowering the emissions collides with the ever increasing demand in energy, which is well represented by Figure 1.2.

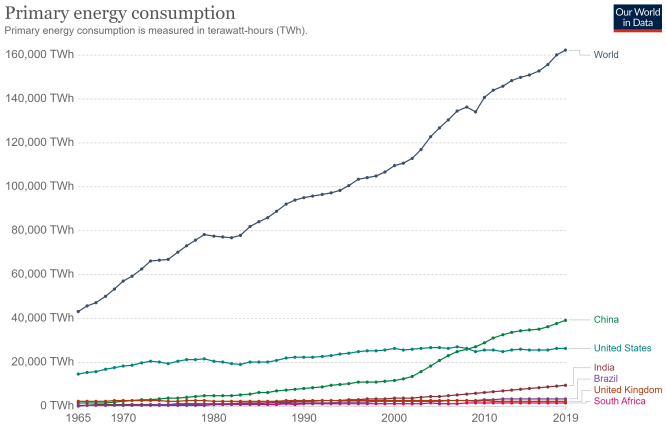

Figure 1.2: Primary energy consumption. Adapted and reprinted with permission from [5].

In this context, it seems more than urgent to find out a technological solution to optimise energy consumption, if not reduce it. The power is highly centralised: the generator produces energy distributed through a transmission and distribution lines (T&D). This system has the drawback that high operation cost has to be spent and with the introduction of renewable sources, the grid is destabilised. Furthermore, it did not solve the problem of providing energy to third world countries where the infrastructure cost is too high. In the next paragraph, a possible solution is presented.

1.1.1 A new energetic paradigm: from consumer to prosumer

To enhance the reliability of an energetic system, demand and supply should be aligned either spatially and temporally. An energy source should be coupled with a storage device that can deliver power when needed. Moreover, to eliminate operation cost for TD and the correlated inefficiency due to transport, a behind the meter system (BTM) can be adopted. The electricity system can be viewed as divided by the meter. This latter is a device that displays the electricity consumption of the place where it is installed. In a traditional system where electricity is provided by external, the meter registers how much energy is provided.
A BTM system is electrically connected to the customer's side, not to the utility. It can

store energy when there is an excess of production from a renewable energy source such as solar or when the price is low. The main examples of BTM are:

- On-site generation (solar panel, wind turbine);
- On-site storage (batteries, usually 3 kW to 5 MW);
- Microgrids.

An example image of a BTM system is pictured in Figure 1.4.

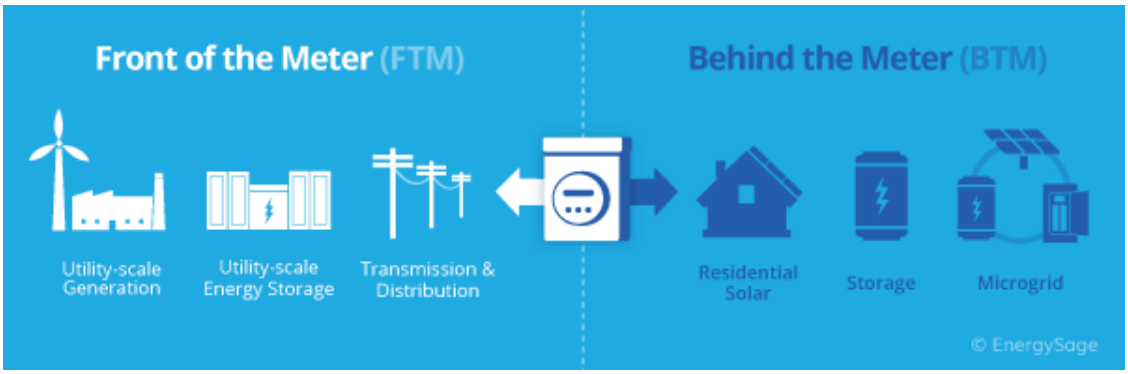

Figure 1.3: Behind-the-meter and front-of-the meter scheme. Adapted and reprinted with permission from [6].

The advantages can be summarised in the following points:

- reduction of operation cost;
- improving the efficiency;
- reducing CO_2 emission;
- balance of demand and supply.

Each of these benefits will be described compared to the current grid.
Nowadays, to provide enough energy at peak hours and make the grid reliable, 15% of the energy surplus is wasted. In the USA, 40% of energy is wasted from residential.
The closeness between users and utility can get better in this aspect. For example, in a BTM system, a user is a consumer and a prosumer. It means that it can store energy from its photovoltaic panels and sell it. Furthermore, a better awareness from the user's side can shift in peak hour demand, enhancing a more responsible behaviour. In this regard, the social side comes into play. It has been highlighted how consumers choices are as important as technical ones.
Each system providing energy has a certain amount of CO_2 emissions. For a typical fossil fuel, it ranges from 888 tonnes per GWh for conventional coal to 499 tonnes per GWh for natural gas, and only 85 tonnes per GWh for solar panels. From a grid perspective, BTM reduces stress and congestion on the line, which helps reduce the use of generators. Moreover, a distributed system and its efficient management minimise the dependency on foreign resources, thus making nations energy independent. Towards this goal, many

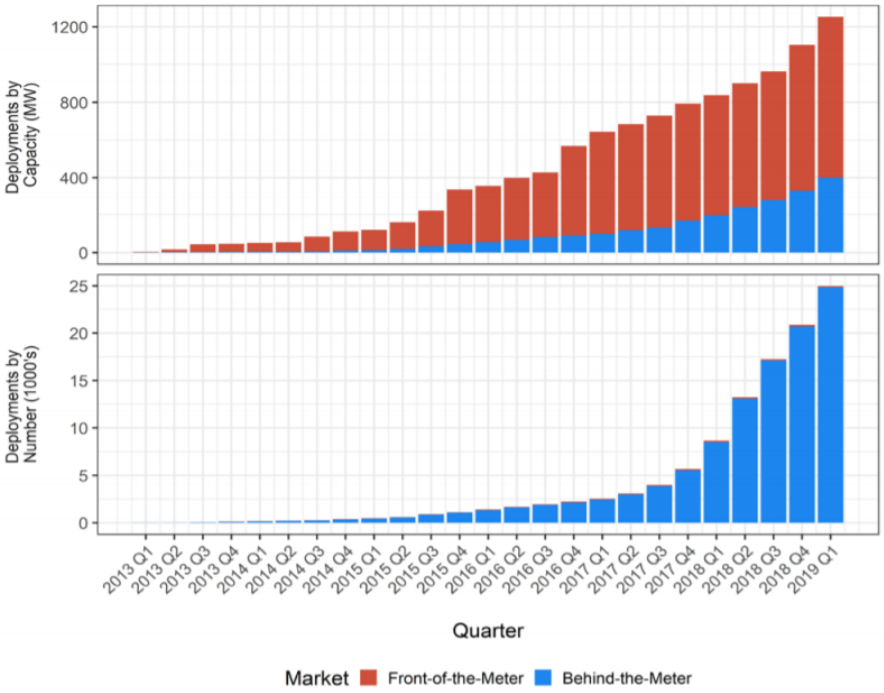

Figure 1.4: Behind the meter in market in deployment by number and by capacity. Adapted and reprinted with permission from (GTM).

countries such as the USA and China have raised energy production through renewables up to 30% [7]. The trend in the market is positive, as shown in Figure 1.4.

To spread this solution, a cost reduction of batteries and ancillary services is needed. To date, the diffusion of BTM is still highly dependent on favourable policy and economic subsidies, some of which will be reported in the following section.

Succesfull applications of BTM technology

Several governments support energy storage systems (ESS) penetration through specific policies program. The strategies adopted are various: subsidies, released loan support funds, incentive in tax credit and electricity tariff systems. Subsidies, in particular, are the most direct way to improve the economic feasibility of ESS.
In Germany, subsidies amount to one-third of the installation costs for ESS with solar panels [8]. In Japan, the government has enhanced subsidy programs to spread broadly household emergency power sources a fortiori for frequent earthquakes. In California, USA, there is a specific program called the Self-Generation Incentive Program (SGIP), which disposes of subsidies for advanced ESS [9].
In Korea, many financial initiatives were promoted for improving the economic effectiveness of behind-the-meter ESS. In particular, the manoeuvre consisted of a 6% investment tax credit to customers who install ESS and through the ESS Electricity Charge Discount Program (ECDP). Thanks to this, last customers could take advantage of load shifting and peak reduction and the program benefits. Coupled with this, technological advancements boost the economic feasibility of ESS applications. As a result of the ECDP, market size grew up from only 27 billion dollars in 2015 to 825 billion dollars in 2018 [10]. It

is compelling because it shows how the cooperation between politics and technological development can benefit society in this sector, where the current costs are still too high to be sustained by private citizens.
Another exciting application regards the use of batteries in the micro-grid systems, which are not connected to the national grid. This is particularly useful in all those situations with no access to the transmission and distribution lines: it is relevant for rural communities and islands. In these cases, the long distances and the low load do not justify the cost of infrastructures. To date, the most positive data were recorded in 2019, with 770 million people without access to electricityof which 75% localised in the Sub-Saharian region. At the same time, rapid progress has been achieved by the formation of an off-grid system [11]. In these cases, renewable energies are more cost-effective than the conventional option. Moreover, the construction of many renewable energy technologies facilitates is modular; hence, their deployment can be relatively small. This can have a double advantage in cost and risk to many developing countries. Electricity is undoubtedly a powerful means to enhance third-world nations, with micro-grids representing a practical solution to realise it. This brief and intentionally non-exhaustive dissertation concludes possible applications of the ESS. In the following sections, the focus will be on more technical subjects.

1.2 Current storage system and electrochemical role

One of the main hindrances in developing a renewable energy-based society is the coupled storage system. There are different storage devices, and all these differ for capacity, power rating, efficiency, discharge time, maturity and cost. Depending on the final application, a parameter will be prevalent over another. There are many different ways: mechanical, chemical, electrochemical, etc. [12].
These technologies prove to be high-performing thanks to their intriguing energy density, safety profile and cost. They offer great adaptability in energy and power capacity (MW and MWh ratings) among the vast majority of application markets. Other reported technologies with less impact are short-duration flywheels for reserve power and supercapacitors for voltage management of local circuits.
The choice is difficult among batteries types (lead acid, lithium ion, flow battery, etc.).
The lead-acid technology has been used in power application as emergency and backup, while they have been completely replaced for residential application by lithium-ion batteries. They have a low energy density, high power density, low cost but poor cycle life. Its reliability makes them essential in a backup application [13].
Notwithstanding nickel-based batteries durability, low energy, power densities, and inconvenient costs are at a disadvantage in the power area. Other inconveniences are the memory effect and poor ecofriendliness [14].
On the other hand, sodium-based batteries have very compelling characteristics: high energy and power densities combined with low cost and low maintenance. Despite these positive aspects, the necessity to work at a very high temperature makes this solution inadequate for BTM application.
Flow batteries are employed at a large scale and applications with a long time-scale, they associate a high safety to low energy and power density [15], parameters that are incompatible with BTM requirements.

At this point, it seems more clear why lithium-ion batteries are gaining the largest share of the market: higher energy and power density (see Figure 1.5) coupled with moderate cycle life and cost make this solution highly appropriate. Furthermore, the efficiency and capacity are not strongly affected by the depth-of-discharge compared to other battery systems, like lead-acid or nickel-based. A drawback regards thermal runaway, which can lead to fire and explosions.

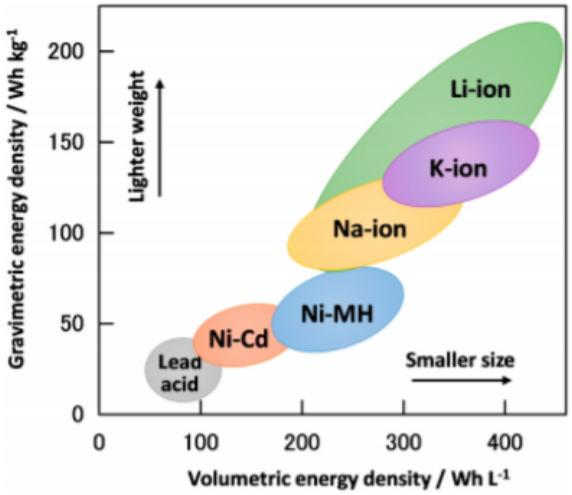

Figure 1.5: Comparative energy system. Adapted and reprinted with permission from [16].

1.3 Alkaline earth challenge

Ascertained that the current solution to store energy from renewables is based on LIB, this paragraph will highlight some chemical-physical properties of this element, compared with other alkalines.
Considering all the applications in which lithium is used, it is clear that in areas where low weight is fundamental (portable electronics, for instance); it is, to date, impossible to substitute it. The horizon of this thesis is stationary storage. Hence, high volumetric energy density is a fundamental factor, more than the gravimetric one.
At the same time, cost, maintenance and safety are also essential in this application sector. Concerning cost parameter, lithium scarcity can increase prices in the following years, so other feasible solutions should be considered. Another problem is the geographical distribution of Lithium, which is uneven and very localized, which can hinder access to resources. Costs of carbonate and salts for potassium are also lower, making it even more appealing.
With respect to energy density, it is connected to the redox potential: a higher potential will correspond to a higher energy density (if all other variables are taken as constant). In this case, K^+/K couple has a redox potential of 2.93 V vs. SHE, which is much closer to lithium than sodium. Potassium-ion batteries have a potentially higher energy density than SIBs.
Moreover, the abundance of potassium will lower the cost of PIBs. In addition, the weaker

Lewis acidity and the corresponding smaller Stokes' radius of K^+ than those of both Li^+ and Na^+ could lead to the highest conductivity and ion mobility of K^+ in the electrolyte. Another advantage of potassium over sodium is that graphite (classic and well-developed anode for LIB) as a negative electrode can be intercalated by potassium ion. At the same time, this is not the case for Sodium, bringing to inadequate capacity. All these aspects are quantitatively summarized in Table 1.1.

Parameter	Li	Na	K
Atomic number	3	11	19
Earth crust abundance	0.0017%	2.3%	1.5%
Density (g/cm^3)	0.535	0.968	0.856
Melting point(℃)	180.5	97.7	63.4
E° vs. SHE(V)	-3.04	-2.71	-2.93
Stoke's radius (nm)	48	41	36
Desolvation energy in EC (kJ/mol)	208.9	152.8	114.6
Theorical capacity (mAh/g)	3827	1165	685
Cost of carbonate ($ per tonn)	6500	200	1000
Cost of metals ($ per tonn)	100.000	3.000	13.000

Table 1.1: Comparison of lithium, sodium and potassium in batteries' related features[17].

1.3.1 Potassium ion batteries: a brief historical perspective

In 1954, graphite intercalation compounds (GICs) were discovered for potassium ion based systems. In the 1980s, intercalation chemistry exploration began with a Prussian blue cathodic electrode. The research brought to the prototype of a potassium ion battery, carried out by Eftekhari in 2004. The configuration used had potassium as an anode and Prussian blue as a cathode. The safety issues related to the highly reactive Potassium and other technologies (see lithium-ion batteries) slowed the investigation. In 2015, Komaba et al. and Ji et al. proved the electrochemical intercalation of K^+ ion in graphite in EC: DEC electrolyte. This finding, coupled with the awareness of lithium scarcity, boost the research on PIB systems (as can be seen in 1.6. After that, the scientific community started looking at other systems such as alloying and conversion anode to improve performance. Moreover, the interaction of electrode and electrolyte was examined. Up to date, various high-capacity carbonaceous anodes were discovered [17]. The state of the art will be explored in more detail in the Second Chapter.

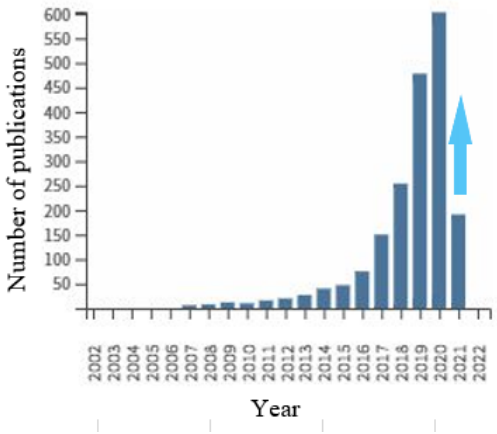

Figure 1.6: Number of publication for potassium ion batteries. Accessed (19-04-2021) in Web of Science.

1.3.2 Challenges

Several critical issues were highlighted during the research on PIBs. The main disadvantage is the large volume of potassium ion. Therefore a priority is to find a way to accommodate the significant expansion that the electrode has to sustain. Considering the same anode material, the volume expansion is 10% at the end of discharge for lithium while 60% for potassium [18]. In addition, the electrode can also degrade through pulverization. The second issue is kinetics. It is clear that the Stoke's radius (see in 1.1)is favourable for the potassium ion, ensuring a fast kinetic in the electrolyte. At the same time, ionic and chemical diffusion in the solid electrolyte interface is slow [19]. Another concern is that it can be an electrolyte reduction and formation of dendrites on metal, due alto to potassium higher reactivity compared to Lithium[20].

1.4 Fundamental steps of this work

The second chapter is the bibliographical analysis of this work, and it is divided into two macro-sections. The first section explains the state of the art of materials and components of a battery. The second section details the electrochemical and morphological characterization techniques used in the following experimental part. The third chapter deals with the experimental work. It is divided into two sections. The first section in the third chapter is a report of instruments and lab facilities, while the second one will describe the procedure followed for electrodes preparation and cells assembly. After that, the performed tests and the set-up will be reported. Lastly, the fourth chapter will display results. The materials examined in this thesis are four: three carbonaceous (graphite, SuperP and C45) and Molybdenum Disulphide, combined with two different electrolytes (KPF_6 in EC:DEC and KFSI in dimethyl ether(DME). The cells were tested in coin cell and T-cell configurations to perform charge-discharge, cyclic voltammetry and EIS test. The results will be then compared with the literature in order to understand the mechanism behind the functioning.

Chapter 2

Materials, test and working principles

2.1 Batteries

A battery is a device which converts the chemical energy contained in its active materials into electric energy via an electrochemical oxidation/reduction reaction.
Battery is a generic term usually referring to the system, the elementar unit is called cell and its components are [21]:

- Anode: component which gives up electron to the external circuit during the discharge process.
- Cathode: component which takes electron from the external circuit and it is reduced.
- Electrolyte: component that uniforms the charge balance allowing the transfer of ions between anode and cathode.

Batteries can be classified as primary or secondary, depending on whether or not they can be recharged. A non rechargeable battery is catalogued as "primary", while a rechargeable one as secondary. The focus of this thesis project is on the rechargeable ones. A rechargeable battery has an external system which can reverse the spontaneous direction of current flow: in this way the cathode will be oxidesed and the anode reduced. The two modes in charge and discharge are shown in Figure 2.1.

The working principle is called "rocking chair" because K^+ ions travel back and forth betwixt anode and cathode. In charging process of a full battery, the electron moves towards the anode via an external circuit, at this point a reduction reaction takes place. The discharging process is similar with the role of anode and cathode reversed.
The choice of materials for each component is fundamental for a correct and optimised system. In the following sections, the state of art of materials will be given.

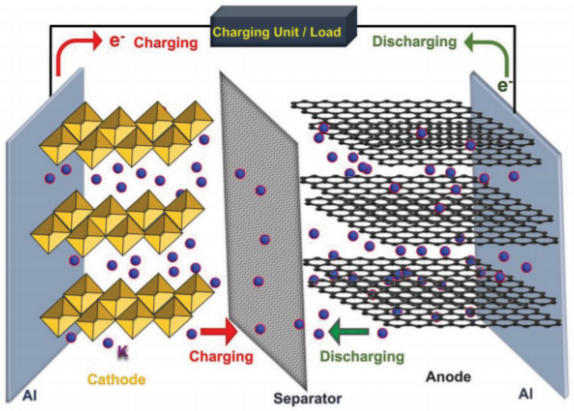

Figure 2.1: Scheme of a potassium battery. Adapted and reprinted with permission from [16].

2.2 Anode material

Anode is the component that maintains the ions in an high energy state and it is important in determining the energy density and long stable cyclability of a PIB [17]. It is responsible of cell voltage too.
Among all materials, the pure metal is the best for anodic electrode for its high energy density and largest amount of metal in the smallest space (highest packing density) [22], with a specific capacity of 685 mAh/g. At the same time, several drawbacks hinder its application: dendrite formation and related safety issues make it difficult to use it even if the lower melting point (63.4 ℃) compared to lithium and sodium could help dendrite issue through a self-healing process [23]. Luckly, it is possible an electrochemical reaction between different materials at low potential, therefore there are other possibilities to host potassium ions.
Based on the mechanism used to store potassium ions, three different classes can be distinguished as anodes:

- intercalation: potassium ions insert in a layered structure forming compounds;
- conversion: the active materials react with potassium and the latter is reduced forming a new compound;
- alloying-type: potassium can alloy with elements of 14 and 15 group;
- organic.

In general, intercalation anodes have more stable performances, while alloy and conversion systems can store more potassium, therefore having an higher capacity. Several factors are responsible for the performances (kinetics, ion diffusion in the electrolyte, ion and electron transfer in the electrode material), which are determined by interlayer distance, pore structure and defects [24]. Moreover, during repeated charge/discharge processes, large volume variation of electrode materials is induced by insertion/extraction of K-ions with large radius. These challenges regard all the abovementioned cathegories. In the following paragraphs, a further description and considerations about how to tackle these issues are given.

2.2.1 Intercalation-Graphitic carbons

In general, an intercalation electrode has a layered structure and the interlayer space is exploited to accomodate potassium ions during charge.
Graphite carbons have excellent performances as anode in the lithium battery field. As is often the case in this field, the development of PIB takes advantage of the discovery from LIB. A similarity is that in both cases the formation of graphite intermediate compounds (GICs) is possible, whereas they have not been found for intercalated sodium. In potassium intercalation, three different GICs have been revealed. Their classification is based on their chemical formula and the stages. The latter are various and they indicate the number of graphene layers that separate two intercalated potassium ions. The GICs formed are KC_{36} stage III, KC_{24} stage II and KC_8 stage I. The stage I GIC, for instance, has a graphene layer for every K-intercalated ion; therefore all graphene layers are intercalated. Figure 2.2 is a graphic description of the just mentioned mechanism.

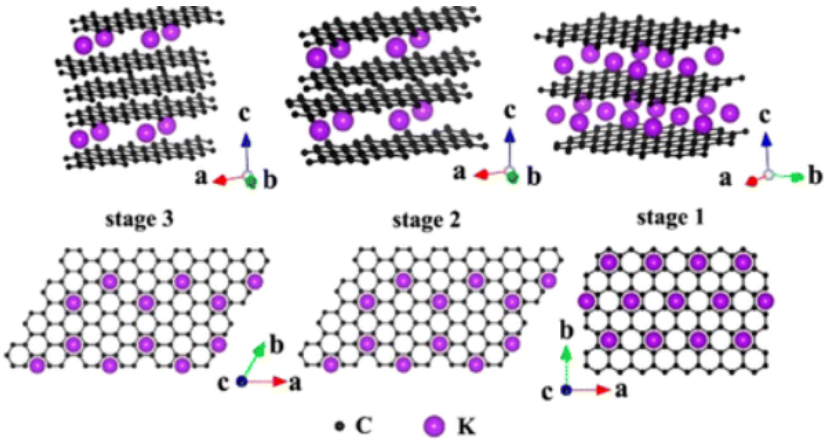

Figure 2.2: Graphical representation of GIC in graphite for PIBs. Adapted and reprinted with permission from [25].

Stages exist at a particular voltage, this information is particularly useful to compare and interpret the results obtained in the fourth chapter. The formation of KC_{36} stage III is attested from 0.3 to 0.2 V, the range for stage II between 0.2 and 0.1 V, and finally the stage III at 0.01 V. During K-extraction, stage III compound is directly converted to the stage III compound at about 0.3 V, and subsequently returns to graphite with low crystallinity when the voltage is above 0.5 V [26].
These findings are supported also by DFT theory, which found out that the formation enthalpy of KC_8 compound is lower than the corresponding stage I (LiC_6) of lithium. From this, it can be inferred that potassium intercalation is even easier [27]. Furthermore the diffusion coefficient of KC_8 is higher enhancing even more the intercalation process [28]. The same DFT theory was used to assess the kinetics and mechanism behind intercalation process, discovering that K^+ ions migrate via the vacancy mechanism rather than the Frenkel one [29]. Inferior cycling and rate capabilities of graphite anode are issues to be tackled. Different strategies are available, one regarding the system and other the electrode itself. As regards the system, binders and electrolytes optimization is an efficient solution. In [30] it is demonstrated the role of different binders on performances as well as the electrolyte. The main binders are: polyvinylydenefluoride (PVDF), sodium

polyacrilate (PANa) and sodium carboxymethylcellurose (CMCNa), they are quite similar in the performances at high number of cycles but dissimilar in the first cycle. This was attributed to the irreversibility of SEI formation, and it is shown how the initial efficiency is improved by PANa and CMCNa on SEI layer compared to PVDF. The other way consists of tailoring the microstructure. In order to improve performances, the graphite was heat treated with potassium hydroxide enlarging the interlayer spacing. The electrochemical performances justify the process: a high reversible capacity of 100 mAh/g after 100 cycles at 0.2 A/g was assessed. It also exhibit increased rate performance and diffusion kinetics of the K-ions during the electrochemical process: an expanded interlayer guarantees a faster potassium ion diffusion [31]. Similarly, in [32] an expanded graphite was sinthetized: the interlayer distance between the carbon layers was incremented (from to 0.387 A)and an increase of surface area (more than three times compared to commercial graphite) resulted in a capacity of 263 mAh/g at the current of 10 mA/g and an high reversible capacity even after 500 cycles at 200 mA/g with a Coulombic efficiency of around 100%. The abovementioned articles demonstrate that a larger interlayer distance enhances the diffusion in solid state and hence the rate performances. Furthermore, the higher specific area allows higher contact between electrode and electrolyte, promoting reaction kinetics.
Others sintethized new materials tailoring the structure at nano-size. In particular, a hierarchical nanostructure was realized with good performances, ie. 232 mAh/g of specific capacity, great rate capability and cycling stability for 500 cycles [33]. Another alternative taken in consideration is doping and co-doping with heteroatoms (for instance sulfur or phosphorus elements). Their large anionic radii and additional potassium active sites expand the interlayer distance and promote K-ion insertion/extraction. Doping with S and/or P also increases the potassium storage per unit, improving the overall specific capacity [34].
Despite these interesting solutions, graphite and its high degree of graphitization hinder the further increment of interlayer distance and specific surface area. Moreover, the structural stability is difficult to be attained during repeated charging and discharging. As a result, others possibilities have been explored.

Intercalation-Amorphous carbon

The amorphous carbons are so called because they do not show a graphitic crystalline structure. The idea behind them is that a non crystalline structure could tolerate in an easier way the potassiation and de-potassiation process. The three main cathegories are: low temperature annealed, hard carbon and soft carbon. These materials have been studied for SIB more than for PIB. Hard carbon are produced by pyrolisis of organic polymer, the structure obtained formed of planar hexagonal network of carbon atoms without order in the c direction. The mechanism through which they store potassium is via “House of card” model, described in [35] and in Figure 2.3.

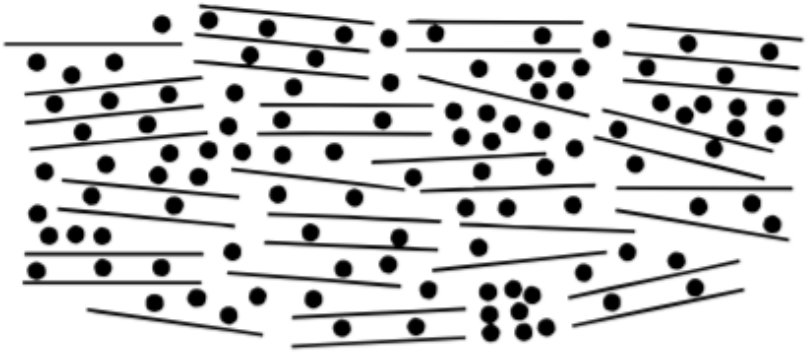

Figure 2.3: House of cards model . Adapted and reprinted with permission from [35].

2.2.2 Intercalation-Non carbonaceous materials

Along with graphitic anode, intercalation is exploited by other materials based on inorganic compounds. The advantage are cost, low toxicity and low potassiation potential. In this regard, titanium anode will be taken into consideration as representative of the cathegory. The safer operating voltage, smaller volume expansion and higher retention rate of high current charge and discharge capacity justify the interest received from the scientific community, although the reduction in reversible capacity. The crystal structure has channels which enhances the K-ion insertion/deinsertion [36]. A titanate with the formula $K_2Ti_6O_{13}$ has been studied in two different morphologies, i.e. a tunnel like and in nanowires. The performance shows that tunnel like has better performances with a capacity of 120 mAh/g at 0.2C [37], thus demonstrating the effect of morphologies in this class of materials too.

2.2.3 Conversion anode

The mechanism through which these materials store potassium is via the conversion reaction in eq. 2.1.

$$MX + nK^+ + ne^- \rightarrow K_nX + M \tag{2.1}$$

in which M is a transition metal element, X is a non metal ion (such as O, S, Cl). The latter also governs the classification of this class, being hence divided in oxide, sulphide, etc. Among these, MoS_2 is the one taken in consideration either for its role in LIB and SIB combined with the interest in the experimental part of this work. The crystal structure has two main configurations: triangular prism structure, named as 1T- MoS_2, and octahedral structure, denoted as 2H-MoS_2. The different structures reflect also physical properties: MoS_2 with 1T-MoS_2 structure (in bulk materials) is semi-conductive, while MoS_2 in 2H-MoS_2 crystal structure has more metallic properties [38]. MoS_2 monolayers are restacked through weak Van der Waals interactions with an interlayer distance of 0.65 nm (Figure 2.4). Every single MoS_2 layer has the S-Mo-S configuration that possesses a layer of Mo atoms sandwiched between two layers of S atoms via strong covalent bonding, as depicted in Figure 2.4.

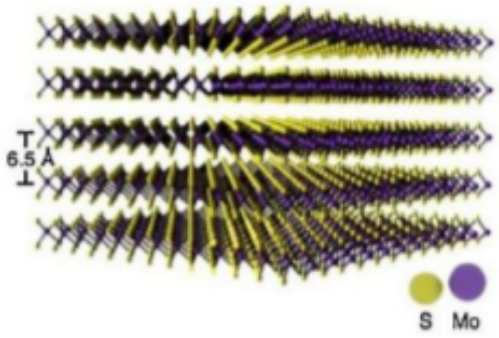

Figure 2.4: Structure of MoS_2. Adapted and reprinted with permission from [39].

The 2D structure provides a large area for storing ions with shortened diffusion pathways. The insertion of ions into the crystal structure of MoS_2 is accompanied by a structural change from 2H semi-conductive state to 1T metallic phase, which occurs in the discharge process of MoS_2. Then, the formed K_xMoS_2 is reduced to MoS_2 and metallic Mo during the charging process. This allows the intercalation process between two planes, process demonstrated by ex-situ XRD test too. In contrast to the mechanism found in graphitic anodes, there is not a staging mechanism, this is also true for LIB and SIB. Coupled with intercalation, a conversion reaction such as this reported in eq. 2.2 allows a further insertion of potassium ions.

$$MoS_2 + 2xK^+ + 2xe^- \rightarrow 2K_xS + Mo \tag{2.2}$$

Moreover, this material is able to maintain a wider interlayer spacing and an open 2D diffusion pathway for K^+ transportation. The two mechanisms are discernible because they operate in two different voltage ranges. It has been discovered that intercalation reaction takes place above 0.54 V vs. K^+/K, and conversion reaction below 0.54 V vs. K^+/K. Upon initial K^+ ion intercalation (>0.8 V), a new phase of $K_{0.4}MoS_2$ appears. $K_{0.4}MoS_2$ maintains the hexagonal structure of MoS_2, whith a d-spacing of 8.28 Å (expansion of 34%) [40]. There were some attempts to enhance performances; a study reports a nano-rose-like MoS_2 in a structure of reduced graphene oxide (MoS_2@rGO). In this case, the hierarchical structure offers better achievements, alleviating the stress and enhancing structure stability [41]. Another compelling behaviour is the one described in [42]: it reported the influence that cristallinity has on the performances and on the mechanism of intercalation and conversion, and it was outlined that lower cristallinity eases diffusion in the intercalation process (which corresponds to a 0.5-3 V potential window), while an higher cristallinity guarantees a more stable structure and boosts surface charge storage at 0.01–0.5 V (conversion region).

Alloying materials

Alkaline elements can alloy with elements of group 14 and 15 (such as Sb, Sn, P, Bi), with a reversible reaction that allows potassium storage, providing an high specific capacity.

The general reaction involved is the following:

$$xA + yM^{+} + ye^{-} \rightarrow A_x M_y \tag{2.3}$$

where A is the alloying element, M is the alkali metal, i.e. potassium in this context; x and y are stoichiometric coefficients. During the charge process, potassium inserts and it alloys with elements forming compounds: this is how K is stored. With this regard the process can have several steps with as many phases and related volume changes (in Sb based anode an expansion of 407% after potassiation was detected [43]), that can lead eventually to the pulverization of the material. This is one of the main problem that needs to be tackled: strategies move towards micro/nano-tailoring of the structure or the deployment of a support such as carbon-based materials which help getting better the conductivity, while maintaining structural integrity. Two examples will be cited, in which the aforementioned strategies brought results. A Sb anode with a nanoporous structure was tested with a capacity of 560 mAh/g at 50 mA/g [44]. A similar strategy was adopted with bismuth where an high specific capacity was not coupled with an high conductivity, so in a 3D structure of Bi, the micron-sized particles reveal a high capacity of approximately 400 mAh/g in DME [45].

Organic compounds

Low cost, abundancy and structural controllability spotlighted organic materials as up-and-coming anode. Unlike inorganic solid mainly bonded via covalent/ionic bonding, these are dominated by Van der Waals interaction, promoting potassium host for larger voids and lower energy barriers [46]. For instance, para aromatic dicarboxyl acid such as dipotassium terephtalate (K_2TP and K_2CP, shown in Figure 2.5) have been investigated. The specific capacity is higher for the K_2CP, corresponding to 181 mAh/g at a current rate of 0.2 for 100 cycles.

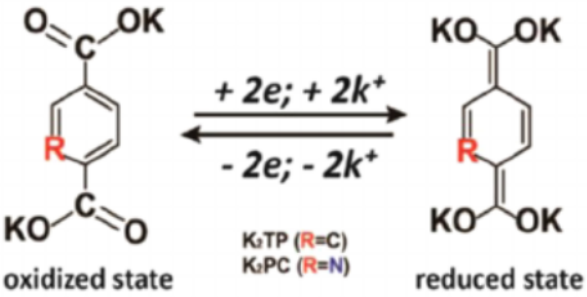

Figure 2.5: Structure of dipotassium terephtalate. Adapted and reprinted with permission from [47]

The low conductivity and solubility in the electrolyte require to be tackled in order to level up this technology.

2.3 Cathode

Cathode is the electrode regulating the energy density of a full cell. In order to guarantee high capacity and cycle stability, an open framework with large channels is ben-

eficial to hold potassium. Despite an,odic electrode where different mechanisms are involved in potassium storage the cathodic materials operate only via an intercalation/deintercalation process. Research on cathode lags behind the anodic electrode.

2.3.1 Prussian blue analogue

Prussian blue analogues belong to the class of metal hexacyanoferrates. The chemical formula is $A_xM[Fe(CN)_6]y{\cdot}zH_2O$, in which A is the alkali metal ion, M is a transition metal and x can have a value between 0 and 2, depending on the chemical valence of the transition metal and of Fe. Their peculiar features are: structural controllability, open framework, stability and low cost.

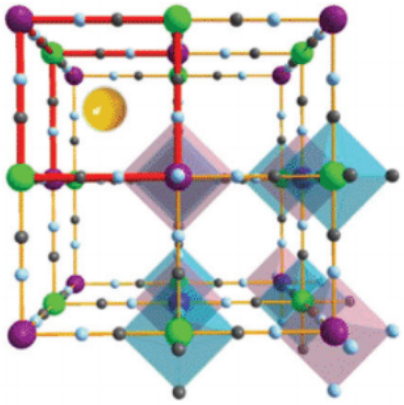

Figure 2.6: Structure of a Prussian blue cathode. Adapted and reprinted with permission from [34].

The mechanism through which they store potassium is shown in Figure 2.6. The FCC structure has a rigid framework and it contains channels and large interstitial sites in which potassium ions can be accumulated. The charge process corresponds to potassium insertion (in discharge, extraction), attainable through a solid state diffusion process, reason why an open frame helps speeding the process, hence the rate performance of the electrode. Strategies towards optimization exploit doping and co-doping. The limiting factor of this type of system regards the specific capacity that does not exceed 100 mAh/g. Another concern is correlated with its synthesis: a low temperature process leads to water which hinders ions diffusion.

2.3.2 Layered transition metal oxide

Sodium and lithium batteries are the leading technology due to modest cost, cycling stability and energy density. The general formula is AMO_2, with A representing the alkaline component and M the metal. However the large size of potassium and phase transitions cause serious damages to the electrode structure, provoking a worsening of capacity over cycles. With this regard, the research moves towards system such as K-birnessite (ecofriendly alkali transition metal oxide materials), in which water augments the interlayer distance improving diffusion kinetics and cyclic stability, leading to performances attaining 134 mAh/g at a current density of 100 mA/g, as well as great rate capability (77

mAh/g at 1000 mA/g) [48]. Another problem is the degradation caused by the electrolyte at high voltage: to circumscribe the phenomenon, a coating (AlF_3) has been designed and it is effectively beneficial for cycle stability. Generally speaking. it is needed to settle for a compromise: high capacity and less structural stability provided by an higher content of crystal water, or vice versa.

2.3.3 Polyanion compounds

The high stable 3D structure with open framework captured the attention as cathodic electrode. The nominal chemical formula is $AM_x[(XO_4)]_y$, with M being iron o vanadium and x phosphorous or sulfur. This class comprises fluorophosphates, phosphates and sulfates. Furthermore, the low energy pathway and the inductive effect of the covalent bond X-O can enlarge the potential window, and hence the energy density. To date, taking advantage of the good performances of $LiFePO_4$, the olivine $KFePO_4$ was studied with the results that larger ions can not be accomodated without damaging the structure and lowering the performances. As with graphite so with this compounds an amorphous $FePO_4$ material delivers a decent discharge capacity of 156 mAh/g at 5 mA/g, with an average voltage of 2.5 V. Meanwhile, almost 70% of its theoretical capacities are retained after 50 cycles. Besides cathode developments, such high voltage requires a stable electrolyte which can stand without decomposing [49].

2.4 Collector

It is the part between the external circuit and the electrode itself. Its role is to let the electrons flow toward the external circuit and it affects capacity, rate capability and long-term stability [50]. Hence, the material has to be electron conductive. The two main considered options are copper and aluminium. The latter is particularly suitable for PIB because it does not alloy with potassium. Furthermore, this could be a great opportunity to further decrease cost and weight of the battery.

2.5 SEI layer

The solid electrolyte interphase (SEI) is a vital element in secondary batteries, reason why it will be dealt within this chapter. It is the most important interface in a battery system and it is the one formed by the reaction between anode and electrolyte.
In the SEI layer, cations (potassium ion in this case) can diffuse keeping the reaction kinetics, while electrons can not, therefore it acts as an electronic insulator between electrode and electrolyte. A representative picture is shown in Figure 2.7.

It affects both electrochemical performances (initial capacity loss, self discharge and cycle life) and safety in LIB technology. The understanding of this phenomenon in PIB is still at the beginning hence a morphological and structural studies are the most examined features, while mechanism, stability and ion transfer are topic still unexplored, hindering the further development of battery itself [51].

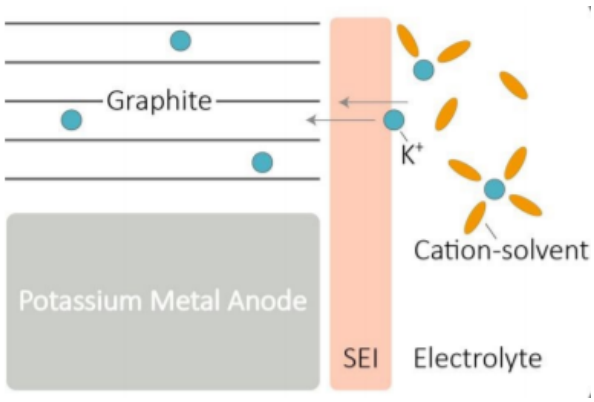

Figure 2.7: SEI layer. Adapted and reprinted with permission from [51].

In order to understand this process, the energetic relation between the Fermi level (indicated as μ_A) of anodic material and the lowest unoccupied orbital (LUMO) of the electrolyte should be considered for the stability of the system. Considering the case in which

$$\mu_A > E_{LUMO} \tag{2.4}$$

an electron transfer from anode to electrolyte will be favorable, provoking the reduction of the electrolyte as shown in Figure 2.8. In a system where anode stores potassium ion in the range of 0-1 V vs K, the formation is thermodinamically driven. This is the case for graphite and alloy-type with a Fermi level higher than LUMO in non aqueous electrolyte. Moreover, the influence of the electrolyte is also very important: there are differences between ester and ether electrolyte, but their correlation with SEI should be further explored. The energetic levels depend on the electrolyte (solvent+salt): every solvents has its window stability, which is affected by the solvent-cation and anion-cation interaction.

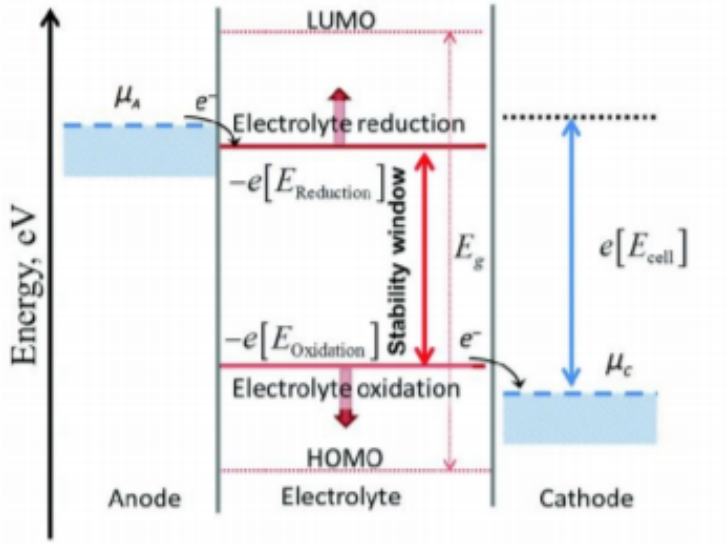

Figure 2.8: Fermi energy for anode and cathode related to HOMO-LUMO of the electrolyte. Adapted and reprinted with permission from [51].

There have been lot of efforts to understand the parameters affecting SEI formation. It was highlighted how the solubility of the compounds formed influences the performances of the electrode: in fact, if the layer is less soluble (maybe due to a weaker Lewis acidity), it is more stable. In literature, it was studied for hard carbon in Li, Na and K batteries, they found out that lithium and potassium have higher Coulombic efficiencies and that their spectra were more similar than the one for sodium with organic component. Furthermore, the presence of peaks suggests a more relevant degradation process in potassium.
There are three possibilities for potassium-graphite interaction. In the first scenario, solvent molecules are not stable towards the anode, this provokes the reduction of the solvent and exfoliation of graphite. The second scenario describes a stable anode-solvent interface, meaning that solvent does not reduce and co-intercalation (potassium with solvent sheath) is possible. The third scenario takes into account a solvent-anode couple which is stable against reduction, but the electrolyte decomposes and it forms a layer on the top of graphite. In this case, the intercalation is carried out by potassium ion, without the solvation sheath [52]. The behaviour is indeed influenced by the electrolyte, so the choice of the latter is fundamental for both potassium kinetics in SEI layer and hence the K-ion intercalation chemistries.
In conclusion, it is indeed true that a battery performance can be tuned through controlling the SEI layer.

2.6 Electrolyte

The electrolyte is composed by the solvent and the salts. It is a fundamental component for the correct functioning of a battery system and it is a crucial parameter to consider in order to improve the performances (such as lifetime, rate capability and safety). An unsuitable electrolyte can be responsible of severe secondary reactions, formation of uneven SEI layers and dendrite growths [17]. Moreover, larger size and lower Lewis acidity of potassium ions bring to consistent differences in solubility, ionic conductivity and solvation/desolvation behaviour.
The different electrolytes can be divided into various categories. A brief overview of the different classes will be given in the following sections, focusing the attention on organic electrolytes, which have been used in the experimental part of this thesis.

2.6.1 Aqueous electrolytes

This class has the peculiarity of non flammability, for this they have been considered for grid applications. Moreover, low cost and sustainability, high conductivity make them an appealing solution. At the same time, a big limit is determined by the potential: 1.23 V causes indeed evolution of H_2 and O_2, limiting the application to materials able to work in this potential window. The other preeminent hindrances are the limited energy density and limited cycle life, the latter due to the degradation of the electrodes. Despite some good achievements, current knowledge does not allow a commercial application of these systems.

2.6.2 Solid state electrolytes

They are divided in inorganic and gel polymer electrolytes. They are regarded with interest for the possibility to sustain high voltage in a safe way. The inorganic electrolytes are based on β-Alumina (BASE) and the general issue is to couple high ionic transport in solid state and related structure. Among alkalines K^+ has the best conductivity, making conceivable a full solid-state battery. The inner brittlness can enhance interfacial reactions, for this a gel polymer with enough flexibility can avoid this drawback.

2.6.3 Ionic electrolytes

In view of high voltage cathodes, there is the need of electrolytes which withstand high voltage too: in this framework, ionic liquids (IL) are considered suitable because of their stability at high voltage. In addition, features like nonvolatility and incombustibility are higly desiderable in an electrolyte system, and ILs are superior if compared to conventional organic and aqueous electrolytes. Furthermore, the solvation influence of cations and anions can be avoided by using neat ILs. An example from the literature is KFSAPyr$_{13}$FSA (FSA = bis(fluorosulfonyl)amide; C3C1pyrr = N-methyl-N-propylpyrrolidinium), which shows low viscosity, strong ionic conductivity, great electrochemical robustness and an electrochemical window of 5.72 V for potassium ion storage [53].

2.6.4 Organic electrolytes

With this term it is meant an electrolyte with a potassium salt and a carbonate or ether-based solvent. Among the various categories, they are broadly studied and offer indeed many advantages: wide voltage windows, superior ionic conductivity and promising temperature performance, to mention a few. The characteristics sought in an electrolyte are [54]:

- High ionic conductivity;
- High thermal stability;
- Wide electrochemical window;
- Inert to other battery components;
- Low cost and environmental friendliness.

The current knowledge on salts and solvents and their possible combination will be dealt in next paragraphs.

Role of potassium salts

Potassium salts are a key component of the electrolyte, which should have features like [54]:

- low dissociation energy and high solubility
- high thermal and chemical stability

- inertness towards other components of a battery
- helps forming an uniform and stable SEI layer
- low cost and environmental friendliness

The most common salts for PIB are listed in table 2.9, each with the related properties. The main common salts are also given. The most widely used salts are KPF_6 and KFSI.

Salt	Structure	M. wt	T_m/°C	Al-corrosion
KPF_6	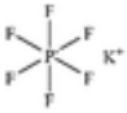	184.1	575	No
KFSI		219.2	102	Yes
KTFSI		319.2	~200	Yes
$KClO_4$	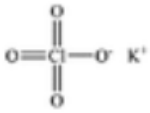	138.5	610	No
KCF_3SO_3		188.2	238.5	Yes

Figure 2.9: Most common Potassium salts. Adapted and reprinted with permission from [54].

The latter is used in particular in high concentration systems (HCE) because of the higher solubility in both ether and ester solvents [55]. Furthermore, it has been evaluated the formation of an uniform and stable SEI layer has been observed. KPF_6 has as drawback, i.e. the hydrolisis of P-F bond and the formation of HF species, which are extremely corrosive [56]. The dissociation of KFSI, on the other hand, forms FSI^- species which corrodes aluminium collector, thereby narrowing the choice of collector to copper.

Solvents

The solvent is a main factor to be considered in the electrolyte. The features required are: high dielectric constant, low viscosity and volatility, good stability, low melting point and high boiling point, low cost and environmental friendliness. Ester solvents, already

selected for LIB, have a preminent role in PIB too. There are two main solvent categories: cyclic carbonates (EC and PC) and linear carbonate (DEC, EMC DMC). The former have an high dielectric constant, as shown in Figure 2.11, hence they can be applied in high voltage systems. EC and DME will be described in detail for their role in experimental part.

Solvent	Structure	ε/(25 °C)	η/(cP, 25 °C)	T_m/°C	T_b/°C	d/(g cm^{-3}, 25 °C)
EC	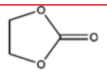	89.78	1.9, 40 °C	36.4	248	1.321
PC	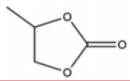	64.92	2.53	−48.8	242	1.200
DEC	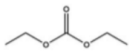	2.805	0.75	−74.3	126	0.969
EMC	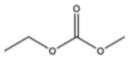	2.958	0.65	−53	110	1.006
DMC	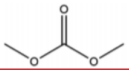	3.107	0.59, 20 °C	4.6	91	1.063
DME	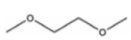	7.2	0.46	−58	84	0.86
DEGDME		7.3	0.99	−68	162	0.944
TEGDME		7.9	4.05	−30	275	1.009

Figure 2.10: Table with solvent properties. Adapted and reprinted with permission from [54].

With regards to EC, it was calculated in that the solvation energy for potassium is the smallest among others alkaline ions (lithium and sodium), which guarantees a fast ion transport and better rate performance [57]. At the same time, it follows that it is not straightforward to obtain concentrated electrolyte. Furthermore, a low solvation energy could accelerate the side reactions. In order to reach right properties, linear carbonates are added as cosolvent. The system EC/DEC, for instance, is one of the most studied solvents and it shows a relatively wide stability window.
Ether solvents were explored lately and are promising for their good stability. Despite EC, ether-based electrolytes are attainable and this ensures a tight bond of ether molecules to the salt ions, increasing the stability of the system. Among them, the most common are DME and DEGDME with low viscosity, while TEGDME shows the positive feature of low volatility, even if it has an higher viscosity compared with the two aforementioned. Focusing on DME, it was found out that the interface polarization resistance depends inversely on the concentration of KFSI. In addition, HCE KFSI–DME electrolyte had an excellent oxidation durability compared with diluted KFSI–DME electrolyte. In accordance with theoretical calculations, DME tends to close binding with potassium ions in such a way the highest occupied molecular orbital (HOMO) lowers and slow down the oxidative decomposition of electrolyte. Talking of SEI layer LUMO energy level of KFSI is lower than that of DME, hence the reduction energy of KFSI is lower than DME. It follows from this that the reduction product is FSI which could form a dense inorganic SEI layer.
In contrast, the lower LUMO energy level of EC/DEC leads to the severe decomposition

and side reactions, resulting in a thicker organic–inorganic SEI layer. Additionally, it found that the kinetics of ester and ether electrolytes also showed an obvious distinction.

Ester has a good oxidation resistance and they can be matched with high-voltage cathodes while ethers show lower oxidation voltage and they tend to form a thinner SEI layer enhancing kinetics of the system.

The influence of different solvents on electrochemical performances has been evaluated in [18] where graphite anodes were tested in different electrolyte solvents (in particular EC:PC, EC:DEC and EC:DMC) with KPF_6 salt. Results show that the graphite anode in KPF_6–EC:PC electrolyte has superior cycling stability and high coulombic efficiency. They proposed that the inferior electrochemical performance of KPF_6–EC:DEC and KPF_6–EC:DMC electrolyte comes from the formation of a more stable SEI layer in EC:PC.
These results are illustrative for the role of electrolyte solvent in SEI layer, and thus the electrochemical performance of electrode materials.
Additives such as fluoroethylene carbonate (FEC) are usually good to stabilize the system in lithium ion batteries, while in potassium ion it is not that positive: In it was studied the effect in half-cell and they noted that solvation energy with FEC was higher than without it hence this could inhibit the ions desolvation. Other studies confirm the negative trend. Besides the peculiar features of the components is the combination of the two that determine the properties.

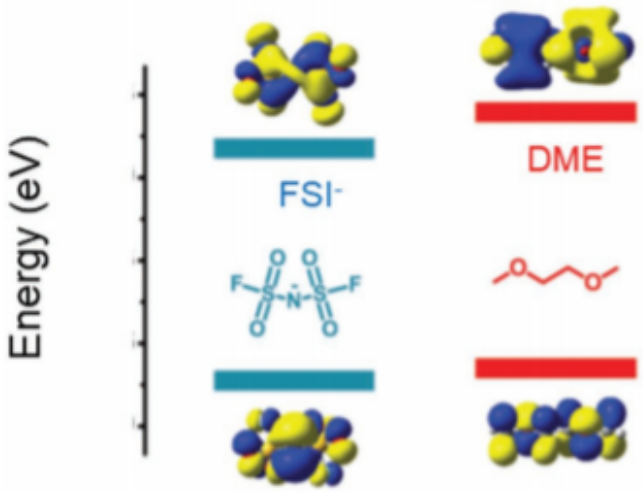

Figure 2.11: HOMO et LUMO levels for DME solvent and FSI^-. Adapted and reprinted with permission from [58].

2.7 Characterization

Several tests are carried out in order to evaluate electrical performances and to elucidate the correlation with physico-chemical processes undergoing in the battery. With regard to electric features of a system, potentiostatic and galvanostatic tests are used (name depends on whether the potential or the current rate is kept constant). To evaluate the phenomena involved during the functioning (i.e., SEI layer formation, degradation of electrolytes, etc.), electrochemical impedance spectrosopy (EIS) and morphologycal characterization (such as ex-situ FE-SEM) are performed.

2.7.1 Cyclic voltammetry

Cyclic voltammetry (CV) belongs to the potentiostatic tests, and the scan rate is kept constant during the test. This analytical technique gives information about:

- Reversibility of a chemical reaction;
- Potential at which an oxidation or reduction reaction takes place;
- Understanding the influence of parameters (temperature, scan rate and concentration of reactant) on a reaction.

Generally speaking, a system tends to its more favorable energetic state: so, if the potential energy of the electrons in the electrode is higher than the potential energy of the empty molecular orbital on the analyte, an electron will be transfered from the electrode to the analyte, vice versa the analyte will undergo oxidation if its highest energy electron in the molecule is at a higher potential energy than the electrons in the electrode. The role of a potentiostat is to change the electrode potential and see if a current is detected [59]. Furthermore, at the surface of the electrode, the scanning potential has to follow the Nernst's equation described in eq. 2.4:

$$E = E^0 - \frac{RT}{nF} ln \frac{Red}{Ox} \tag{2.5}$$

Once the equilibrium potential and the applied potential are known, the ratio can be calculated for each value. The working principles is similar to the linear sweep voltammetry with the difference that, once completed the voltage range, it is then reversed (as clarified in Figure 2.14), hence the term "cyclic". The resulting graph current-voltage is called voltammogram in Figure 2.14 (b). Repeating the test for a certain number of cycles, further information on voltage, reversibility and cyclability can be collected. Moreover, by changing the scan rate, which is the main parameter in this test, it is possible to take into consideration the kinetics of a reaction.
Hence, the main features to be considered are: particle size, scan rate, temperature, electrolyte concentration and electrode thickness [60]. The cell for the test has a working electrode (WE), a reference electrode (RE) and a counter electrode (CE). At the working electrode position is positioned the material to be tested. The potential is controlled through a potentiostat and it is measured between the WE and RE. The voltage of the latter should be stable and constant. The CE helps in closing the circuit.

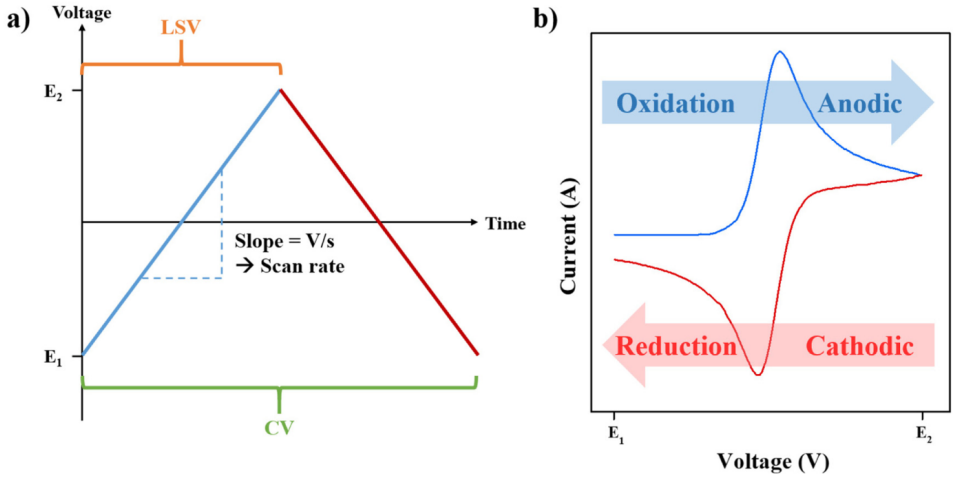

Figure 2.12: a) Cyclic voltammetry input, b) cyclic voltammogram. Adapted and reprinted with permission from [60]

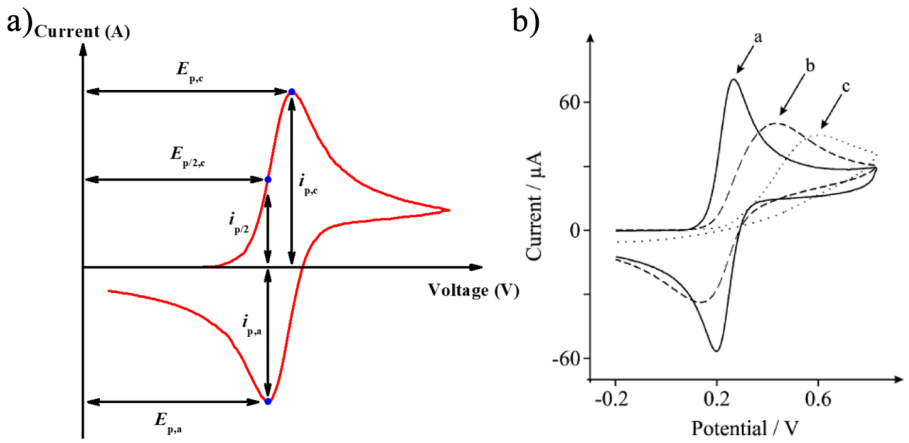

Figure 2.13: a) Cyclic voltammogram, b) Reversible (a), quasi-reversible (b) and irreversible reactions (c). Adapted and reprinted with permission from [61].

2.7.2 Charge-discharge test

Charge-discharge cycles belongs to galvanostatic tests. Usually, batteries are tested at different current rates for a certain number of cycles in a specific voltage range. The output is the capacity of the device, usually plotted as specific capacity vs. cycle number. Furthermore, charge-discharge curves (plotted as potential vs. specific capacity, or vice versa) can be gathered with slope or plateau traits highlighting the different electrochemical reaction involved in charge/discharge. A further information can be attained making a differential capacity analysis: exploiting the linear trend of the curve, data can be interpolated and differentiated. This gives a plot dQ/dV over voltage that, coupled with the related voltammogram, gives a deep insight on reduction and oxidation voltages. In particular, plateau in the voltage vs. specific capacity curve turns up as peaks in the dQ/dV plot, with as narrower the dQ/dV peak as flatter the plateau. Each peak feature represents a different chemical reaction or intercalation environment and the area under the peak is the capacity of that particular process. The cyclic voltammogram (CV) yields

the same information, but under different circumstances. The main difference is that in dQ/dV analysis data are gathered at constant current and there is more time to complete the reaction, while in CV the voltage is forced and a part of capacity could be undetected. Another parameter is that the drop of voltage due to resistance is constant in the capacity-voltage test because current is, while this is not the case for CV (i.e. bringing consistent changes in plot shape [62]). In general, the shape of voltage-specific capacity curve is indicative of mechanisms behind cell operation. In particular,a flat plateau in the potential curve describes a two phase reaction (with a constant chemical potential), whereas a sloped "plateau" (i.e., changing chemical potential) denotes a change in solution concentration. A steep decline (or rise) in the potential signifies the kinetic limit at which a reaction is no longer capable of absorbing the constant current being forced out of (or into) the electrode.

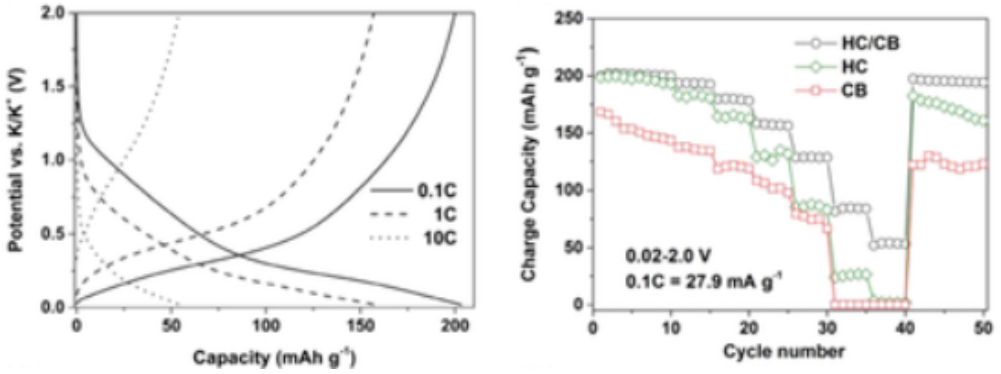

Figure 2.14: Sx CDC, dx specific capacity at different current densities. Adapted and reprinted with permission from [63].

It is a matter of fact that performances lower upon cycling. One way to clear up the reason behind it is with post-mortem, ex-situ analyses. The main drawbacks of these studies are the following: destructive, possible contamination during disassembly of the cell and lack of information on dynamic process. The next tecnique represents a valid alternative.

2.7.3 EIS

Electrochemical impedance spectroscopy (EIS) is an analytical technique which is very compelling because it allows an in-situ, non destructive analysis and it is suitable to enlighten the electron and mass transfer. Furthermore test itself is simple to use and rapid. EIS consists of application in input of a constant voltage or a constant current over a range of frequencies (usually from 100 kHz to 10 mHz) and measuring in output current or voltage response, respectively. Usually, the amplitude of the applied excitation signal is around 10 mV (hence non destructive). An important assumption is the pseudo linearity so that a sinusoidal input will lead to a sinusoidal output, as shown in Figure 2.15. In this regard, it is a good practice to perform an open-circuit voltage (OCV) measurement before the beginning of the test so that voltage is stable during the experiment [64].

The generalization of input signal is

$$E = E_0 sin(\omega t) \tag{2.6}$$

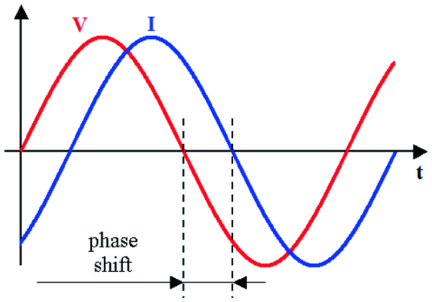

Figure 2.15: A voltage (input)-current (output) in EIS test. Adapted and reprinted with permission from [65]

The related output can be written as

$$I = I_0 sin(\omega t + \phi) \tag{2.7}$$

with ϕ indicating the phase shift. The equation governing the test is the generalized Ohm's relation in which:

$$Z = \frac{E}{I} = \frac{E_0 sin(\omega t)}{I_0 sin(\omega t + \phi)} \tag{2.8}$$

Data can be plotted in two different ways, mainly with imaginary part vs. real part (better known as Nyquist's plot) or as phase over frequencies (Bode's plot), as depicted in Figure. 2.16.

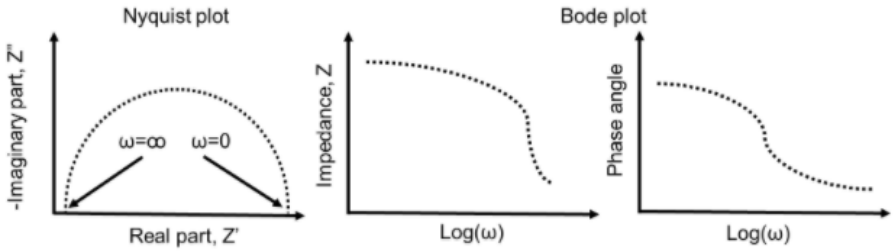

Figure 2.16: At sx Nyquist plot, at dx Bode plot. Adapted and reprinted with permission from [66].

The major challenge lies in interpreting data: the spectrum collected has to be associated to electrical components which respond in almost the same way in that frequency range, at the end an equivalent circuit is derived. This can be done with the aid of a software such as ZView®, in which is possible to draw a circuit model and fit the data.
The main components are three: resistor, capacitor and inductor. Their impedance can be described as shown in Table 2.1. To model the graph obtained, mathematical expedient are used. For instance the constant phase element (known as CPE) is a capacitor with a constant phase, which was created to represent the behaviour of semicircle. A step forward is the association of the just mentioned equivalent circuit to conceivable physical phenomena occurring in a battery. The points considered significant for the scope of this work are described in the following subsections.

Component	Impedance
Resistor	R
Capacitor	$1/j\omega C$
Inductor	$j\omega L$

Table 2.1: Impedance formula for the most important circuital elements.

$\mathbf{R}_b$

R_b is the equivalent series resistance of the system and it corresponds to the intersection with x-axis in the high frequency range.

Charge transfer resistance

The charge transfer resistance (R_{ct}) is the resistance that electrons encounter when they are transferred between two different phases (for instance, between electrode and electrolyte). Graphically, it is the point of intersection with x-axis at medium frequencies. The process of charge transfer is an interfacial process, hence it occurs at the surface where multiple elements are present, such as SEI layer. This makes the R_{ct} a more complex parameter to be evaluated.

Double layer capacity

The variation of electrode potential is accompanied by the formation of double layer on the electrode surface. The charged surface of electrode attracts a counter charge in the electrolyte. Close to this layer, ions dispose in such a way that they balance diffusion and electrostatic forces. It comes out a double layer which can accumulate charge and in this context it is represented by a capacitor. This process is a non Faradic phenomenon: no reaction such as oxidation or reduction are produced, instead charge is transferred by diffusion.

Constant phase element

A constant phase element (CPE) is a capacitor with phase kept constant. Its impedance is equal to:

$$Z = \frac{1}{Cost * (i\omega)^p} \tag{2.9}$$

The value of p depends on the ideality of the system and it ranges from 0 to 1, with this latter representing an ideal system. It is useful to model the real system because the capacitor is not suitable to model non smooth surface and other non ideality.

Warburg's impedance

In low frequency regime it is common to see a straight line with a slope around 45°. In this region, diffusion mass transfer is the limiting process. It is representend in the equivalent circuit as a Warburg's element that corresponds to a CPE with the p parameter equal to 0.5. The deviation (for instance an higher angle than 45°) is associated to the other capacitive effects, hence if this is the case a CPE rather than a Warburg's impedance

should be used. As mentioned in Chapter 2, a SEI layer is usually present and it allows the ion transfer, so in EIS it has to be taken into account. Its effect is evident in the high frequency region and it can be modeled by a capacitor and a resistance.

To understand the equivalent circuit it is possible to start from Bode's diagram. From this, a plateau at 0° corresponds to a totally resistive behaviour, while a -90° to an entirely capacitive behaviour.

2.7.4 FE-SEM

This technique is an ex-situ analysis often used in developing battery materials. SEM differs from a FE-SEM instrument for the source of electrons. The latter has an electron gun, which has a smaller spot size hence it produces clearer images. There are several modes to use it and they are distinguished for the electrons detected in output. In this context, the secondary electrons (SE) are exploited and the information collected regards the topography of sample surface. Secondary electrons result from the inelastic interaction between the electron source and the sample. The detector is an Everhart-Thornley system, which is composed of a scintillator in a Faraday's cage positively charged, so that electrons are attracted and collected. The scintillator accelerates electrons and transforms them into light. Then, they pass through a photomultiplier. It is therefore useful in this research to compare the pristine material to the cycled electrode, to reveal any change in topography correlated with exfoliation or similar degradation processes.

2.7.5 XRD

The X-ray diffraction tecnique is a characterization technique useful to detect crystalline phases and unit cell dimensions. In such a structure, the instrument uses the phenomenon of diffraction between interlayers and the wavelength, in particular the constructive interference between an input wavelength and d-spacing. The basic equation which govern its working principle is

$$n\lambda = 2dsin(\theta) \tag{2.10}$$

The diffracted rays are detected and multiplied. The graph plot the intensity versus the angle related to Bragg's equation. It can also be detected any change in interlayer distance. For an amorphous material, on the other hand, no evident peak can be noticed.

Chapter 3

Instruments, methods and tests

The experimental part was carried out at DISAT department, in the Electrochemistry Group. The structure of this chapter will be as follows: the first part will be a description of the instruments used to manifacture and to assembly the electrodes in two different cell configurations (coin cell and T-cell). A second part will describe tests and conditions used to assess the electrochemical performances.

3.1 Instruments for fabrication and testing

3.1.1 Ball milling

The ball milling MM400 Retsch in Figure 3.1 is the instrument used to uniform the slurry, previously mixed. It has two screw-top grinding jars in which one contains the sample and the other is useful to balance the weight. The device imparts an oscillatory movement regulated through the frequency. The latter and the time are the features that can be set by the operator.

Figure 3.1: Ball Milling equipment.

3.1.2 Automatic film applicator

This instrument is used to apply layers with a thickness of few micrometers. The thickness can be tuned by varying the height of the doctor blade, an instrument made of stainless steel which forms the layer by passing over the paste. It is set manually by the operator. Another parameter that can be tailored is the rate of the instrument guide. It goes from 50 to 150 mm/s. The rate in this project was set at 50 mm/s.

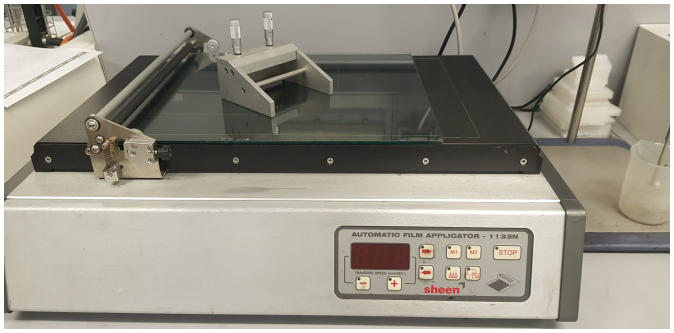

Figure 3.2: Film applicator and doctor blade.

3.1.3 Cutter

The manual cutter shown in Figure 3.3 is used to cut the electrode in disks of 15 mm or 10 mm, for coin and T cell configurations, respectively.

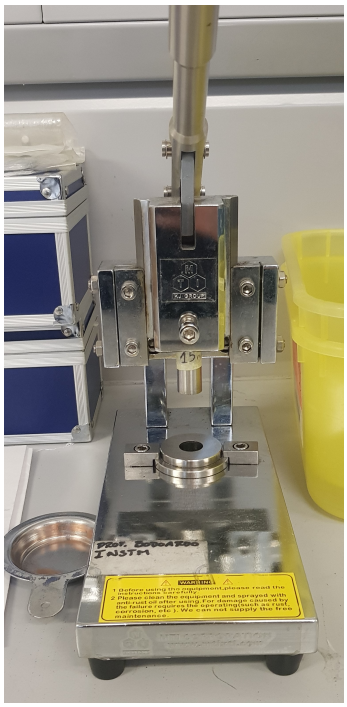

Figure 3.3: Manual cutter.

3.1.4 Glove box

The glove box is a chamber with a protected atmosphere (filled with argon), in which the levels of oxygen and water are very low (below 5 ppm in this particular case). It is the most important instrument by the moment that potassium is highly reactive towards moisture and oxygen and their presence can be either detrimental for the performance and dangerous for the operator. The assembly of cells and the preparation of the electrolytes are performed in this box. The MBraun Labmaster Pro is the one used in this project and it is shown in Figure 3.4. Two gloves allow manipulation of objects inside the chamber. The box has two ante-chambers, one smaller and the other bigger, fundamental because they enable introducing stuff in the protected environment. Each time materials and components have to go in, it is necessary to follow a procedure not to contaminate the atmosphere: in particular, a washing process consisting of three similar steps of evacuation and argon filling are performed to assure an inert atmosphere in the ante-chamber too. The big ante-chamber is used to bring in bigger objects. The argon is provided by argon tanks.

Figure 3.4: Glove box.

3.1.5 Glass oven drying

The Glass Buchi Oven B-585 is used to eliminate solvents and any organic impurities via temperature and vacuum. The system, as shown in Figure 3.5, is composed by a glass tube provided with a stopcock. A metal case surrounds the tube and resistances provide heat. The top of the stopcock has a hole that, during the process, is connected to the vacuum pump. The container in which samples are disposed is made of glass and a

NBR O-ring guarantees vacuum sealing. Time and temperature are the two controllable parameters which can be set and easily controlled in the display.

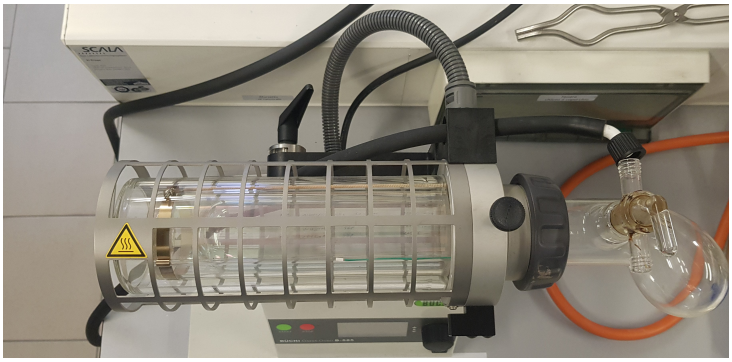

Figure 3.5: Buchi oven.

3.1.6 Crimper

This instrument is used to seal coin cells. The coin is inserted in the lower part and through digital control it applies a pressure that can be set by the operator.

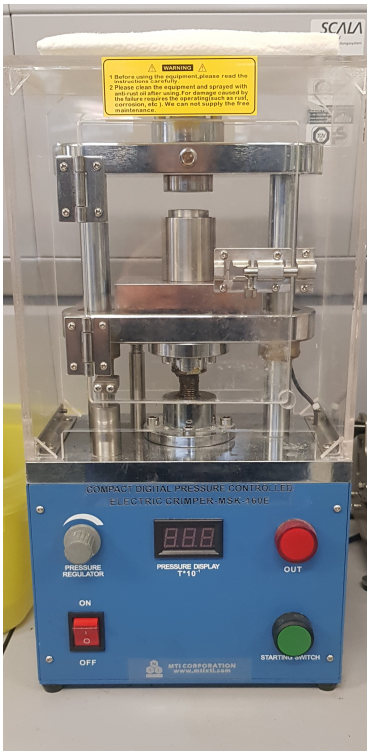

Figure 3.6: Crimper.

3.1.7 Dry room

The dry room is a room with very low humidity conditions. In this project, it was used to disassemble coin cells for post mortem analyses, which consist of FE-SEM and XRD

measurements. For the first, the electrode was cut in smaller pieces and washed in the solvent, in order to dissolve salts deposited on the electrode surface during cycling. For XRD, the active material was scratched from the cycled electrode and the powder was analyzed.

3.1.8 Tester instrument and data acquisition

Cycler

The cycler instruments adopted are Arbin cyclers. These instruments have several channels (8 and 16 the ones exploited in this project). The software for data process is MITS Pro, which provides an user-friendly interface, it allows data acquisition and data analysis.

Potentiostat

The potentiostat used is the VSP3-e Biologic potentiostat. It has four channels. Data were processed by EC-Lab® software. Cyclovoltammetry and EIS tests were completed in this instrument.

The data were analysed and plotted via OriginPro software. In order to obtain specific capacity, the charge-discharge capacity values were divided by the active mass (see its definition in section 3.3). The differential analysis of charge-discharge curves (dQ/dV) was performed exploiting interpolation/differentiation tool in the software. The EIS data were plotted using Origin, while fitting was performed via ZView.

3.2 Preparation of the electrode

In general, the procedure used is similar to different materials. All materials were used as supplied by the corresponding companies and they are listed in Table 3.1.

Material	Supplier	Particle size	Specific surface	Cost (100 g)
Graphite SLS30	Imerys	< 35 µm	7.5 m^2/g	
MoS_2	Sigma Aldrich (99%)	< 2 µm	-	93 €
SuperP	-	-	62 m^2/g	225 €
C45	Timcal		45 m^2/g	300 €
Potassium	Sigma Aldrich		-	435 €
CMC	Daicel	-	-	

Table 3.1: Material features from datasheet.

The powders of active material and conductive material are weighted on a Radwag, AS 220C2 balance. The binder in liquid state was made of a solution of sodium carboxymethyl cellulose CMC in water (grade Mill-Q®) at 5%. The binder was placed in a micro tube (2ml volume) with two zirconia spheres to help the subsequent mixing. The powders are constituted of the active material and a conductive additive. These were crushed in a mortar to disagglomerate particles before being introduced in the micro tube. In order to help an even dispersion a solvent was used; i.e. water or n-methyl-2-pyrrolidone (NMP) in the experimental part and they were added with the help of a pipette. To make it homogenous the sample was placed for 15 min at 30 Hz in the ball milling machine. To prepare the full electrode a collector is needed. In this case copper is used, so a copper foil is cut and placed on the automatic film applicator. The blade runner was set manually to 200µm height. Ethanol was used to clean and help adhesion with the plane of the instrument, on top of the foil some droplets of highly purified water was put on to help wettability with the aqueous based paste. Generally speaking, the liquid to help wettability is the same used in the slurry. The electrode is left to dry overnight and the result is shown in Figure 3.7.Next, it is cut in disks of 15 mm and 10 mm with manual cutter. The last step before assembly in the glovebox is to dry the disks for 4 hours at 120℃ in a Buchi glass Oven B-585.

3.2.1 Electrodes

MoS_2

Material	Percentage (%)
MoS_2	80
C45	10
CMC	10

Table 3.2: Composition of the electrode with MoS_2 as active material.

The total mass is 0.25 g. The solvent used is water in a volume of 500 µL.

Figure 3.7: Graphite slurry pasted onto copper foil after drying

Graphite

Material	Percentage (%)
Graphite	90
C45	5
CMC	5

Table 3.3: Composition of the electrode with graphite as active material

The total mass is 0.2 g. The solvent used is water in a volume of 500 µL. Artificial graphite can be synthesized by graphitizing non-graphitic precursors (e.g. petroleum, coal) in a non-oxygen environment at high temperature above 2000 ℃.

SuperP

Material	Percentage (%)
SuperP	80
PVDF	20

Table 3.4: Composition of the electrode with SuperP as active material.

In this case, the solvent is NMP and it was added for a volume of around 900 µL on a total of 0.1 g because of the low density and the micro-tube volume constraints. PVDF was in solution at 8% concentration in NMP. For this system, the drying of the electrode was carried out in an oven at 50 ℃ for 90 min.The composition found in the table results from several attempts in which the percentages of Super P and binder were 95-5, 90-10 and finally 80-20, which was the only one to have enough mechanical stability to be cut in disks and not to detach from the copper foil. SuperP carbon black is formed from a partial oxidation of petrochemical precursors. Its peculiarities are a large specific surface area (confirmed by datasheets' comparison too) and excellent electrical conductivity,

reason why it has been used as a conducting additive in the electrodes to improve the electronic conductivity in alkals-ion-based chemistry batteries [67]. It has been used as active material of an anode electrode in both LIB and SIB batteries.

C45

Material	Percentage (%)
C45	90
CMC	10

Table 3.5: Composition of the electrode with C45 as active material.

The material used is a conductive carbon black Super C45. In electrodes with MoS_2 and graphite as active material, its role is as a conductive additive. The total mass is 0.1 g because of the low density and the micro-tube volume constraints. The solvent added is water for a volume of around 900 µL. As with the Super P, so with C45 different percentages of binder-active material were tested with 90-10 ratio, resulting as that with enough mechanical stability. No further information were available about synthesis methods.

3.2.2 Preparation of the electrolyte

The electrolytes used in this project are two: KPF_6 at 0.8M in EC-DEC in 1:1 and KFSI salt 0.8 M in DME. The first system was prepared in the glove box, the total volumes of 2.5 ml of DEC and 2.5 ml of EC were left at 90 ℃ for 3 h to have the right viscosity. After 2 days, the solution was filtered. A second type of electrolyte studied is the KFSI 0.8 M in DME. Salts and solvents were provided by Sigma Aldrich and they were used as received.

3.2.3 Half cell assembly of a coin cell

In order to test different materials, the half cell configuration and not the full cell is used. This is useful when exploring new materials. The components of an half cell are listed in Figure 3.8.

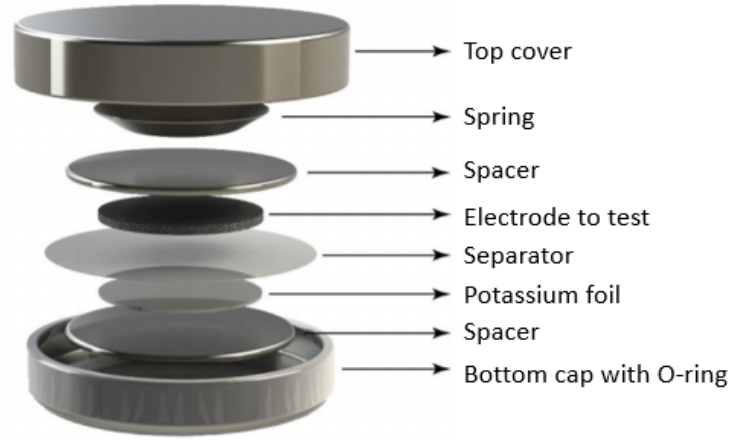

Figure 3.8: Schematic configuration of a coin cell components. Adapted and reprinted with permission from [68]

The system is therefore composed of an anode, which is a potassium foil, and a cathode, which is the material to be tested. It results conceivable this configuration because in [69] it was demonstrated that the plating-stripping of potassium experiences an overpotential reasonably low and acceptable polarization, therefore potassium can be used as the counter electrode in half-cells. Potassium metal disks were obtained from potassium cubes stored in mineral oil, it was cut in smaller pieces and with a rolling pin it was thinned. Then, a punching tool of 16 mm diameter was used to obtain a disk that was placed on the separator. This constitutes the anode of the cell. On the top of this, a Whatman glass fiber separator divides electronically the two parts of the system. At this point the separator is wet through a pipet with 12-13 drops of electrolyte. Next step, the electrode prepared is weighted on a balance and it is positioned on the separator. Lastly, another spacer was positioned between the electrode and the top case, which closed the cell. Spacers are useful to guarantee a mechanical support to electrodes. At this point, the cell was brought out the glove box and sealed with the crimper at 5 bar. A bench multimeter was used to asses the potential, thus the absence of a short circuit.

3.2.4 Assembly of a T-cell

The shape of this cell is the one shown in Figure 3.9, hence the name. The main difference is the number of electrodes: in a coin cell there are two electrodes, while in a T-cell there are three electrodes: a working (WE), a counter (CE) and a reference electrode (RE). In this configuration there is the control of potential between WE and RE while it is measured the current between the WE and the CE. This cell is also assembled in the glove box, the working electrode was placed on a plunger and two Whatman glass fiber disks of 10 mm were placed on top of it. Nuts help plungers holding the right position during the test. The electrolyte was added abundantly to avoid drying problems during the test. Then,

the reference and the counter electrodes were made of potassium metal, with a procedure similar to the one used for the coin cell with 10 mm punching tool. The disks were placed on the top of plungers and closed with nuts. In between potassium reference electrode and the other plungers, another separator was put to avoid short circuit. At this point the assembled cell was taken out of the chamber and a multimeter was used to check the absence of short circuit. If this is verified, a parafilm is used to manually seal the cell.

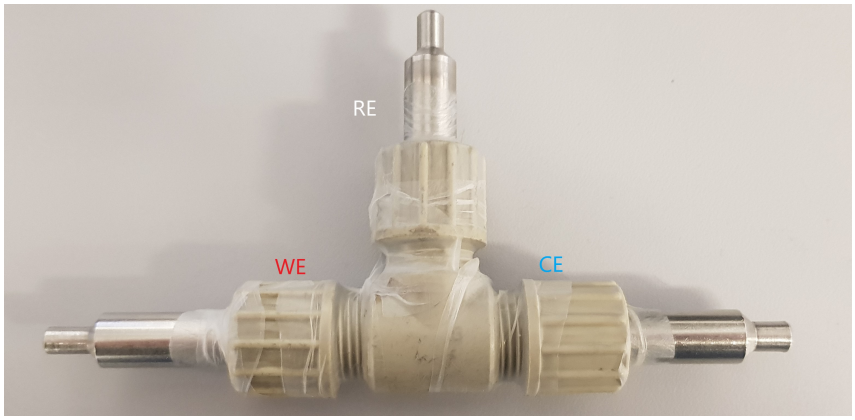

Figure 3.9: T-cell with label of the three electrodes

3.3 Tests

This work focuses the attention on the electrochemical performances of the systems studied, so the galvanostatic test of charge-discharge and potentiostatic test (ciclovoltammetry) were performed for each combination electrode/electrolyte. All electrochemical characterizations were carried out at room temperature.

3.3.1 Galvanostatic test

The coin cells were tested in an Arbin battery cycler instrument to perform charge-discharge tests. In this configuration, the discharge corresponds to intercalation and charge to deintercalation.
The main informations are about specific capacity, Coulombic efficiency, capacity retention and rate capability (definition of these terms are in the Appendix). In order to set the current, the following equation was used:

$$C = C_d * mass_A \tag{3.1}$$

where C is the current, C_d is current density and $mass_A$ is the mass of active material that is equal to:

$$mass_A = (mass_{el} - mass_{coll}) * Percentage \tag{3.2}$$

The $mass_{el}$ is the mass of the electrode that was measured in the glove box before assembling the cell. The percentage is the quantity of active material, given in Tables 3.2, 3.3, 3.4, 3.5. The mass of the collector was weighted at first selecting eight different samples (cut in disks of 16 mm) with an average weight of 0.015586 g. The measure was not

repeated by the moment that copper roll was the same for all the samples. In Table 3.6 the program used is presented.

Current density (A/g)	Number of cycles
0.05	10
0.1	10
0.2	10
0.4	10
0.8	10
1	10
2.5	10
5	10
0.05	10
0.1	100

Table 3.6: Test program to assess lab-scale PIB performances.

3.3.2 Potentiostatic test

The potentiostatic test performed is a cyclic voltammetry in the Biologic potentiostat. The cell used is a T-cell configuration. The program applied a potential cut-off of 0.01-3V versus the reference electrode at a scan rate of 0.1 mV/s for five cycles. Before the measure starts, an OCV monitoring for 45 min is executed.

3.3.3 Second step analysis

The good or bad results in these two tests determine the subsequent tests. Good performances, on the other hand, prompted other tests which aimed to understand either the mechanism of functioning and the performances at very high cycle number (aging). The systems which did not accomplish the tests just mentioned or the ones that had bad performances were not subjected to further electrochemical tests. FE-SEM analysis was performed on all the systems to reveal any morphological modification after cycling.

Aging test

In order to evaluate the performance at high cycle number, cells were cycled in an Arbin cycler, at which followed an EIS measurement in a Biologic instrument. The program used and current density values are shown in Table 3.6. An EIS test was performed

Stage	Current density (A/g)	Number of cycles	Repeat
Forming	0.05	3	1
Charge-Discharge	0.1	100	5(*)

Table 3.7: Aging program,*= not all the systems have accomplished 500 cycles

	Frequencies range	Amplitude
EIS	100 kHz-10 mHz	10 mV

Table 3.8: EIS parameters.

every 100 cycles of charge-discharge in such a way not to monitor only the ability to last many cycles number, but also to elucidate any degradation process involved.

EIS analysis for forming stage

In chapter 2, it was highlighted the importance of the SEI layer. In order to detect its formation, different techniques were exploited. In this context, EIS analysis was applied by the moment that SEI is an interface and EIS can detect it. To be more precise, an EIS was performed on T-cells for ten cycles after a charge-discharge at 0.05 (A/g). The program is shown in Table 3.9.

Stage	Parameters	
OCV	5min	
EIS	100kHz-10mHz	10mV
OCV	5min	
Discharge	0.05 A/g	0.01-3 V
Charge	0.05 A/g	0.01-3 V

Table 3.9: Program for the forming steps

3.3.4 Morphological analysis

In addition to the electrochemical analysis, FE-SEM secondary electrons and XRD were performed. The first one to asses if any change in microstructure was present before (pristine electrode) and after cycling, the second one for the cristallinity.

The samples were prepared cutting a piece from the for the pristine material, while the cycled electrode was recovered from the coin cell, washed in the corresponding solvent and after drying, it was placed on the sample holder. The samples for XRD analysis were obtained scratching the material on the copper foil, while scratching the material from the coin cell disks in the cycled coin cell.

Chapter 4

Results and discussion

In this section the results obtained will be shown and discussed. In Table 4.1 a summary table of test performed on each system is provided to guide the following part.

System	Test1	Test2
Graphite-KPF_6	✓	✗
Graphite-KFSI	✗	✗
$MoS_2 - KPF_6$	✓	✓
$MoS_2 - KFSI$	✗	✗
SuperP-KPF_6	✓	✓
SuperP-KFSI	✓	✓
C45-KPF_6	✓	✓
C45-KFSI	-	-

Table 4.1: Test performed for each system.

4.1 MoS_2-KPF_6

4.1.1 Electrochemical performances

Cell	M_a	D-cap 15	CE(%)	D-cap 100	CE(%)	D-cap 200	CE(%)
1	0.003371g	87.65	99.98	91.36	100	88.99	99.98
2	0.003211g	81.15	100	89	99.8	88.72	99.73
3	0.005211g	103.41	99.35	97.13	99.7	92.52	99.89

Table 4.2: Cells performance at 15th cycle, 100th cycle and 200th cycle.

Electrochemical performances show an initial specific capacity of 200 mAh/g which goes to 100-125 in the first ten cycles. The CE of the first cycle is around 63% , which is similar to the value found in literature[70]. This irreversible capacity loss is attributed mainly to the formation of the SEI layer [71]. On the other hand capacity stability is great: comparing the 10th cycle with the 100th the capacity retention is of 90%, which remains stable with a capacity retention of 97,4% between 100th and 200th cycle. The stable performances can also be noted in Figure 4.4 where charge-discharge curves are very close and potential window is almost the same, highlighting poor polarization phenomena. In Figure 4.38 different replica were plotted: cell1 and cell2 show a similar behaviour and are more stable while cell3 has higher performance at low current density but lower at higher current density. Moreover, at high current densities (see Figure 4.3) curves are steeper and capacity decreases a lot, for instance it goes to 20 mAh/g at 5 A/g, hence rate capability is low.

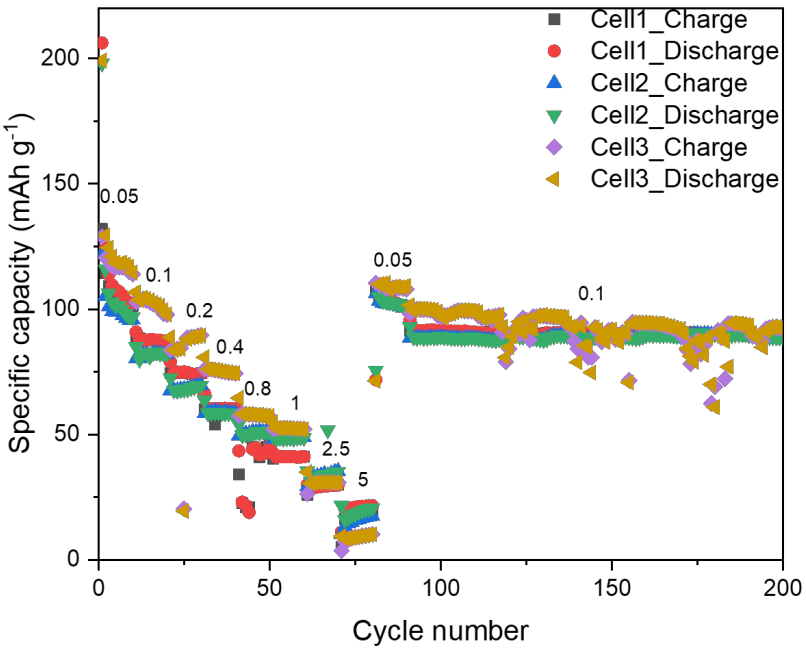

Figure 4.1: Specific capacity vs. cycle numbers, at different current densities (A/g) for MoS_2 with KPF_6.

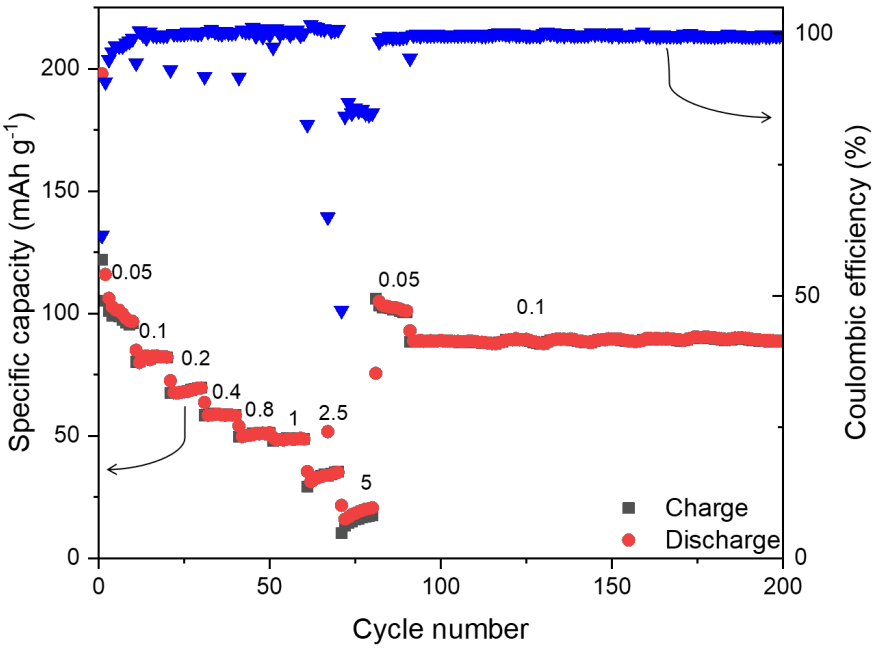

Figure 4.2: Specific capacity vs. cycle number and CE vs. cycle number for the best replica, MoS_2 with KPF_6.

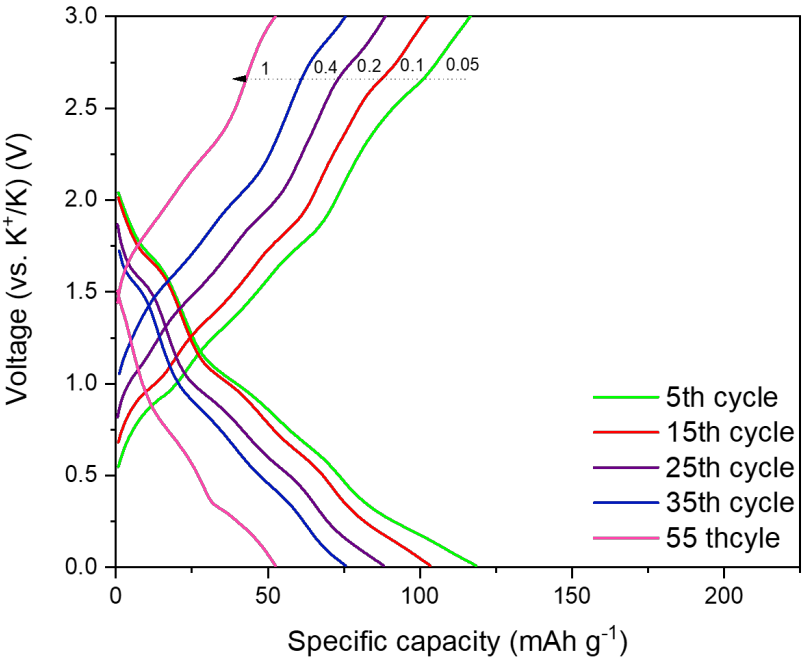

Figure 4.3: CD curves at different current densities for MoS_2 with KPF_6.

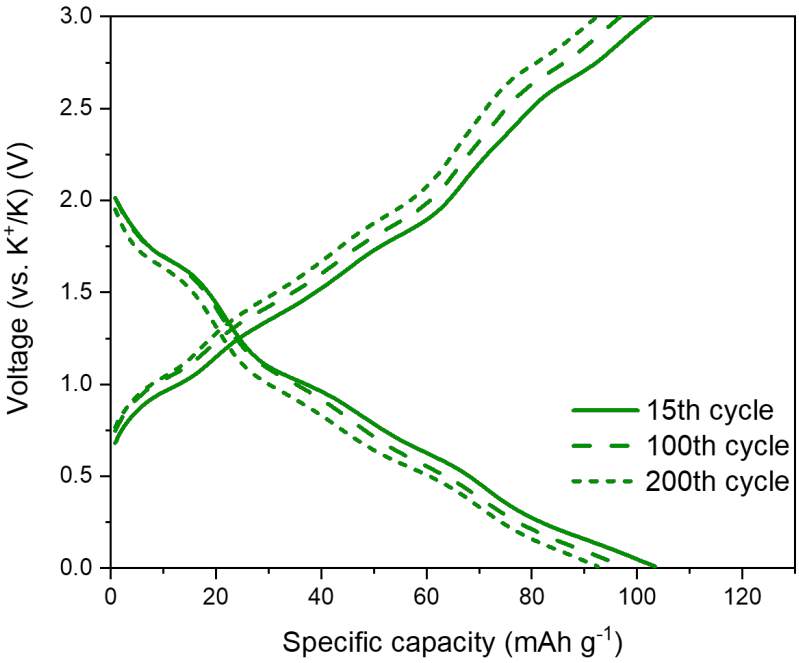

Figure 4.4: CD curves for MoS_2 at different cycle number (15,100,200).

4.1.2 CV

In order to study the mechanism of functioning in this section CV curves and dQdV vs. V curves will be studied. At first cycle, the cathodic branch in the voltammogram (Figure 4.6) shows three peaks while the anodic branch two peaks. The cathodic ones are at 1 V, 0.28 V and 0.01 V. The peaks were compared with other systems [72] and [73], in which the peak at 1 V was attributed to intercalation of potassium ions. The compound formed is K_xMoS_2 with a theorical capacity of 67 mAh/g. The storage mechanism below 0.8 V is ascribed to the conversion reaction of MoS_2 being reduced to metallic Mo and K_2S from the conversion of K_xMoS_2. The latter mechanism allows higher specific capacity. At the same time it can be irreversible or reversible. In literare both have been reported. The irreversible reaction means that Mo and K_2S do not recover to MoS_2 and this leads to poor structural stability due to shuttle effect of polysulfide, which contributes to rapid decay of electrochemical capacity [74]. The partially reversible conversion reaction has been reported in [41], where thee partially discharged products it is reversibly converted to MoS_2 after the charge process. In the anodic scan, it is observed only one small broad peak around 1.6 V, which could be interpreted as depotassiation [73] process and that is also present in subsequent cycle. It can be supposed that this is the case of a partially reversible conversion reaction. The anodic peak at 0.5 V can be related to the conductive additive (see the paragraph dedicated to C45). The subsequent cycles (2-5th) almost overlap indicating the reversibility of the reaction that takes place. In order to elucidate storage mechanism, dQ/dV vs. V curves at different current densities were reported in Figure 4.7. Four cathodic peaks correspond to four anodic peaks, at lower current densities. The reduction-oxidation peaks are coupled as follows: (0.2-1.31 V; 0.65-1.59 V; 1.03-1.89 V; 1.71-2.66 V). The number and position of peaks change with increasing current densities with an evident polarization phenomenon. The specific capacity in charge-discharge is higher than the theorical value due to intercalation, hence there is also conversion. Further studies are needed to discover the reactions involved as also suggested in literature [74].

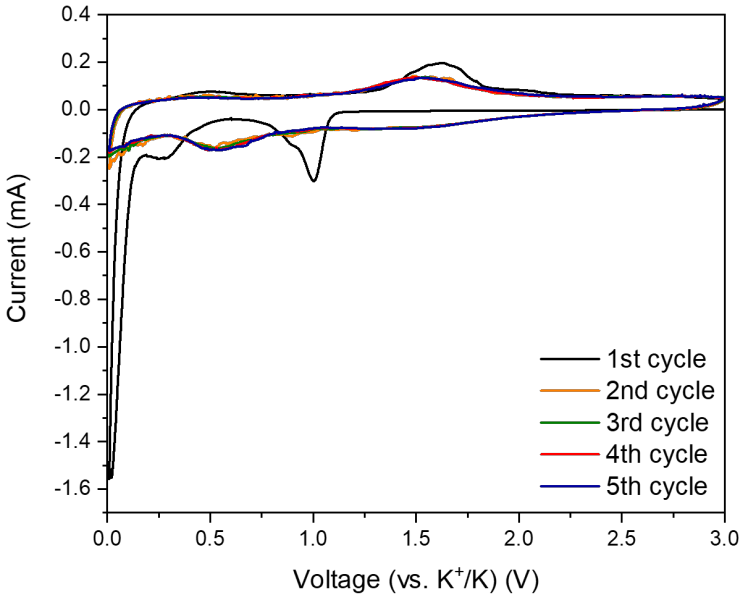

Figure 4.5: Voltammogram for MoS_2 with KPF_6.

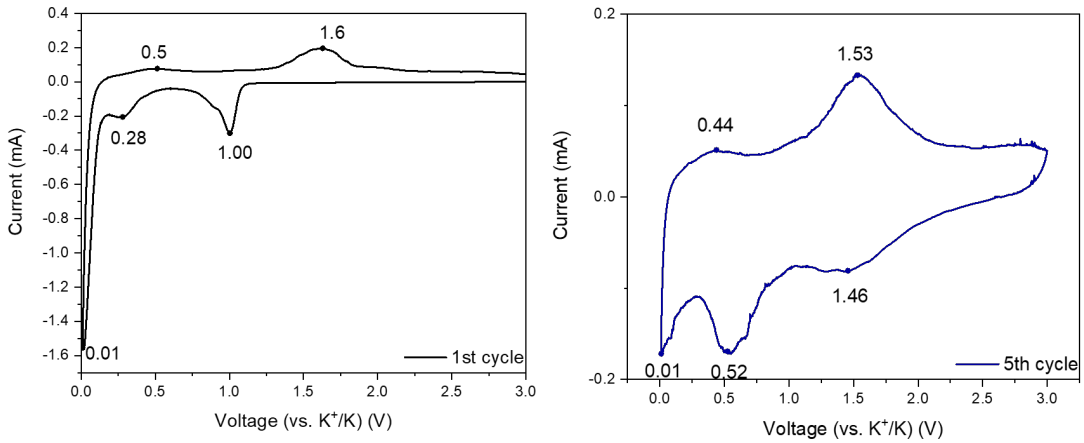

Figure 4.6: Voltammogram of cycle 1 and 5 for MoS_2 with KPF_6 and related peaks.

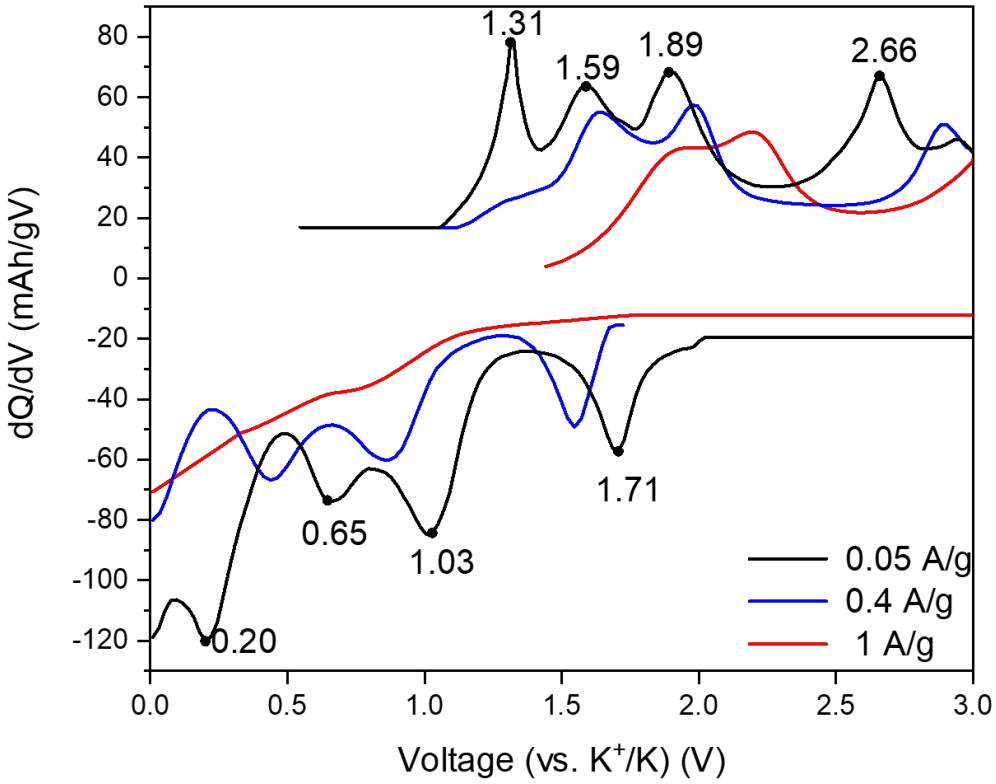

Figure 4.7: dQdV curve at different current densities for MoS_2 with KPF_6.

4.1.3 FE-SEM

The fresh electrode shown in Figure 4.8, depict a material with particle size in micrometer range (lower than 5 µm as confirmed in datasheet and found in literature for commercial Molybdenum disulphide). The morphology has a layered geometry (clear at Figure b) 4.8) with the conductive additive which is quite homogeneously distributed.
The cycled electrode (in Figure 4.9) compared to the fresh one shows similarities. The particles are still in the micro size range and the surface of particles does not have any relevant differences.

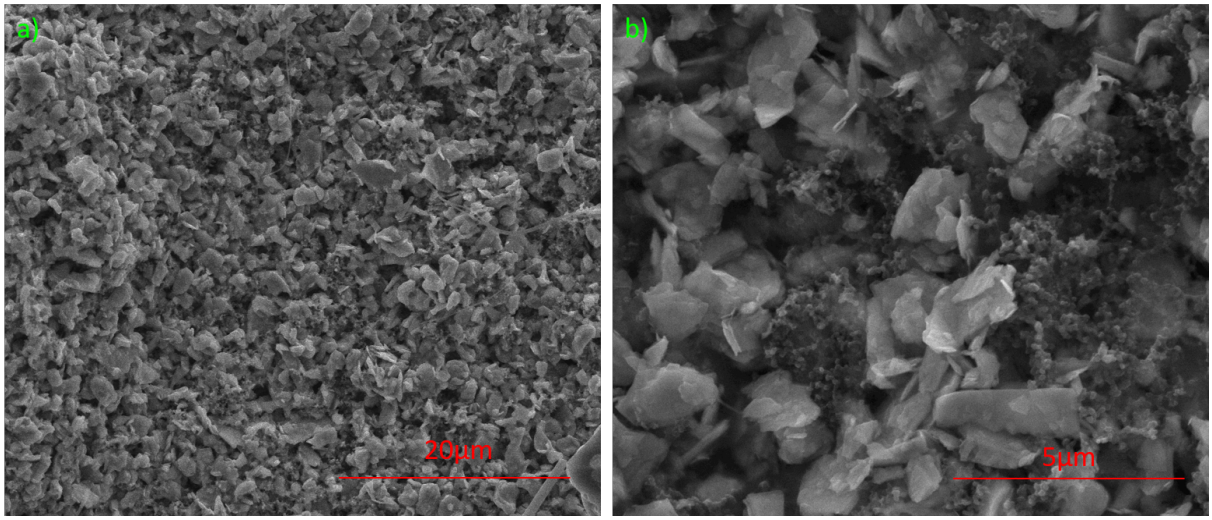

Figure 4.8: FE-SEM at different magnitude, fresh MoS_2 electrode.

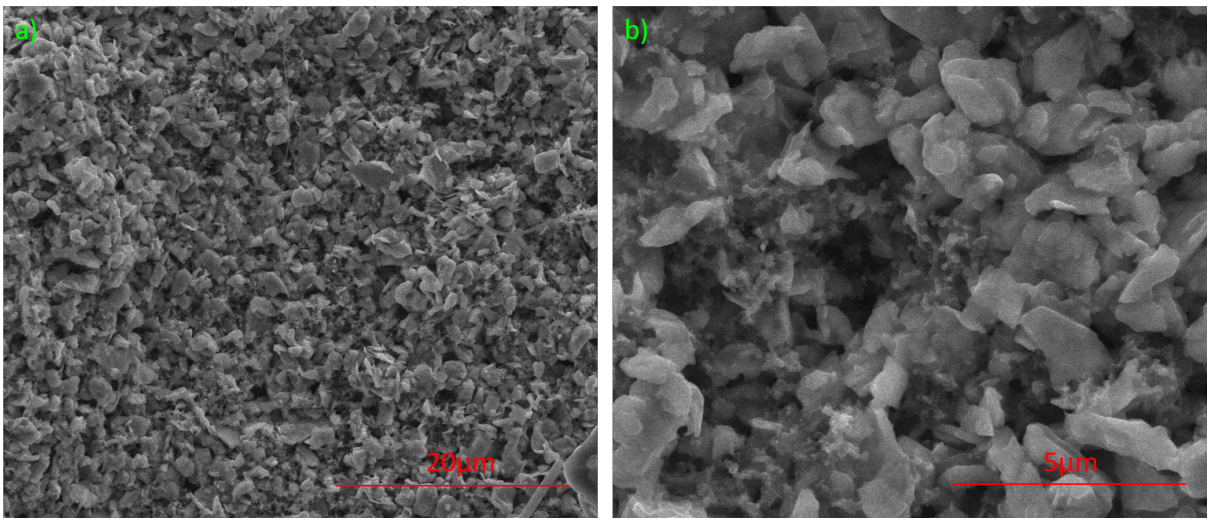

Figure 4.9: FE-SEM at different magnitude, cycled MoS_2 electrode with KPF_6.

4.1.4 Forming stage

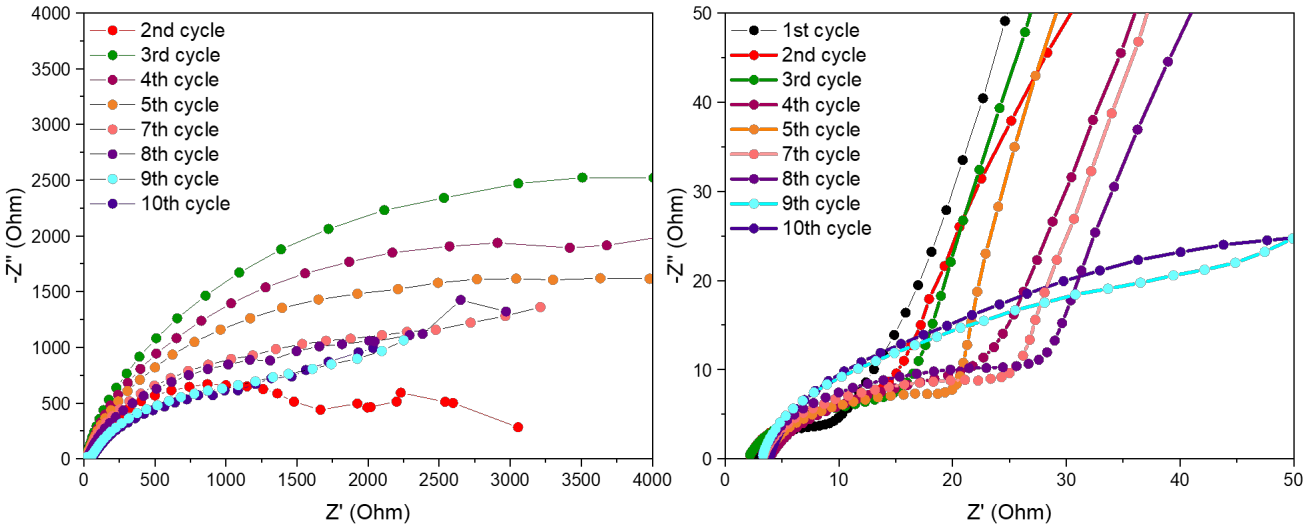

Figure 4.10: Nyquist plot in two different ranges; complete spectrum at sx, high and medium frequencies at dx, for MoS_2 with KPF_6.

The forming stage was evaluated with the program described in chapter 3. The first cycle is typical of a system electrode-electrolyte with an interface described by a semi-circle and a straight line in the low frequencies region which depicts the diffusion behaviour. Starting from the second cycle, in high and medium frequencies there is a depressed semi-circle and another semi-circle in low frequencies region. Upon cycling, a beginning of straight line becomes evident in particular at cycles 9-10. In order to fit the spectra obtained, the circuit in Figure 4.11 was exploited. The two semi-circles correspond to circuital elements R1-CPE1 and R2-CPE2. The third element represent the behaviour at low frequencies. In Table 4.3, the values given by the fitting process. The bulk resistance, indicated with R_b is stable and it has a value between 2.20-4Ω.

Figure 4.11: Model used to fit MoS2 with KPF_6 during forming stage.

The R1 and R2 resistances increase while R3 decreases. It is not straightforward to attribute the physical phenomena behind this trend. Upon cycling two interfaces are formed: one is attributable to SEI layer and the other one to the product of conversion. The R3 could describe the charge transfer resistance which is so high maybe due to semi-conductor material in the crystalline phase 1H-MoS_2.

Cycle	R1 (Ohm)	Error(%)	R2 (Ohm)	Error(%)	R3 (Ohm)	Error (%)
3	4.11	21.9	9.41	10.9	5490	1.14
4	4.38	34.8	15.13	11.9	4320	1.2
7	9.02	13.3	11.58	11.9	2193	1.4
8	10.88	8.5	10.89	9.7	2259	1.3
10	13.31	9.8	40.18	4.7	1646	1.8

Table 4.3: R1, R2, R3 values and related errors upon cycling for MoS_2 with KPF_6.

4.1.5 Aging test

The peformance are shown in 4.12. Both systems are not stable till 500 cycles. In 4.12 (sx) the specific capacity decreases steadly while in 4.12 (dx), for 200 cycles the capacity is around 120 mAh/g for both charge and discharge. In the following cycles the trend changes and charge capacity is higher than discharge. This phenomenon can be due to some oxidative processes (such as electrolyte degradation). In literature the explanation given for the is that SEI layer formed in KPF_6 dissolved in EC/DEC mainly consists of the reduction/decomposition products from the organic solvents, which are unable to effectively passivate the active material, leading to continuous electrolyte decomposition and capacity decay[75]. The abrupt change in electrochemical performances in cell 4.12 (sx) can be explained with EIS spectra in Figure 4.13. R_b value is correlated to the state of health of a battery and it can be noticed an increase upon cycling. Furthermore the depressed semi-circle which is usually associated at middle frequencies to charge transfer resistance increases. To end up, the part at lower frequencies which usually is a straight line representing diffusion is almost absent. In Figure 4.12 (sx) it can be noticed that between 100 and 200 cycles there is a consistent lowering of specific capacity and in the same interval the increase in resistance is the steepest among the intervals. At the same time the semi-circle correlated to charge transfer that also gets bigger. The behaviour of this parameter could explain the lowering of performances in fact it is increasingly difficult the transfer of charge.
A post-mortem analysis was carried out and two cells open. The first cell in Figure 4.14 (a-c) was subjected to charge-discharge while the second cell in 4.14 (b-d) to aging test. It is clear that the electrode is not stable mechanically and the Whatman separator is very different compared to the one in (a), showing a darker colour. This further confirms the hypothesys of electrolyte degradation and electrode instability, both phenomena being responsible of an increase of the overall resistance.

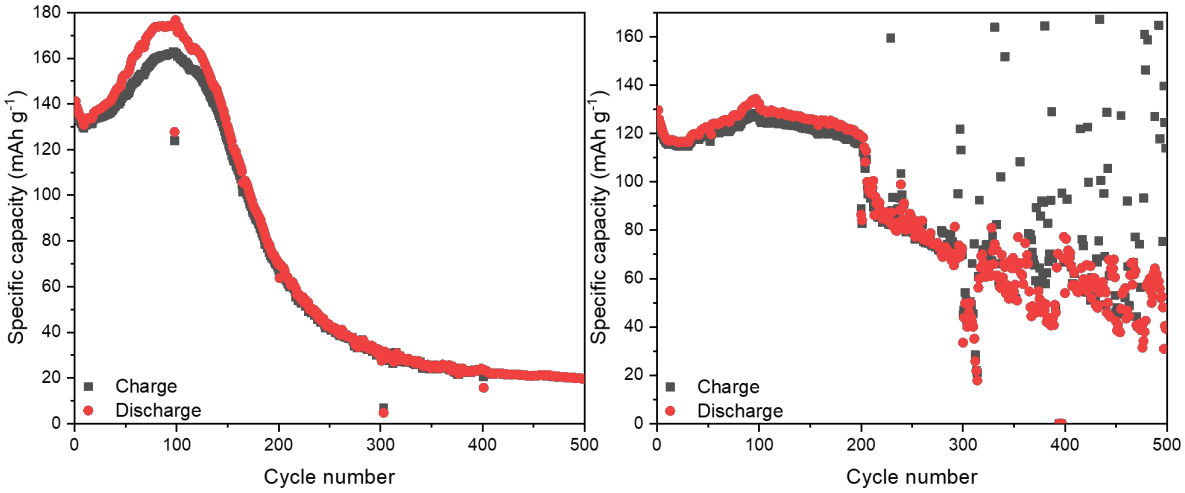

Figure 4.12: Specific capacity vs. cycle number, aging test at 0.1 A/g for MoS_2 with KPF_6.

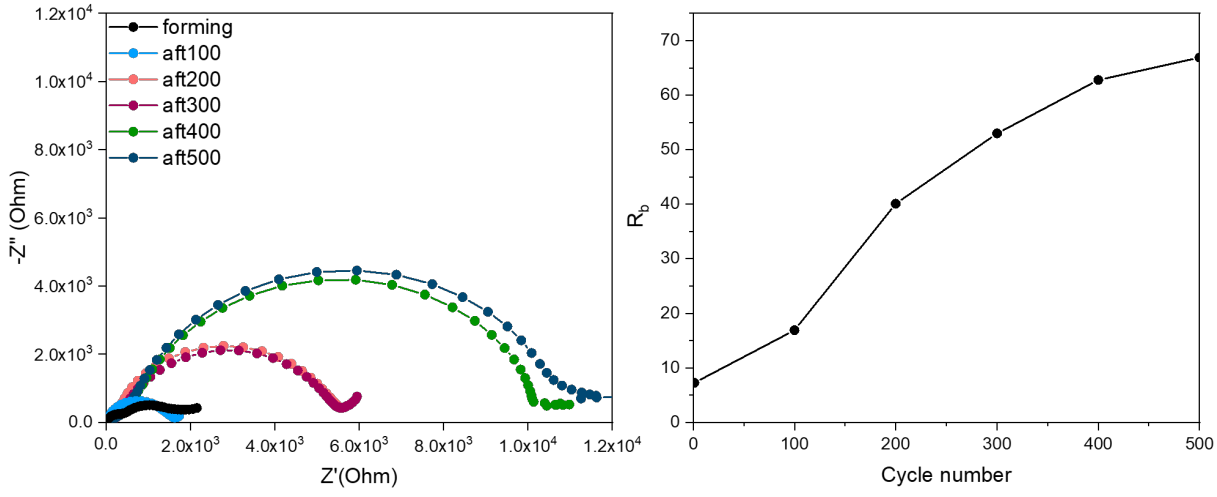

Figure 4.13: Nyquist plot recorded every 100 cycles during aging test for MoS_2 with KPF_6, aging test.

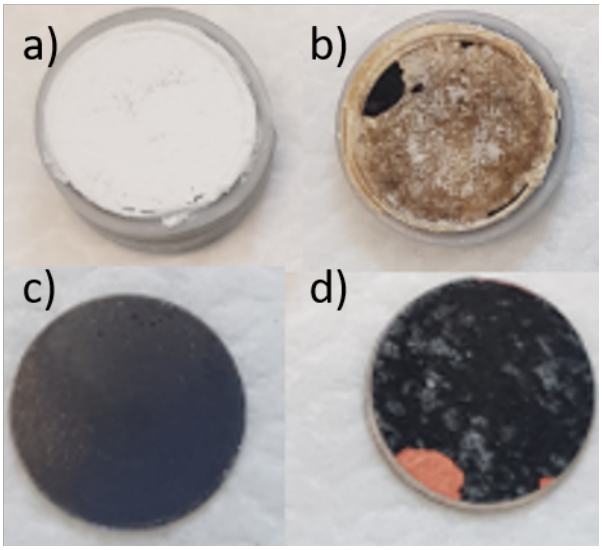

Figure 4.14: Post-mortem cells: a)-c) GF separator and electrode of a cell after test1 b)-d) GF separator and electrode after aging test.

4.2 MoS_2-KFSI

This system reveals an incompatibility electrode-electrolyte. Either galvanostatic and potentiostatic test did not succeed, not being able to complete the number of cycles decided. In literature the closest system is the one in [75], in which the electrolyte consisted of KFSI salt and EC:DEC, showing better performance that KPF_6. Concerning CV, only the two first cycles were obtained and they are reported in Figure 4.15. After that the system was not stable and curves not attainable. It can be noticed that there is a consistent difference between first and second cycle. The first one has three cathodic peaks (at 0.77V, 0.11 V and 0.01V) and two anodic peaks (a shallow at 1.41 V and a defined one at 2.29 V). In literature (for lithium ion battery) the peak at around 2.3 V was ascribed to the oxidation reaction from Li_2S to S [38]. The peak close to 0.8 V has been found for KFSI in DME based electrolyte and it is attributed to salt decomposition and SEI layer formation [51]. The second cycle has also three cathodic peaks but at different voltages (1.02 V, 0.29 V and 0.01 V). The anodic branch in the second cycle does not have any peaks.

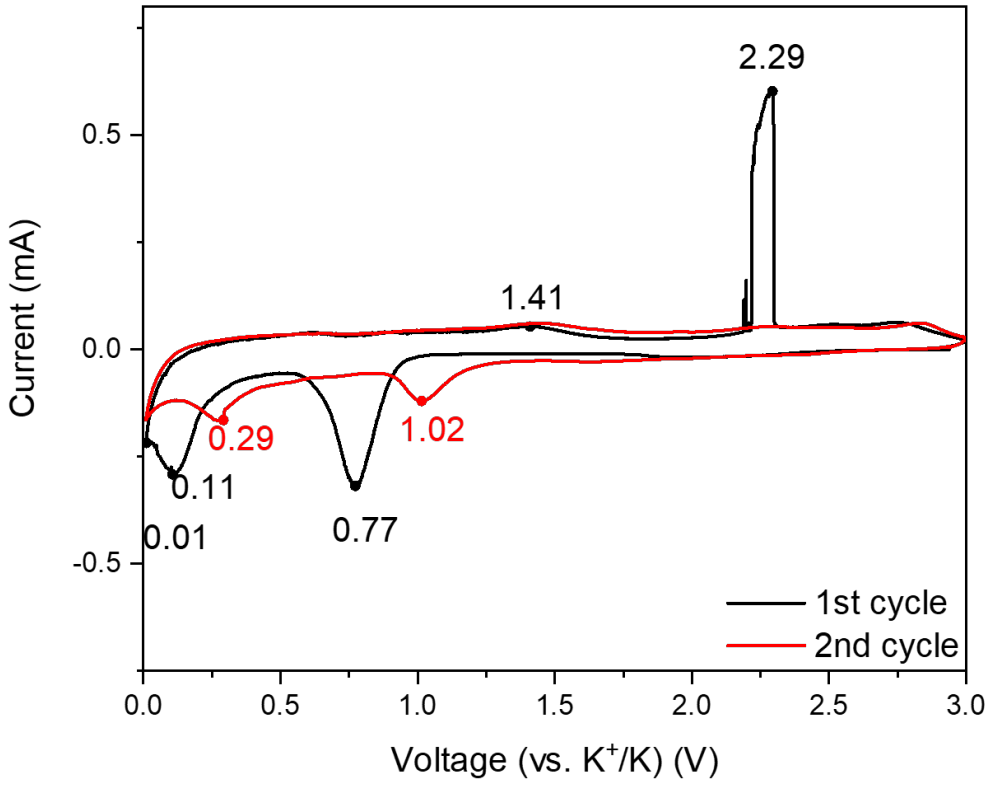

Figure 4.15: First and second cycle of CV test for MoS_2 with KFSI and related peaks.

FE-SEM micrographs show a very peculiar morphology, different for both pristine MoS_2 and MoS_2 in KPF_6. In Figure 4.16 the cycled electrode results different from the pristine. First of all is easy to notice that the electrode luck of mechanical coehsion with evident cracks along the surface. The Figure b) and c) show two different regions of the electrode representing the coehesive electrode b) while in c) some cracks are highlighted. The filament could be due to the binder while the tubular shape element could be due to potassium plating. The latter would be justified by the peak at 0.01 V (4.15). At higher magnification, in the compact area d), particles are pretty uniform even if the surface is not as smooth as the pristine one. In e) there is the formation of a crystalline phase that needs further investigations.

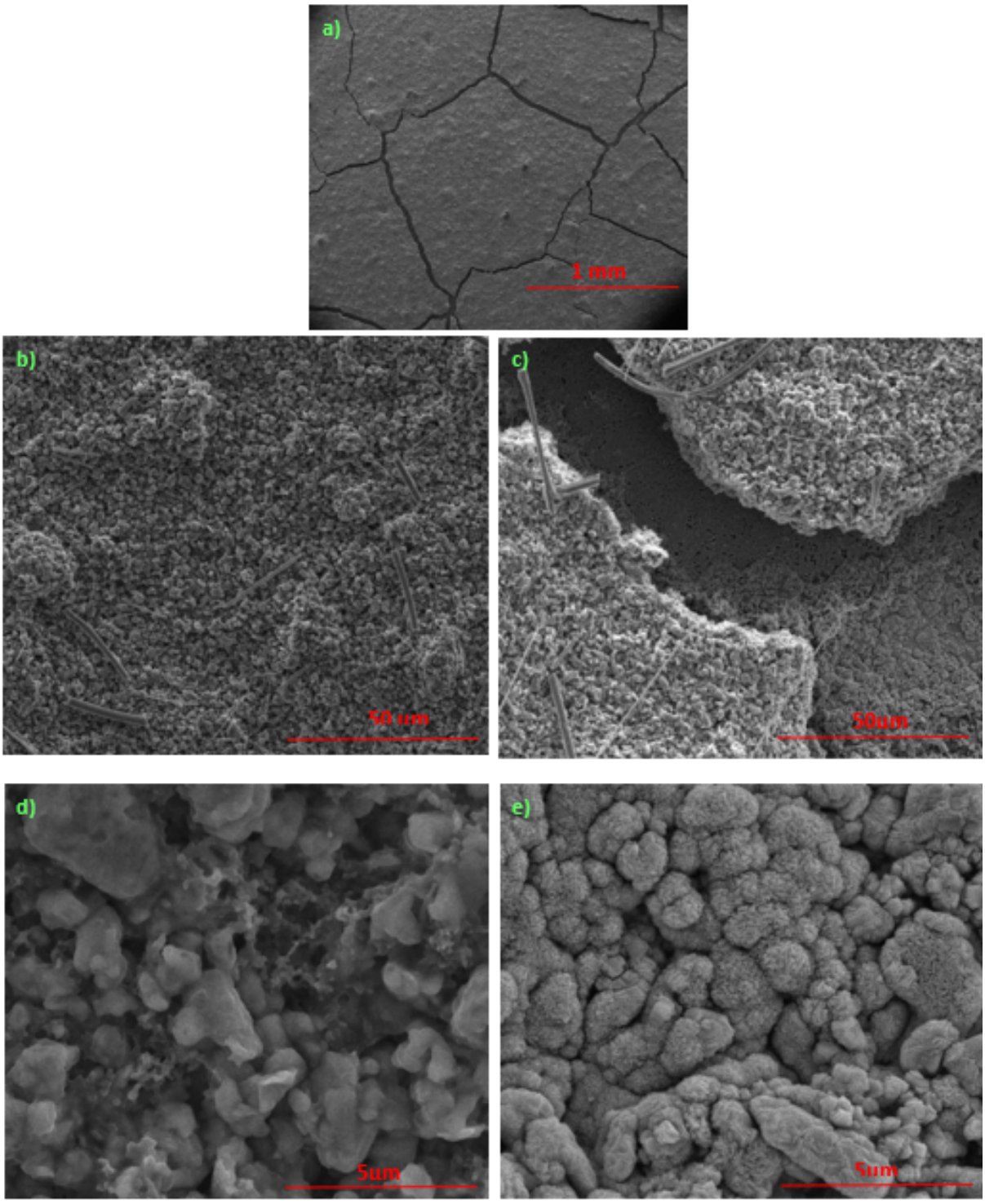

Figure 4.16: FE-SEM images at different magnification of cycled MoS_2 with KFSI.

4.3 Graphite-KPF_6

4.3.1 Electrochemical performance

This combination shows bad performances in term of capacity. In the graph in Figure 4.17, is evident a fast capacity decay: the specific capacity in fact goes to less than 10 mAh/g in a few cycles. The trend is similar for both cells. In literature graphite with this electrolyte, shows bad cycling stability and rate capability. The Coulombic efficiency for the same system is 47%. The low value has been attributed by the decomposition of DEC [76]. The results hence support the finding in literature. Despite the consistent difference in terms of initial specific capacity found in , the behaviour is similar. The same commercial graphite in [69] fail after 25 cycles. Looking at 4.18 is evident a huge effect of polarization between first and second cycle and from second cycle (at 0.05 A/g) and 15th cycle (at 0.1 A/g). This confirms the very poor rate capability.

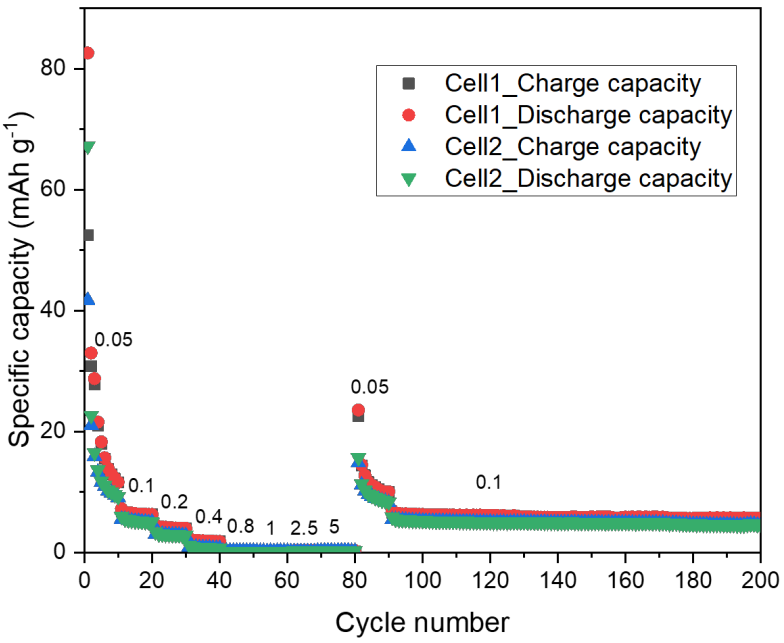

Figure 4.17: Specific capacity vs. cycle number , at different current densities (A/g) for Graphite with KPF_6.

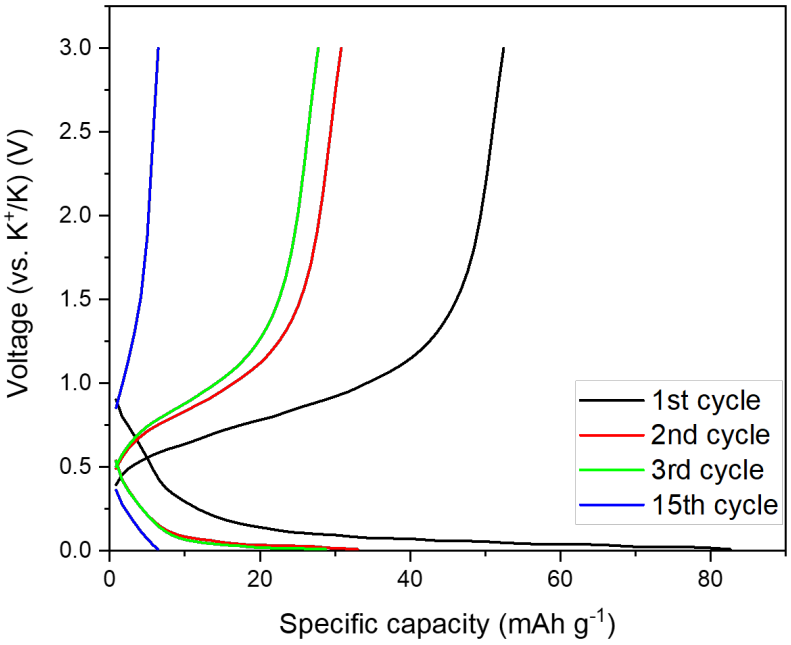

Figure 4.18: CD curves at different current densities for Graphite with KPF_6.

4.3.2 CV

The voltammogram in Figure 4.19 shows two peaks in the first cathodic branch, one at 0.73 V and the other at 0.1V. In the first anodic branch there are three peaks at 0.34, 0.47, 0.63 V. Upon different cycles, the anodic and cathodic peaks differ from the one in the first cycle. Coupling this information with the graph in Figure 4.17 where first cycle has a consistently higher specific capacity which decays in the subsequent cycles, it can be hypotized that some irreversible phenomena happen and that this means lower electrochemical performances. In literature, the phase transitions due to K-insertion show KC_36 firstly formed ranging from 0.3 to 0.2 V, then transformed into KC_{24} between 0.2 and 0.1 V, and finally changed to KC_8 at 0.01 V. In this case the cathodic peak does not reach 0.01 V indicating the lack of formation of KC_8 GIC. This is further confirmed by the capacity: the KC_8 brings a theorical capacity of 279 mAh/g, while KC_{24} around 90 mAh/g. The presence of the cathodic peak at 0.7 V is correlated with some phenomena electrolyte or SEI formation, in fact it is evident only in the first cycle. The K-extraction is described in literature as the direct conversion of KC_8 into KC_{36} compound at about 0.3 V, and then (above 0.5 V) it returns to a graphite with low crystallinity. In the following cycles the cathodic peak shifts at lower potential while the anodic branch has only one broader peak at 0.75 V. This polarization effect is evident in CV plot and in CD.

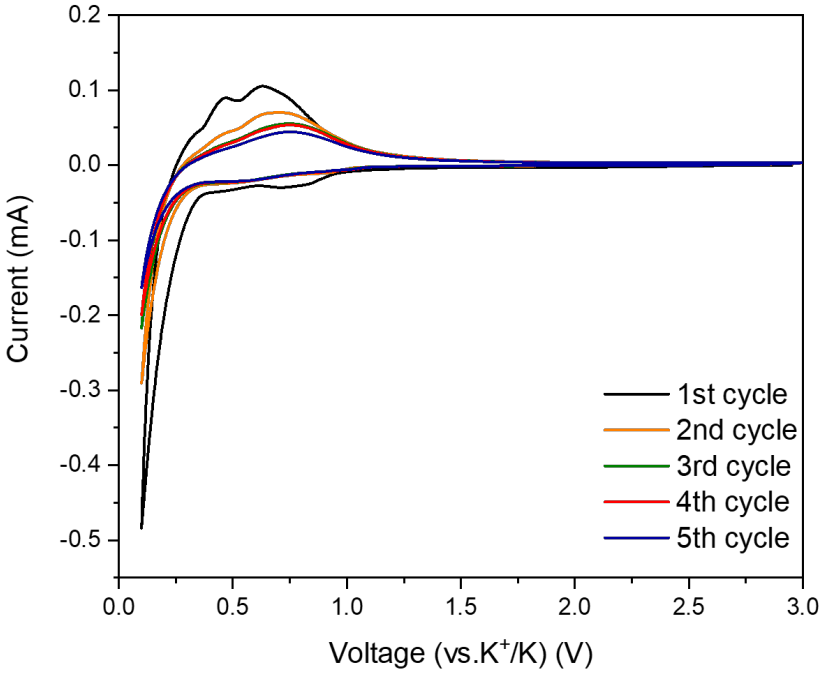

Figure 4.19: Voltammogram for Graphite with KPF_6.

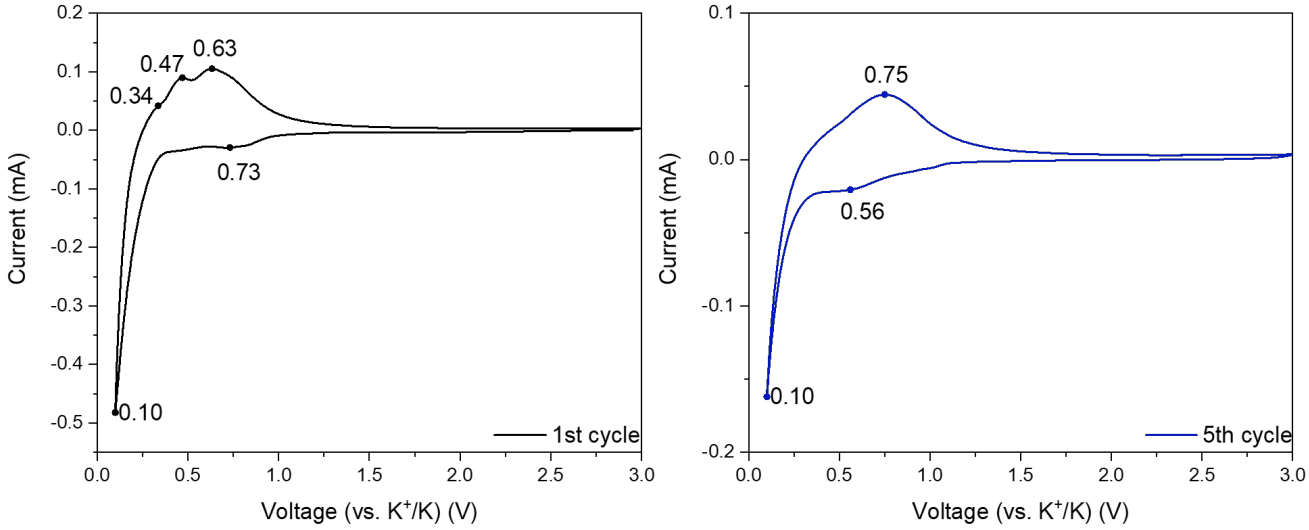

Figure 4.20: Voltammogram of cycle 1 and 5 for Graphite with KPF_6 and related peaks.

4.3.3 FE-SEM

The particles in the fresh electrode are quite large and the particles size distribution ranges from a few micrometres to 40 µm. At high magnification (Figure 4.21), the compact structure of the graphite particles is evident as the typical layered arrangement.In Figure 4.21 b) graphite has a typical layered structure with clean, smooth surface and sharp edges. The particle surface results a bit defective which can be due to ball milling process as reported in [69]. The carbon conductive is well distributed even if in some points it suffers of agglomeration. The cycled electrode in Figure 4.22, has almost the same size distribution particles. In the low magnified image (a) on the bottom left it is evident filaments due to the binder. The interesting fact is shown in the highly magnified image Figure 4.22 (b), in which the surface of the graphite could have an excessive SEI formation, this hypothesis is supported in literature where in [77], the continuous formation of SEI on K surface in EC:DEC electrolyte is responsible of cell fading because of an increase in impedance.

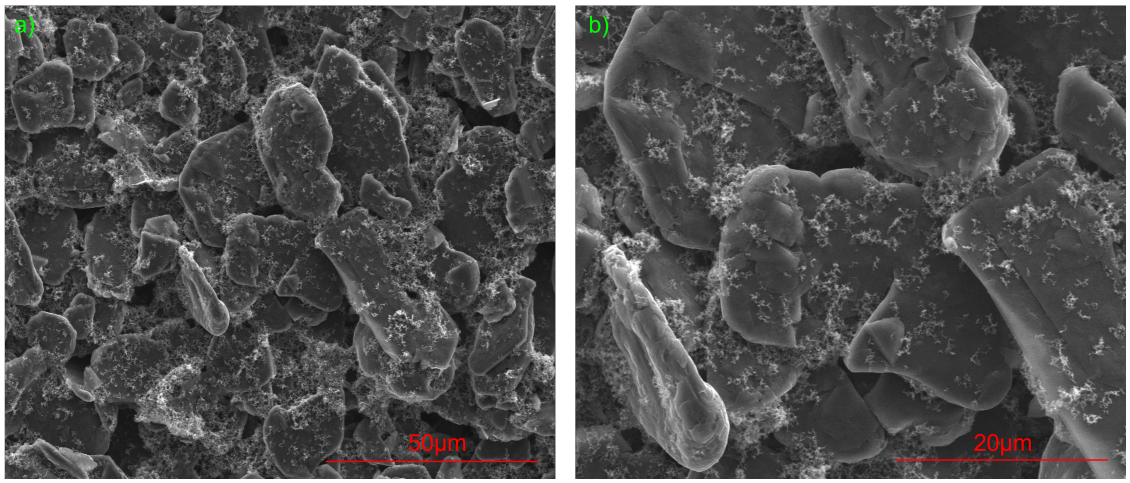

Figure 4.21: Fresh graphite electrode at different magnification.

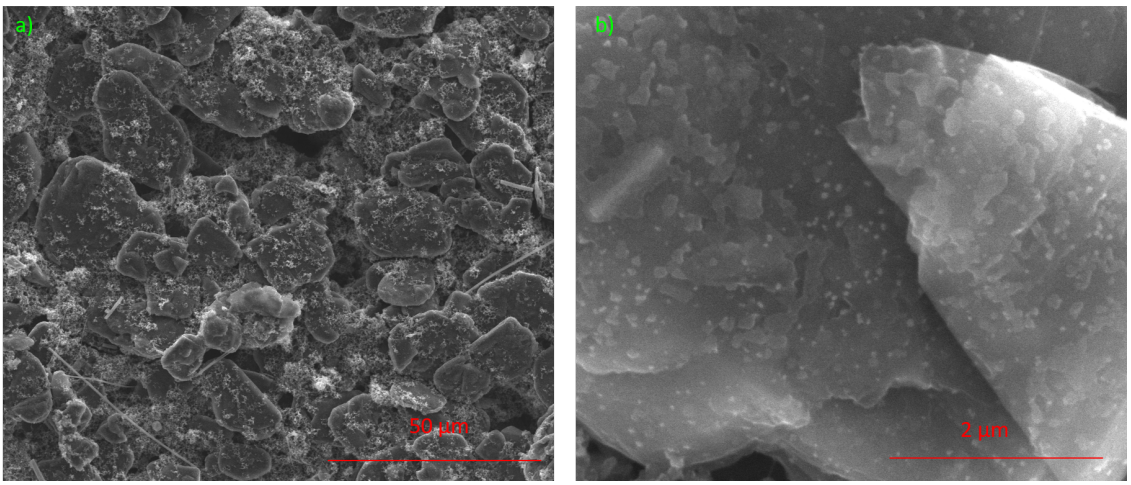

Figure 4.22: Cycled graphite electrode at different magnification.

4.3.4 Graphite-KFSI

This system shows high incompatibility between electrolyte and electrode. The charge-discharge did not accomplish the first cycle and the cyclicvoltammetry shows non attainable profile. In this, the electrolyte system is different. The influence of the solvent is reflected in the mechanism followed for the intercalation process, in fact in ether-based electrolyte ternary GICs can be formed in graphite through co-intercalation[78], in particular in systems where the concentration is not high. It has been found in [79], [80]that concentrated ether follows different interfacial reaction mechanisms compared with the dilute ether, in fact high salt concentration in high-concentration electrolytes or LHCE (localized high-concentration electrolytes) would switch the electrolyte decomposition from organic (decomposition of solvent) to inorganic based (decomposition of anion) products hence forming a denser SEI rich in inorganic. Looking at Figure 4.23 a), the cycled electrode has a similar distribution in term of particles size and the tubular like structure can be attributed to the potassium plating [81], in addition surface is not as smooth as in pristine electrode but rough. This is also confirmed at higher magnification (b) where also is noticeable a no more compact particles but with graphite layer separated. The images could support the hypothesis of co-intercalation mechanism.

4.3.5 FE-SEM

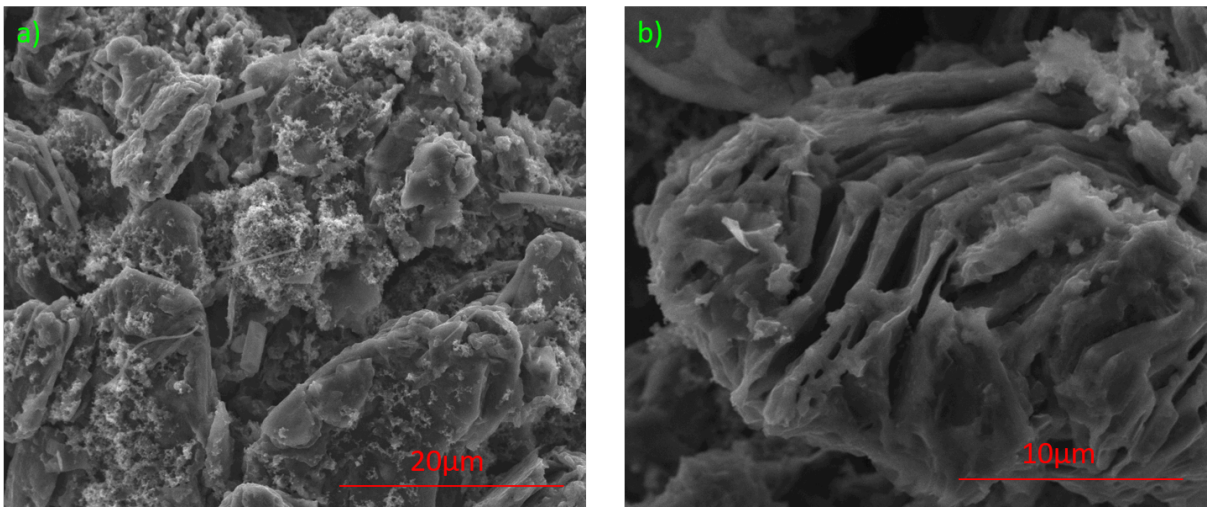

Figure 4.23: Cycled graphite electrode with KFSI at different magnification.

As suggested in literature, a change from microsize to nanosize range and from an order to a disordered structure affect the performance of the electrode. The failure of both cells with graphite (microsize range and ordered structure) as anode moves the attention towards materials with different features. Carbonaceous material with amorphous and nanosize structure will be studied in the following sections.

4.4 SuperP

FE-SEM analysis was carried out also on powders and the morphology is shown in Figure 4.24. It can be noticed that the particles are in nano-size range and that they suffer of agglomeration. In literature, the broad peaks in XRD pattern confirms that the material is not crystalline [82].

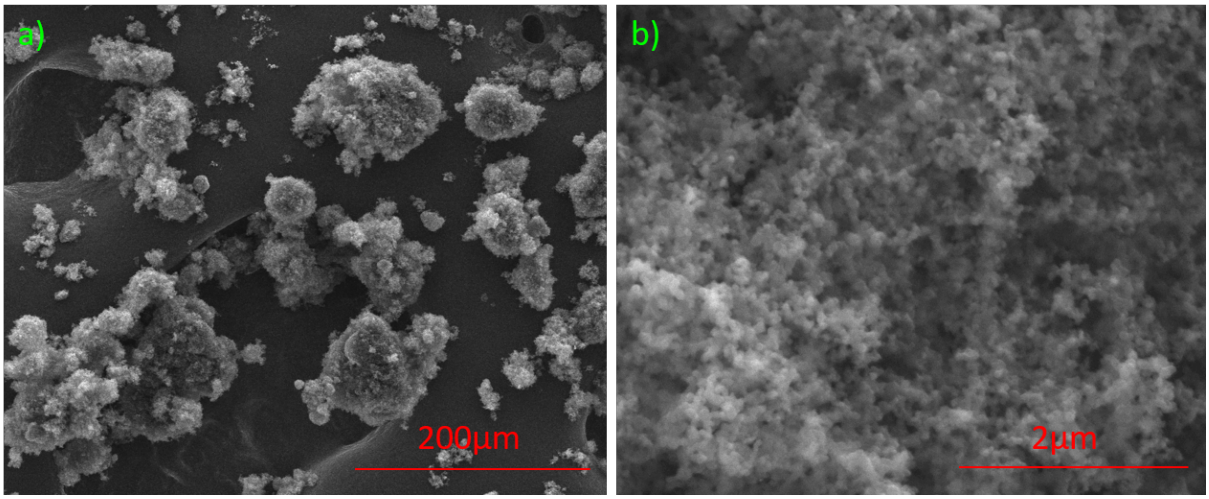

Figure 4.24: FE-SEM images of SuperP powder at different magnification.

No articles have been yet published on the topic so that results will be compared with LIB and SIB. Three replicas of coin cells were made and tested. The first one didn't recover after having been tested at 5 A/g, while the other two completed the test program with the results shown in Figure 4.25 and in Table.

4.5 SuperP-KPF_6

4.5.1 Electrochemical performance

Cell	M_a	D-cap 15	CE(%)	D-cap 100	CE(%)	D-cap 200	CE(%)
1	0.001531g	140.15	91.79	118.41	96.77	107.65	98.91
2	0.001451g	143.23	91.84	118.89	96.73	110.44	98.71

Table 4.4: Active mass and discharge capacity at 15th, 100th and 200th.

The results shows a similar behaviour of the cells tested. Electrochemical performances of this system are higher than the one obtained for graphite with the same electrolyte. In Figure 4.25 the specific capacities at different current rates are reported upon cycle number. In the first 10 cycles capacity varies from 800 mAh/g to 200 mAh/g indicating some irreversible phenomena happening in the first cycles. In fact, due to the high specific surface area and abundant defects of non-graphitic carbon, a large amount of electrolyte will be consumed during the electrochemical reaction to form excessive SEI, resulting in low initial Coulombic efficiency [51]. The poor initial CE could be due to irreversible

adsorption for potassium that would not participate in the following charge/discharge process [83]. The rate capability is good with a capacity of 46 mAh/g and a Coulombic efficiency of almost 100% which is even higher that at lower current densities. Furthermore the capacity is stable upon cycling: with a capacity retention of 84% between 15th and 100th cycle and of 76% between 15th and 200th cycle. This fact is evident also in Figure 4.28, where curves almost overlap. With regard of Coulombic efficiency in Table 4.4, it goes from 92% to 96,6% and 99% at 200th cycle. In literature there are not researches specifically for SuperP in potassium ion battery but there is something about SuperP used in LIB and SIB. The performances obtained with SuperP in LIB are around 220 mAh/g while in SIB have 122 mAh/g both at a current density of 0.1 A/g. The results achieved in this research are very close to the one in SIB. [82]. In order to understand the way in which SuperP stores potassium, literature on hard carbon has been considered, due to the lack of long range order, size and similarities in curves shape.
In this kind of materials three are the main sites to accumulate ions: defects and edges on graphene, graphene-graphene interlayer and nanopores. The profile in discharge (see Figure 4.27) can be divided in three region: a sloping region at potentials higher than 0.8 V vs. K^+/K extending over a low capacity range, a sloping region with a slower potential decay at approx. 0.8–0.3 V vs. K^+/K, and a quasi-plateau at 0.3–0.0.01 V vs. K^+/K. Concerning porous morphology, it provides many active surfaces that are exposed to the electrolyte, thus facilitating K^+ ion diffusion [84].

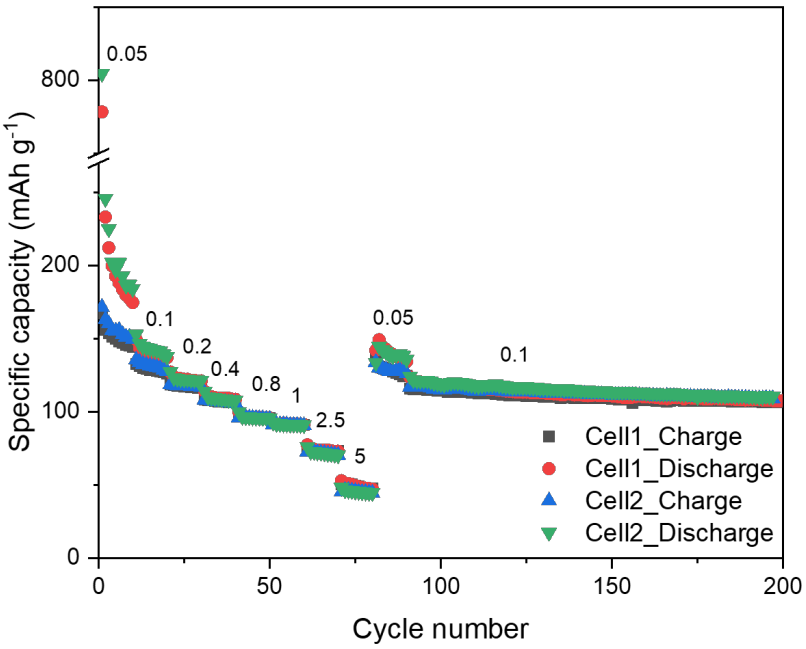

Figure 4.25: Specific capacity vs. cycle numbers, at different current densities (A/g) for SuperP with KPF_6.

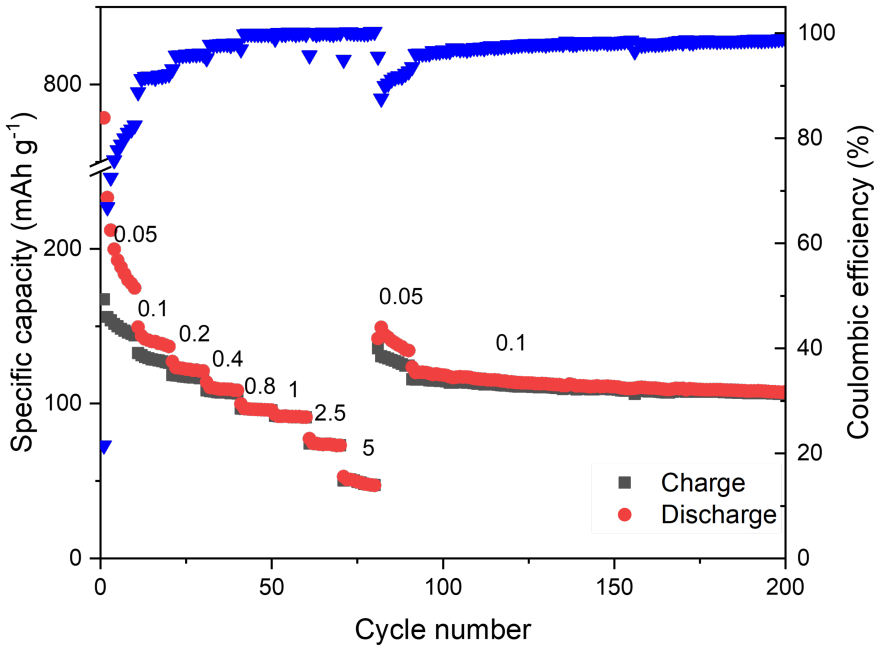

Figure 4.26: Specific capacity vs. cycle number and CE vs. cycle number for the best replica, SuperP with KPF_6.

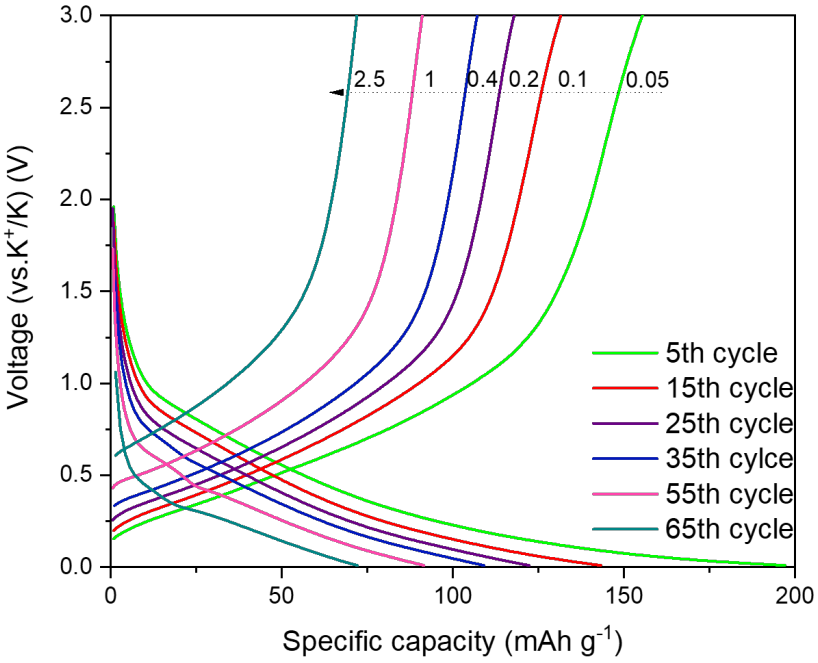

Figure 4.27: CD curves at different current rates in A/g for SuperP with KPF_6.

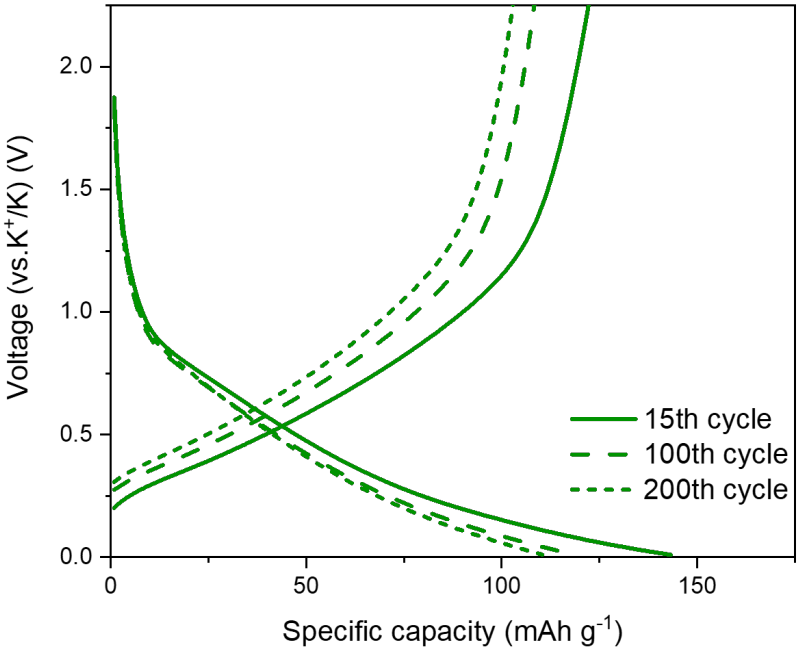

Figure 4.28: CD curves at 0.1 A/g, 15th-100th-200th cycle, SuperP with KPF_6.

4.5.2 CV

In the voltammogram (in Figure 4.29), the first cycle has specific peaks that are absent in the subsequent cycles. The curves representing 2-5th cycle almost overlap, indicating the reversibility of the reactions that take place even if some irreversible phenomena are still present. Cathodic peak at 0.6 V disappears from the second cycle and it can be attributed to the electrolyte reduction. On the reverse anodic scan, a strong peak around 0.2 V is consistent with the removal of potassium ions from the pores while broad peak centered at 0.5 V is due to K ion deintercalation from the graphene layers [85]. Therefore there are many interpretation as which region describes adsorption, intercalation and nanopores filling ([86], [85]). In this work it seems conceivable the hypothesis of adsorption-intercalation. The sloping region in charge-discharge curves (see for instance Figure 4.27) appear between 0.8-0.3 V and it would correspond to the cathodic peak at around 0.8 V. The insertion mechanism is activated at lower potential so in the 0.01-0.3 V range. The lower cutoff is 0.01 V hence there is also plating of potassium[87].

In Figure 4.32 dQdV vs. V curves have been plotted. It is interesting to notice that at higher current densities other mechanism are involved in fact there is the presence of peaks which are not evident at lower current densities and that needs further analyses. Moreover it can be observed that the peak at 0.01 V corresponds even at higher current densities while the peak at around 0.8 V moves at lower potential.Looking at CD curves in Figure 4.27, the quasi-plateau is less evident, maybe due to an higher contribution of a more capacitive nature at higher current densities, which is also reported in [88].

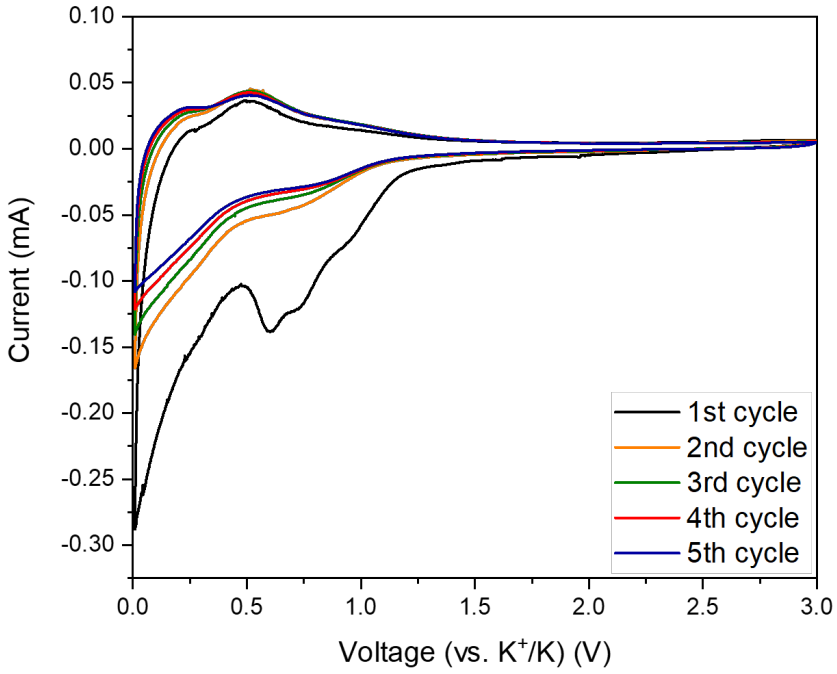

Figure 4.29: Voltammogram for SuperP with KPF_6.

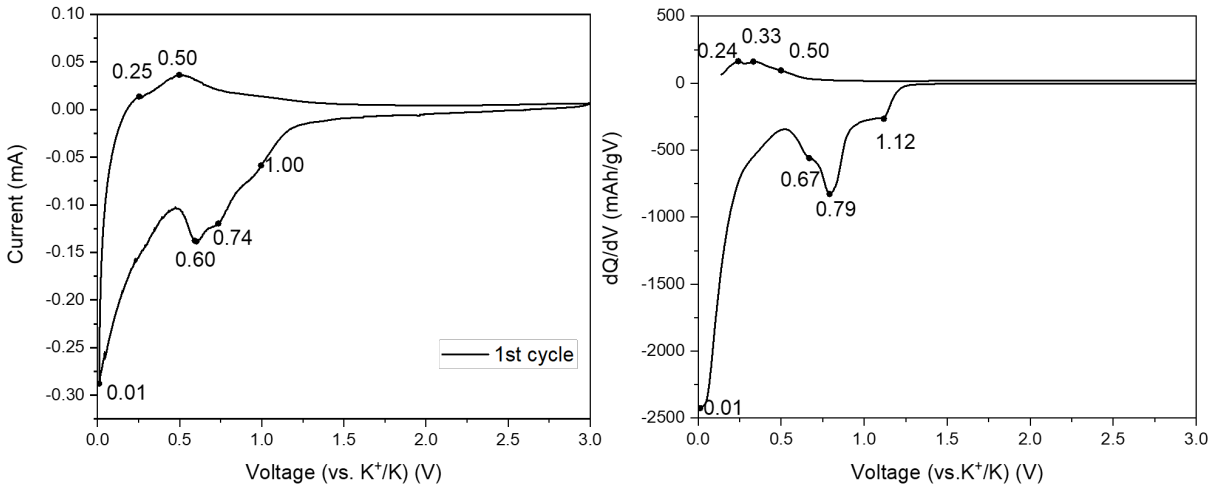

Figure 4.30: Comparison first cycle of CV and dQ/dV for SuperP with KPF_6.

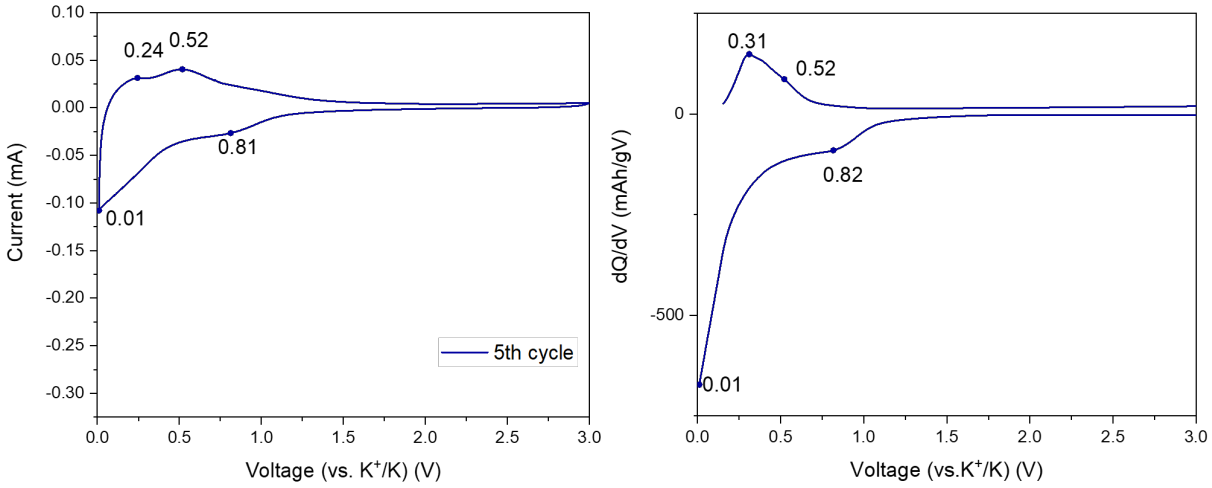

Figure 4.31: Comparison fifth cycle of CV and dQ/dV for SuperP with KPF_6.

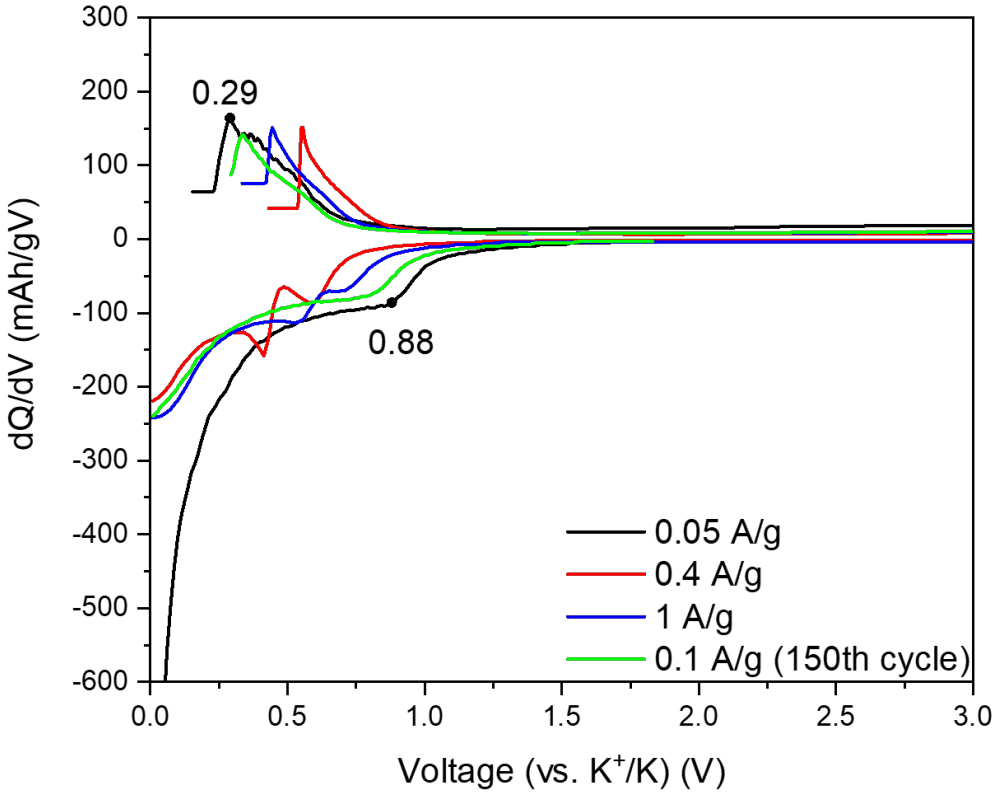

Figure 4.32: dQ/dV curves for SuperP with KPF_6 at different current densities.

4.5.3 FE-SEM

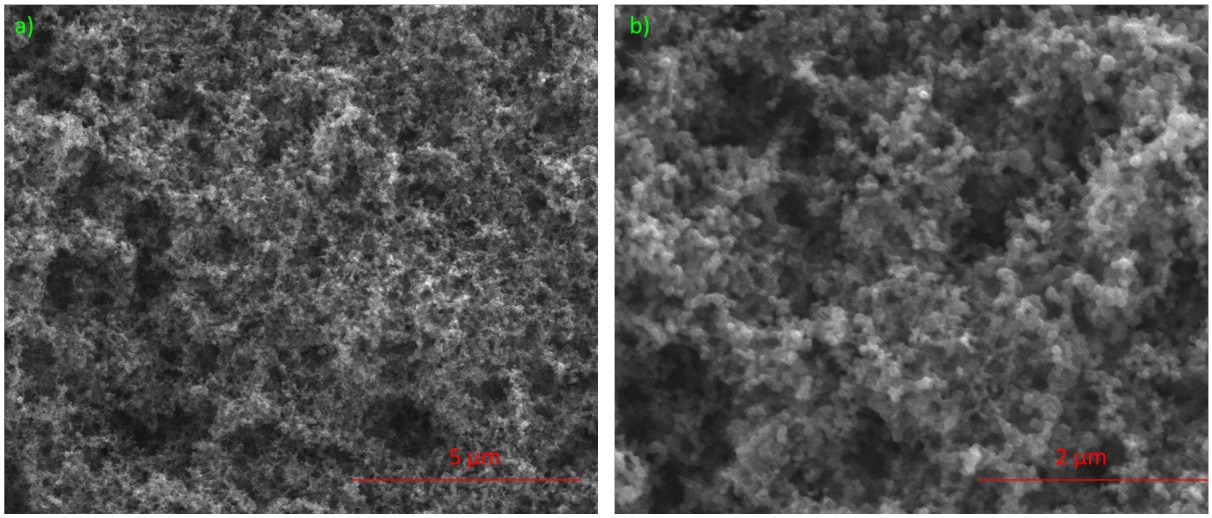

Figure 4.33: FE-SEM images of SuperP at different magnification.

The micrograph of the fresh electrode shows a material which is porous, flocculent, poorly crystalline (similar to literature findings[82]).
The two FE-SEM images proposed in Figure 4.34 were taken from the electrode cycled with the charge discharge program. It can be noticed in 4.34 a) the presence of micro cubes with very sharp edges and shiny spots. At higher magnification (see 4.34) b) a different morphology is evident: it is of micro size range and it looks crystalline. It has been supposed that it is salt penetrated in the porous structure. The SuperP after cycling has still a sphere like morphologies in nano-size range. The electrode should be analysed again with a washing step longer in order to dissolve a larger part of salt.

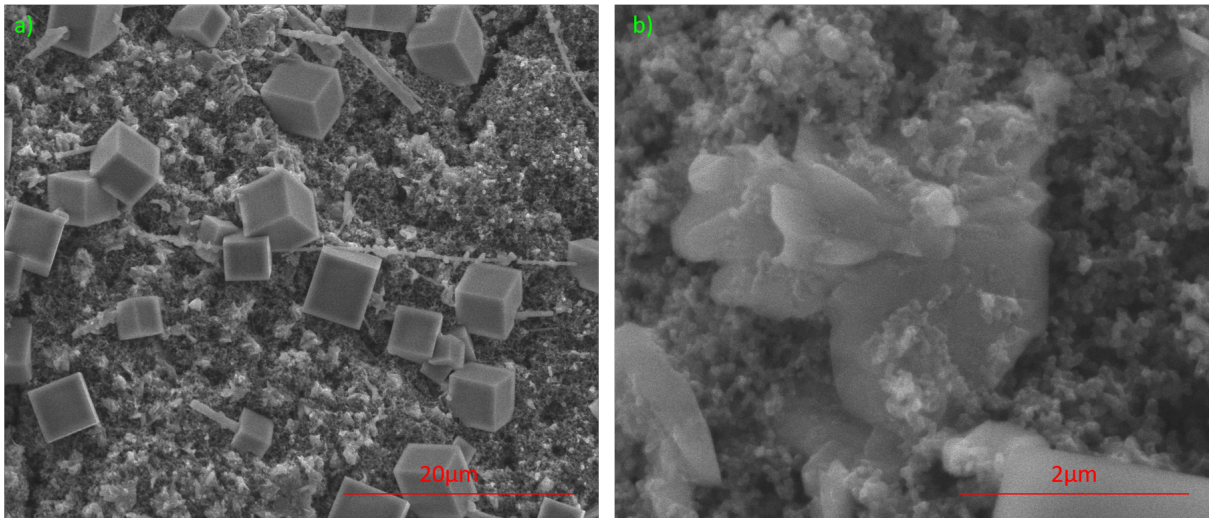

Figure 4.34: FE-SEM images of SuperP cycled in KPF_6 at different magnification.

4.5.4 Forming stage

Nyquist plot presented in Figure 4.35, shows (at sx) the spectra in the total range while the behaviour at high and medium frequencies in the graph at dx. In the low frequency region the trend between different cycles is the same with a straight line at an angle higher than 45°. In high frequencies region (indicated by the orange arrow) there is a non complete depressed semi-circle. In the fitting model it was not described because it corresponds to such a low value that the fitting software did not see it. In medium frequencies range, a depressed semicircle is attributed to charge transfer resistance and it is almost constant upon 10 cycles, the estimated value are reported in 4.5. This result is in line with electrochemical performance.

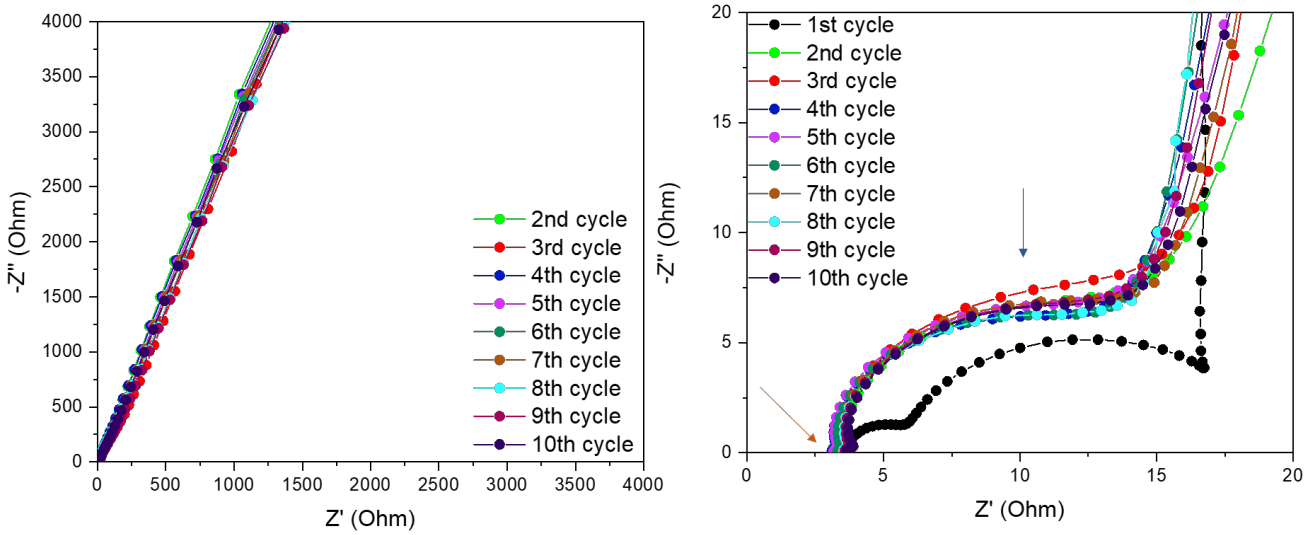

Figure 4.35: Nyquist plot for SuperP with KPF_6 salt, forming stage; at sx full spectrum, at dx high-medium frequencies.

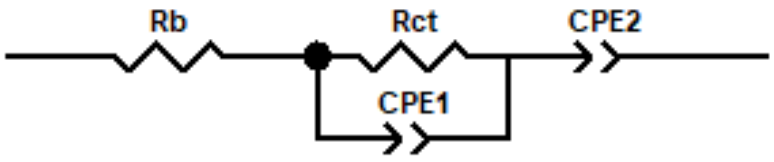

Figure 4.36: EIS model for SuperP with KPF_6.

Cycle	Rct (Ohm)	Error(%)
2	10.25	0.89
3	8.95	3.2
5	9.25	1.52
7	9.65	1.89
10	9.09	1.89

Table 4.5: Charge transfer resistance upon cycling for SuperP in KPF_6.

4.5.5 Aging

The performance at high number of cycles are depicted in Figure 4.37, the specific capacity is around 110 mAh/g, with a CE of 99%. The value is very stable upon cycling. The first 100 cycles have higher capacities but lower CE. At this regard, it can be noticed that EIS after forming and after 100 cycles shows a difference: in fact it is more evident a depressed semi-circle which increases consistently upon cycling (see Figure 4.39). This could be attributed to the formation of a SEI layer which stabilized the cycling performances. The values obtained after 200 cycles have an higher resistance, resulting in a shift of the curve. At the same time the performance after 200 cycles are not lower in the charge-discharge cycles and EIS spectra after 300 cycles follow the initial trend of an enlarged semi-circles at high frequencies and an almost constant semi-circles at medium frequencies, hence the results after 200 cycles can be due to some measurements artifacts or to a system which was not stable. The second semi-circle is usually correlated with charge transfer resistance so it can be said that after a consistent increase between forming and first 100 cycles the value is stable. It is interesting to notice that in the Nyquist plot in forming stage (see 4.35), the first semi-circle was barely evident, here it appears a bit more defined after 500 cycles. This could be due to the high specific surface which would need longer time to form stable SEI layer[89].

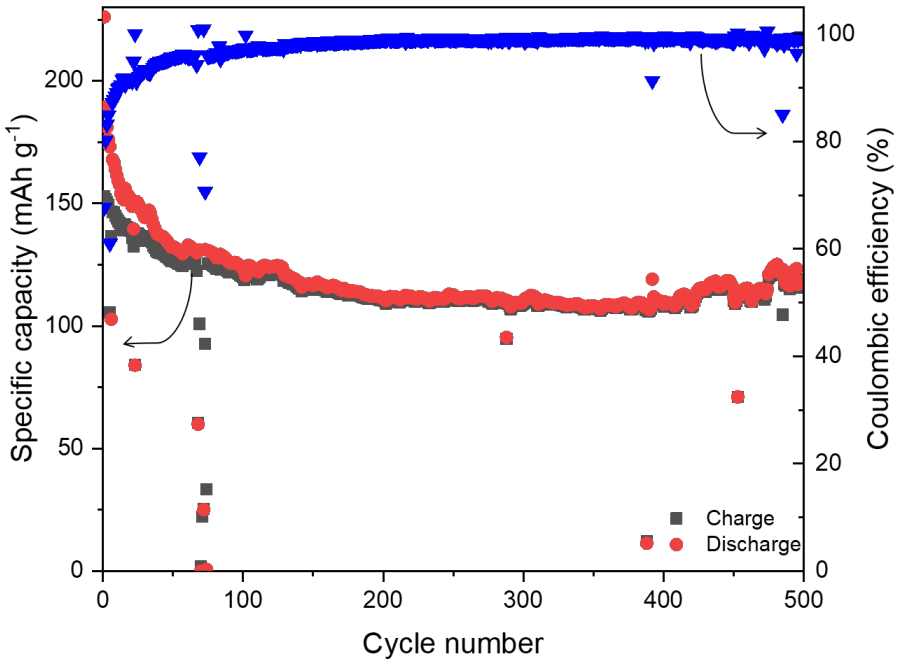

Figure 4.37: Specific capacity vs. cycle number, aging test at 0.1 A/g for SuperP with KPF_6.

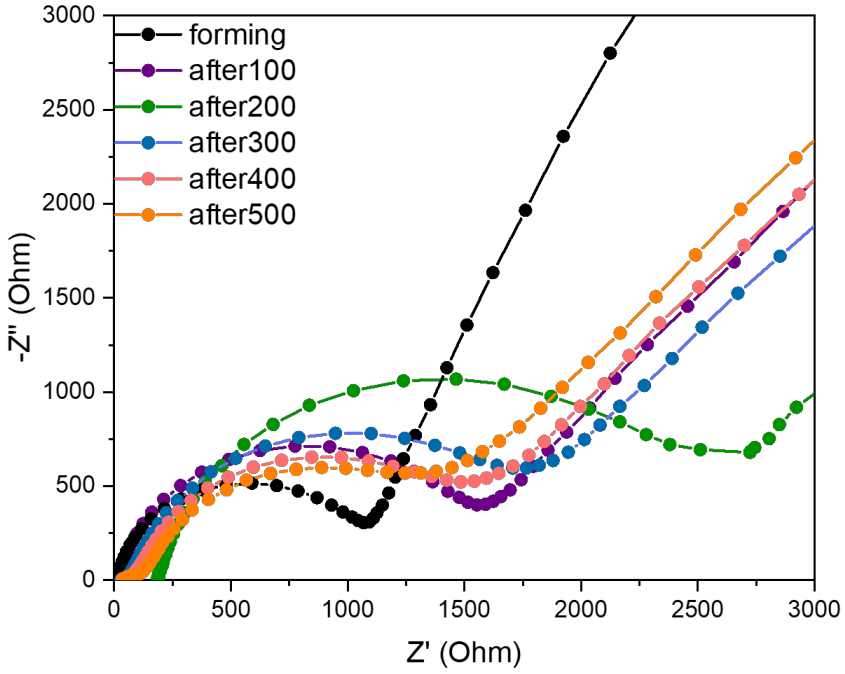

Figure 4.38: Nyquist plot recorded every 100 cycles during aging test for SuperP with KPF_6 salt.

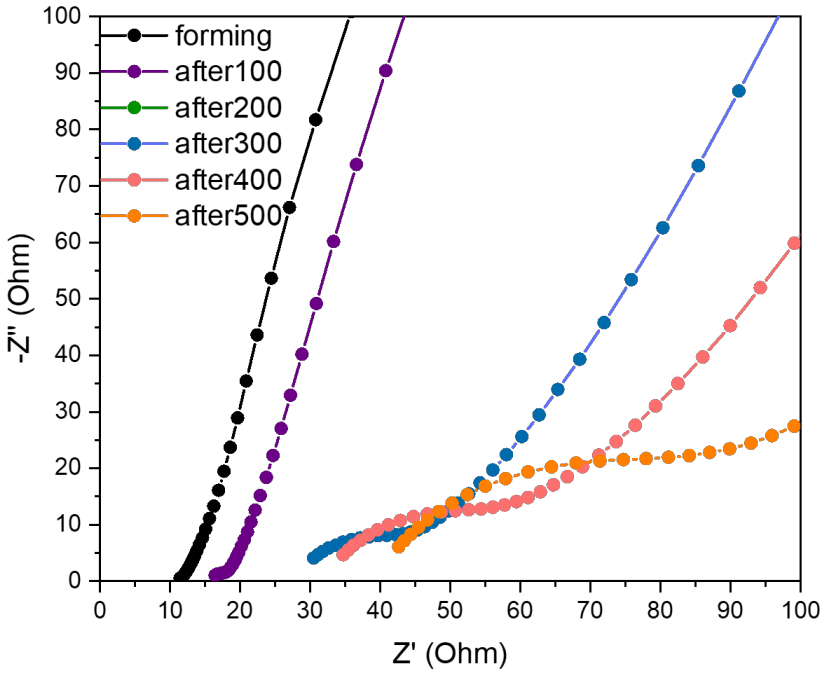

Figure 4.39: EIS spectra for SuperP with KPF_6 salt, highlighting high frequencies range.

4.6 SuperP-KFSI

4.6.1 Electrochemical performances

Cell	M_a	D-cap 15	CE(%)	D-cap 100	CE(%)	D-cap 200	CE(%)
1	0.00137g	166.51	98.89	142.35	99.4	121	152.9
2	0.00137g	191.81	98.9	149.09	287.09	168.49	102.5

Table 4.6: Active mass and discharge capacity at 15th, 100th and 200th.

The SuperP with KFSI has not a stable trend. In the first cycles the capacity increases indicating some activation in the material. It can be noticed that rate capability is quite good with a capacity of almost 50 mAh/g at 5 A/g. Concerning cycle stability, it is worse than cells tested with KPF_6 salt: the last 100 cycles in both cells show degradation process, both can be seen in Figure 4.40. The worsening is more evident in the charge branch(see Figure 4.42) while in discharge curves almost overlap.

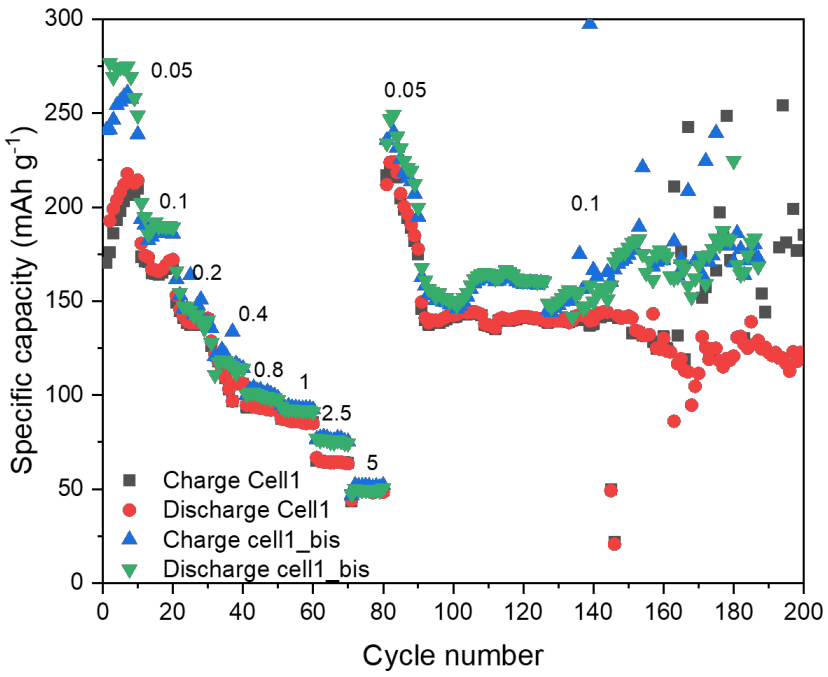

Figure 4.40: Voltage versus specific capacity at different current densities for SuperP with KFSI.

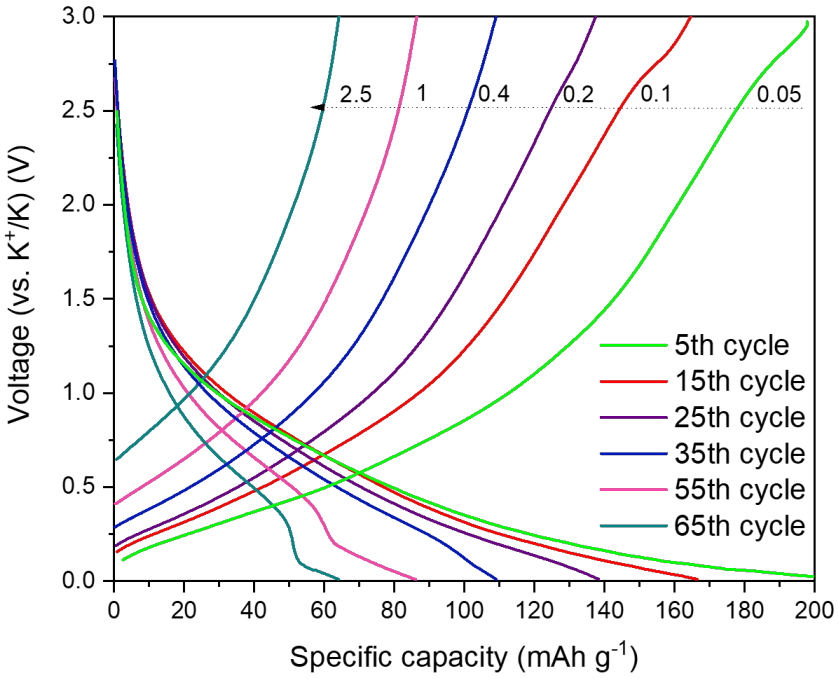

Figure 4.41: CD curves at different current rates in A/g for SuperP with KFSI.

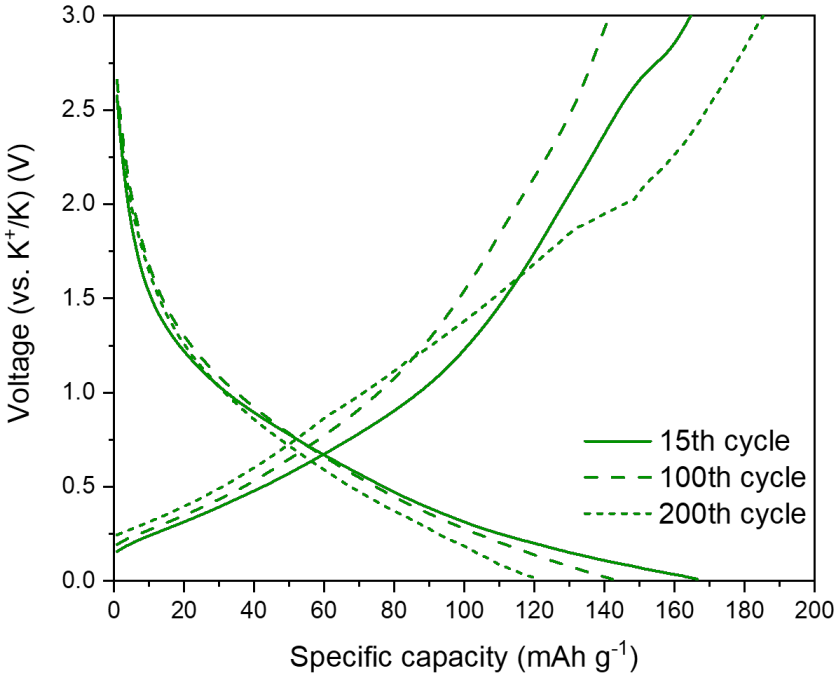

Figure 4.42: CD curves at 15-100-200th cycle at 0.1 A/g for SuperP with KFSI.

4.6.2 CV

The first cycle is characterized by a peak at 0.87 V, which disappears in the following cycles. In literature a similar cathodic peak was found for KFSI 3M in DME for graphite [51] which is attributed to SEI layer formation due to decomposition of KFSI salt. The corresponding peak in the anodic branch is at around 0.2 V which is stable showing the same value at the 5th cycle too. The behaviour in reduction shows the stable presence of three peaks at 0.95 V, 0.23 V and 0.01 V which could be due respectively to adsorption and intercalation. It is indeed true that the peaks at 0.95 V and 0.23 V are very broad which is confirmed by the CD curves in Figure 4.41, where no plateau are present but rather a sloping trend. The latter, in literature [88], indicates that intercalation of K^+ in graphitic layer contributes less to potassium storage. Furthermore, in Figure 4.41, it is interesting to see that in the slope like curves there is an abrupt change at high current densities in the lower voltage region. This latter is considered the zone in which storage is due to intercalation and nanopores filling (as mentioned for SuperP in KPF_6). In the voltammogram (see in the next paragraph Figure 4.44) there is a peak at 0.23V which at this rate does not contribute. It could be inferred that the peak describes some phenomena which is kinetically controlled.

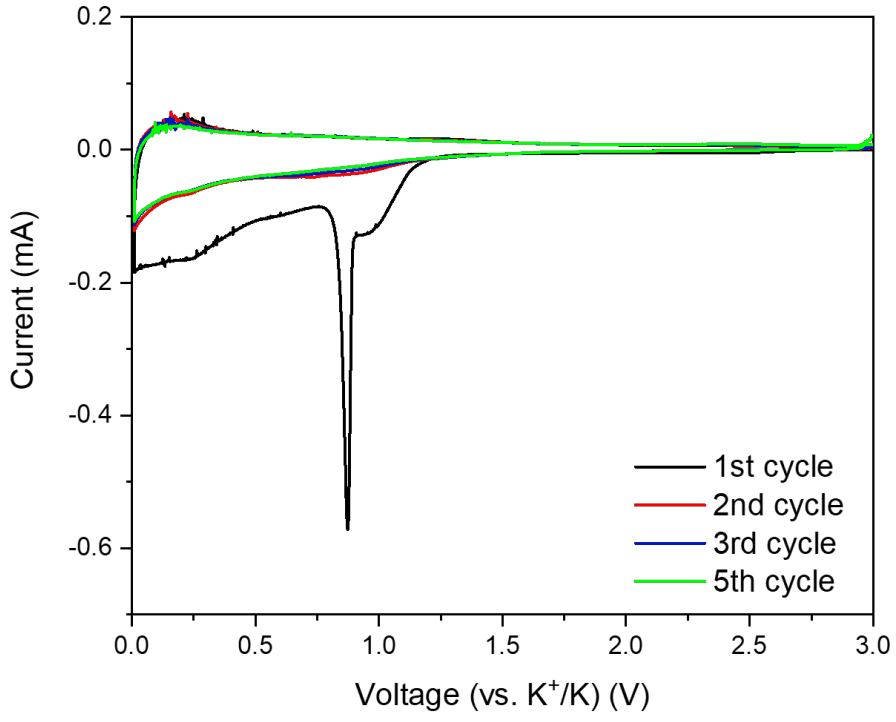

Figure 4.43: Voltammogram for SuperP with KFSI.

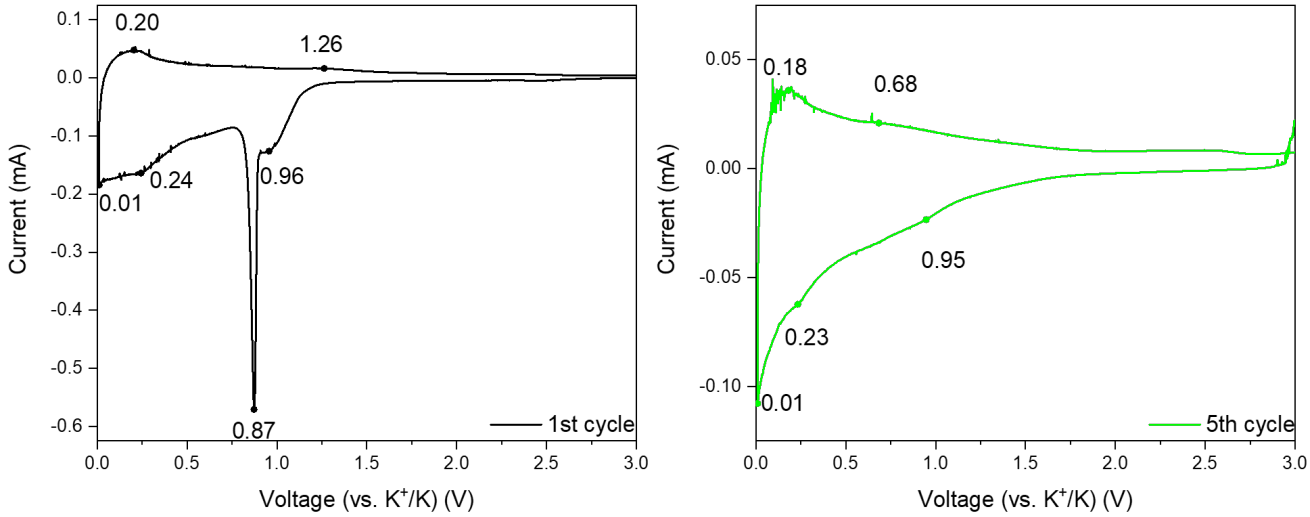

Figure 4.44: Voltammogram of cycle 1 and 5 for SuperP with KFSI and related peaks.

4.6.3 Forming stage

The behaviour in the forming stage is shown in Figure 4.45. It can be noticed that the trend is similar between different cycles. The circuit is similar to the one used in [90]. In order to highlight the behaviour in the high and medium frequencies range, the axis have been restricted and the graph in Figure 4.46 has been obtained. Three different regions can be described with two depressed semi-circles and a straight line, hence the model used is the one depicted in 4.47. The parameter R_b represents the resistance of the system as already explained in Chapter2. The parallel R_{sei} and CPE1 models the SEI formation (the region with number 1 in 4.46) while the second parallel the charge transfer resistance (semi-circle with number (2). The CPE_{diff} depicts the behaviour at low frequencies: the trend is a straight line with an angular coefficient higher than 45°, for this instead of a Warburg impedance it has been deemed that a CPE could fit better. Comparing the values in 4.7, the first resistance slightly increases as the second one while the straight line has the same angular coefficient. From these data is conceivable a formation of an interphase such as a SEI layer by the moment that there is an increase in R_{SEI}. Charge resistance varies its value from 20 to 62 Ω.

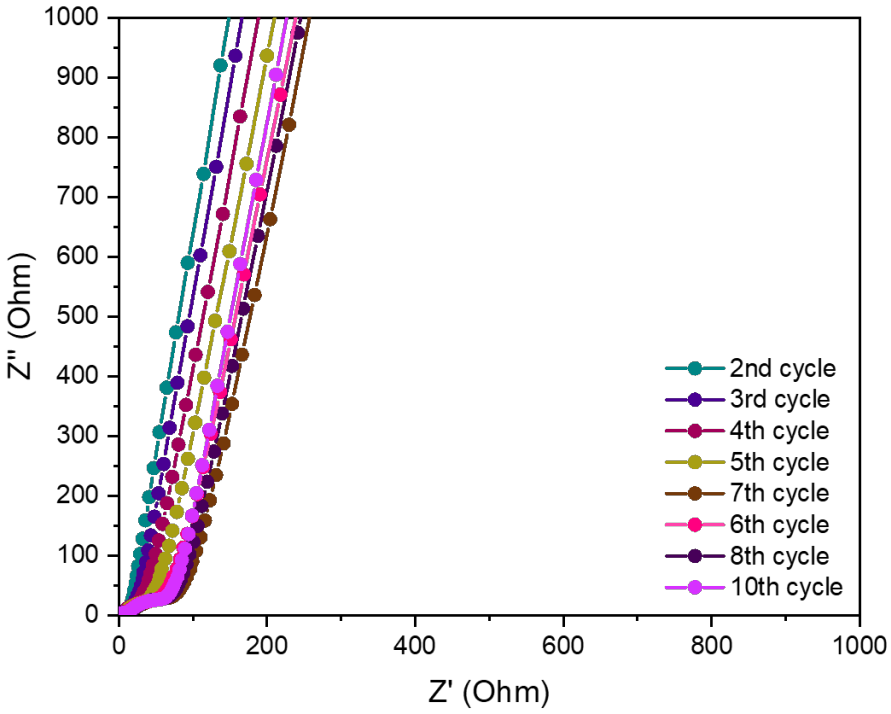

Figure 4.45: Nyquist plot for SuperP with KFSI salt, forming stage full spectrum

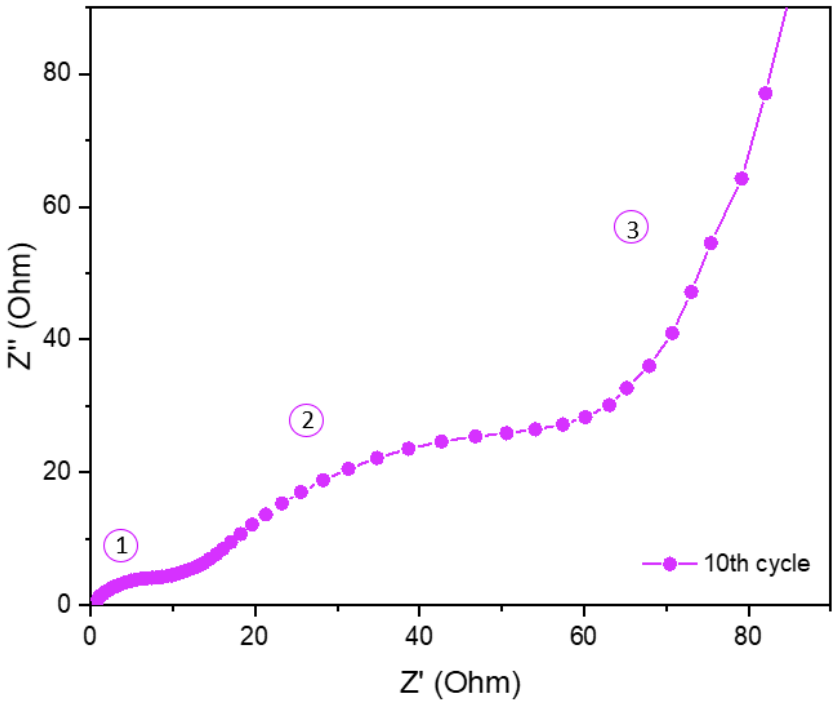

Figure 4.46: Nyquist plot for SuperP with KFSI salt at 10th cycle. Region 1 represents high frequency, region 2 medium frequency and 3 low frequency.

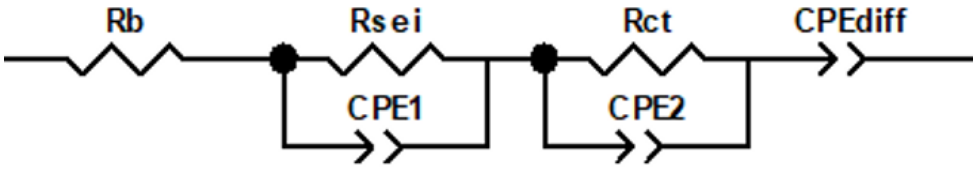

Figure 4.47: Model for fitting SuperP with KFSI.

Cycle	Rsei (Ohm)	Error(%)	Rct (Ohm)	Error(%)
2	3.68	1.53	20.23	4.09
3	3.91	1.23	28.41	3.15
5	7.06	2.85	62	3.19
8	13.46	4.05	65.71	4.1
10	10.76	3.8	61.77	4.37

Table 4.7: SEI and charge transfer resistance upon cycling for SuperP with KFSI.

4.6.4 Aging

The trend at high cycle number has not been explored completely, due to lack of time. In Figure 4.48 it is depicted the capacity over cycles for the first 200 cycles. As it happened for test 1 also in this test the performances are not stable with a CE higher than 100%, indicating degrading processes. The average specific capacity is around 140 mAh/g. In Nyquist plot in Figure 4.49 it can be noticed that there is a different trend between the two semi-circle. The one at higher frequencies decreases while the one at medium frequencies increases a lot, in particular after200 cycles. The performance between 100 and 200 cycles show a worsening with degradation phenomena. The latter is further confirmed by EIS, which in Nyquist plot shows a consistent increase in charge transfer resistance and an almost absent diffusion.

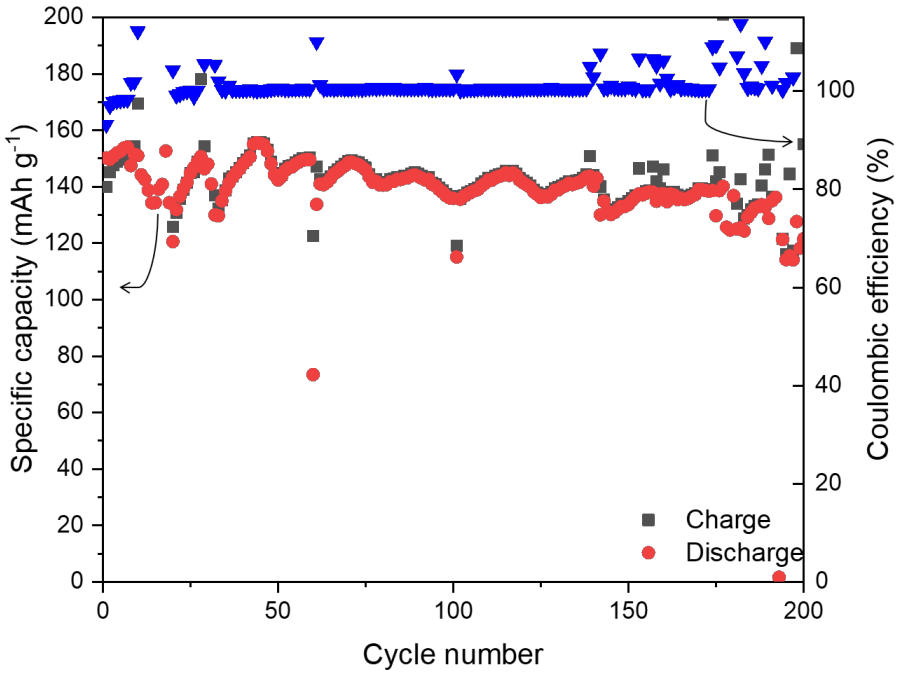

Figure 4.48: Specific capacity vs. cycle number, aging test at 0.1 A/g for SuperP with KFSI.

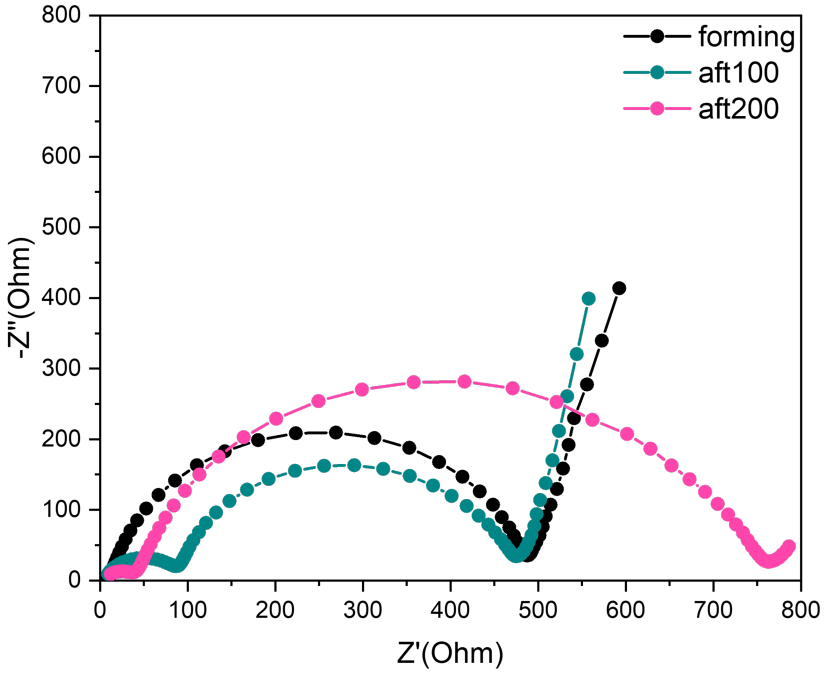

Figure 4.49: Nyquist plot recorded every 100 cycles during aging test for Super P with KFSI.

4.7 C45-KPF_6

4.7.1 Electrochemical performances

Cell	ma	D-cap 15	CE(%)	D-cap 100	CE(%)	D-cap 200	CE(%)
1	0.001633g	169.82	93.44	144.07	97.33	130.86	98.85
2	0.001453g	214.57	94.09	177.18	97.24	141.55	98.91

Table 4.8: Active mass and discharge capacity at 15th, 100th and 200th for C45 with KPF_6.

Electrochemical performances of this system are shown in Figure 4.50. The first cycle as the case for SuperP has a discharge capacity at cycle 1 equal to 684 and 981 mAh/g for cell1 and cell2 respectively with a CE of 32 and 30 %. These values were not plotted. Cell1 has lower specific capacity values except at higher current densities where a specific capacity of 85 mAh/g at 2.5 A/g and 45 mAh/g at 5 A/g are recorded. Cell2 has higher values at low current densities but a more unstable profile, in particular considering the last 100 cycles. It is interesting to notice that both systems have a better CE at higher current densities, for instance cell1 reach a 100% efficiency at 5 A/g(see Figure 4.50 while in the first cycles, for example at 15th cycle it is around 94 %. Other replicas would be useful to establish the trend. In figure 4.52 it can be noticed a good rate capability: curves are quite close indicating poor polarization effect at higher current densities. In addition, the curve at 2.5 A/g shows a limited quasi-plateau. In literature a similar behaviour describes a more capacitive nature of storage [88]. The cycle stability can be seen in Figure **??** and in Table 4.8, hence it has a capacity retention of 85% after 100 cycles and of 77% after 200 (values for cell1). In 4.53 the cell1 performance are plotted because it has a more stable trend upon cycling. The polarization is more evident in charge.

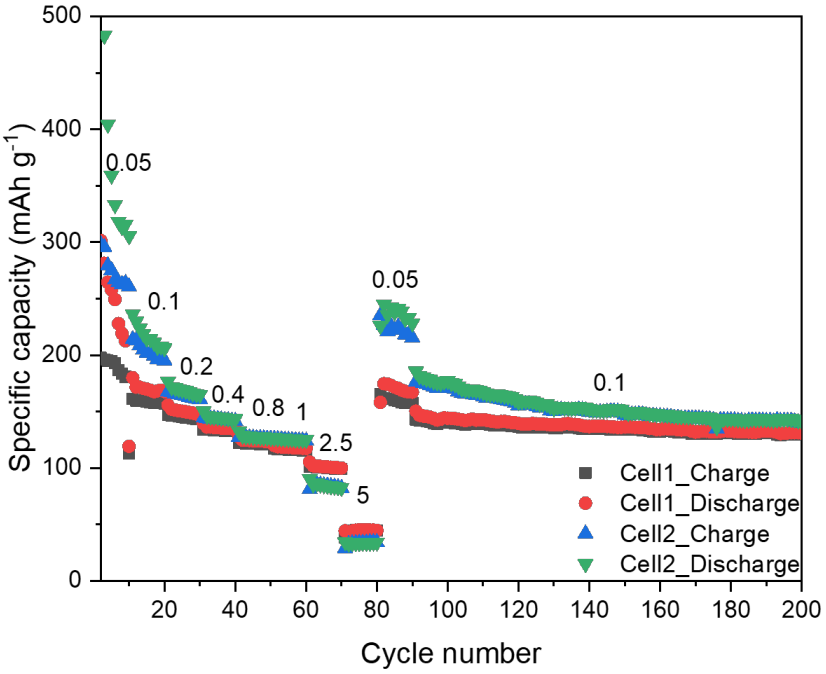

Figure 4.50: Specific capacity vs. cycle numbers, at different current densities (A/g) for C45 with KPF_6.

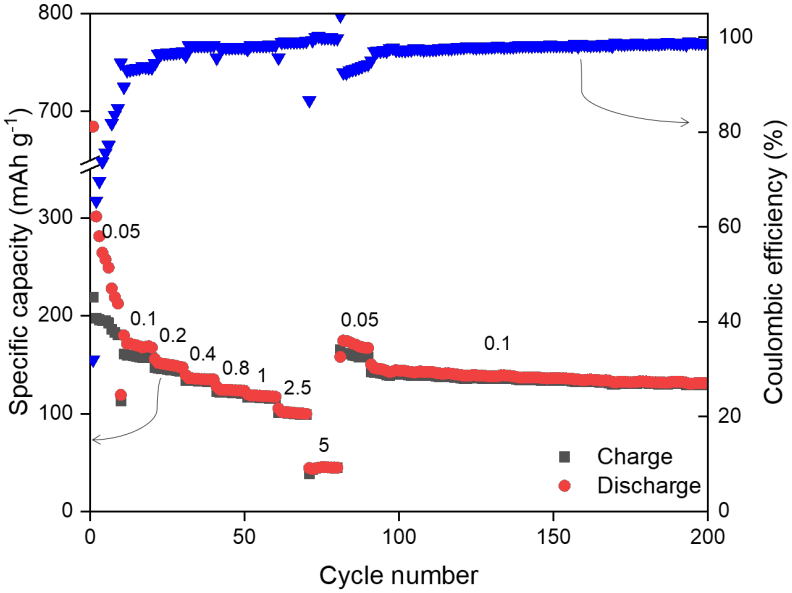

Figure 4.51: Specific capacity vs. cycle number and CE vs. cycle number for the best replica, C45 with KPF_6.

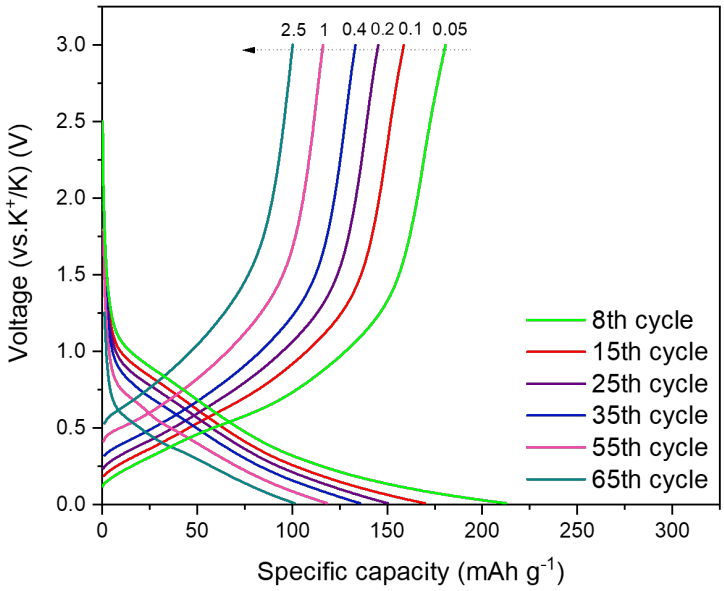

Figure 4.52: CD curves at different current rates in A/g for C45 with KPF_6.

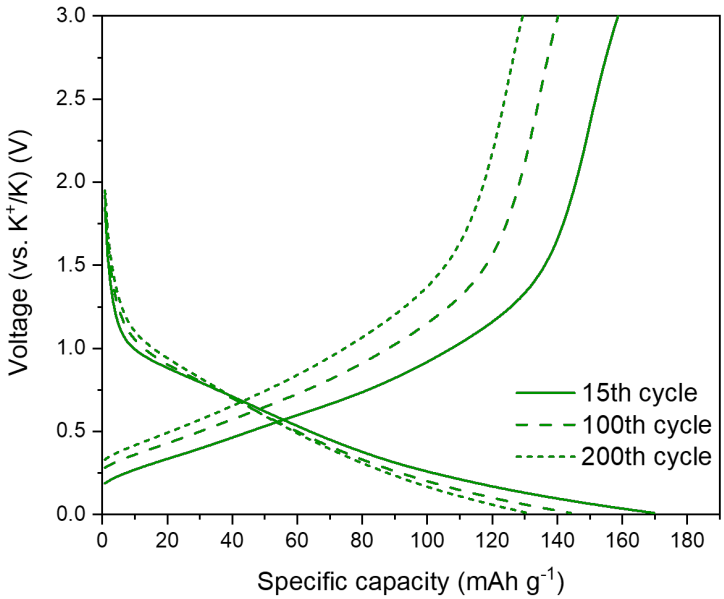

Figure 4.53: CD curves at 0.1 A/g, 15th-100th-200th cycle, C45 with KPF_6.

4.7.2 CV

The CV graph in Figure 4.54 with charge-discharge curve can help in understanding the mechanism of potassium storage by the moment that no literature has been found specifically on C45 as anode. The profile in discharge can be divided in three region: (1) a sloping region at potentials higher than 1 V vs. K^+/K extending over a low capacity range, (2) a sloping region with a slower potential decay at approx. 1–0.4V vs. K^+/K, and (3) a quasi-plateau at 0.4–0.01 V vs. K^+/K. This description is valid for the curve representing the lowest current densities (higher value of current densities have a different voltage window). The mechanism is similar to SuperP, in which the sloping trend is attributed to adsorption and the quasi-plateau to intercalation [86]. The first cycle has a large discharge capacity that is spent without being retrieved in the following cycles, hence indicating the presence of irreversible phenomena (such as SEI formation). In the cathodic branch at first cycle three peaks can be detected respectively at 0.63 V, 0.83 V and 0.01V. In the anodic part there are two main peaks at 0.23 V and 0.53 V which are stable in the first and fifth cycle. In dQ/dV vs. V curves the latter are confirmed even if at higher current densities they shift to higher potential. These peaks describe the extraction of potassium. In the following cycles the cathodic branch has two main peaks at 0.8 and at 0.01V. These values are confirmed in the differential analysis reported in Figure 4.56. Upon increasing current densities the peak at 0.9 V shifts at lower voltages while the one at 0.2-0.3 V to higher voltages as expected. It is interesting to notice that the peak at 0.01 V corresponds in all cycles.

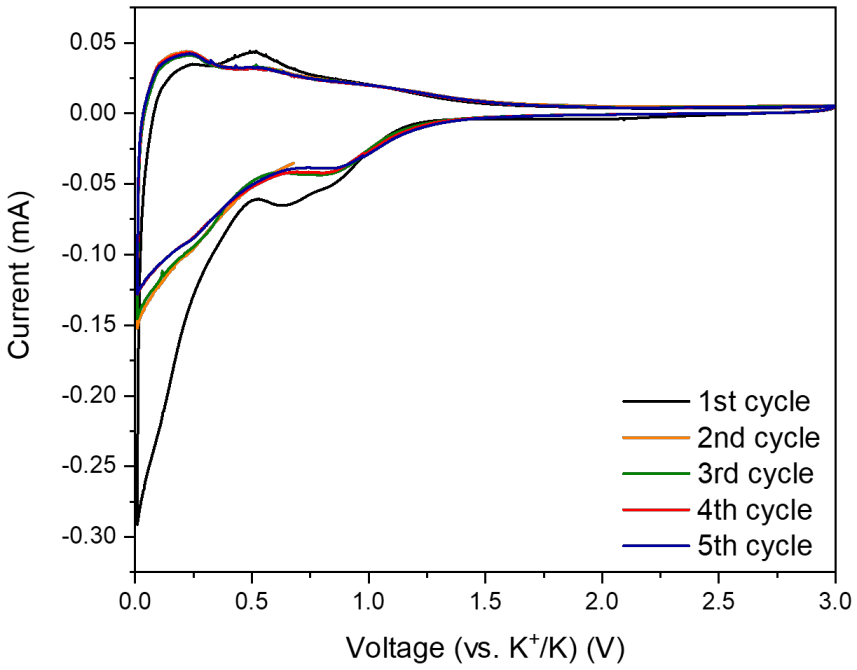

Figure 4.54: Voltammogram for C45 with KPF_6.

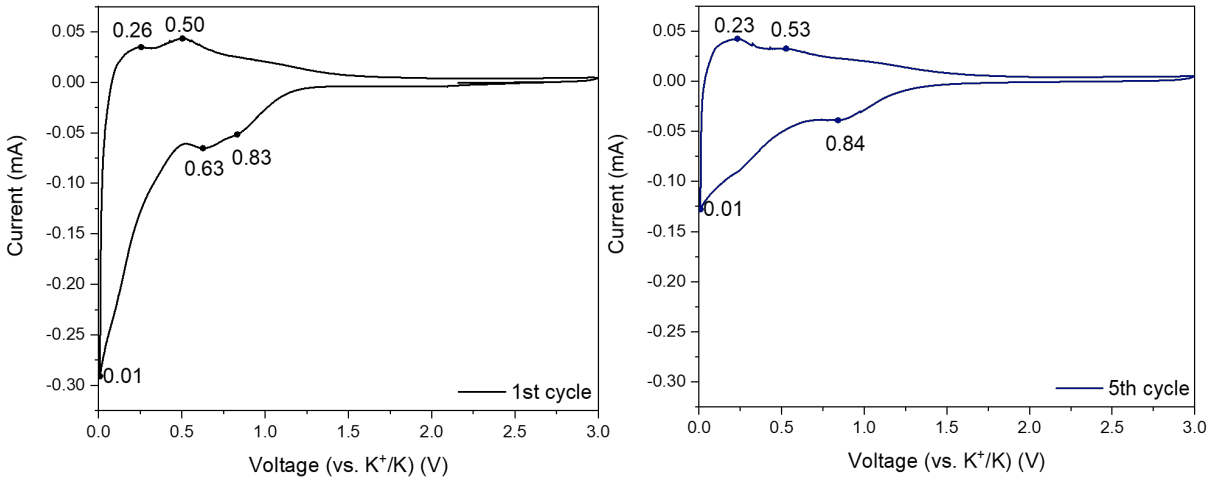

Figure 4.55: Voltammogram of cycle 1 and 5 for C45 with KPF_6 and related peaks.

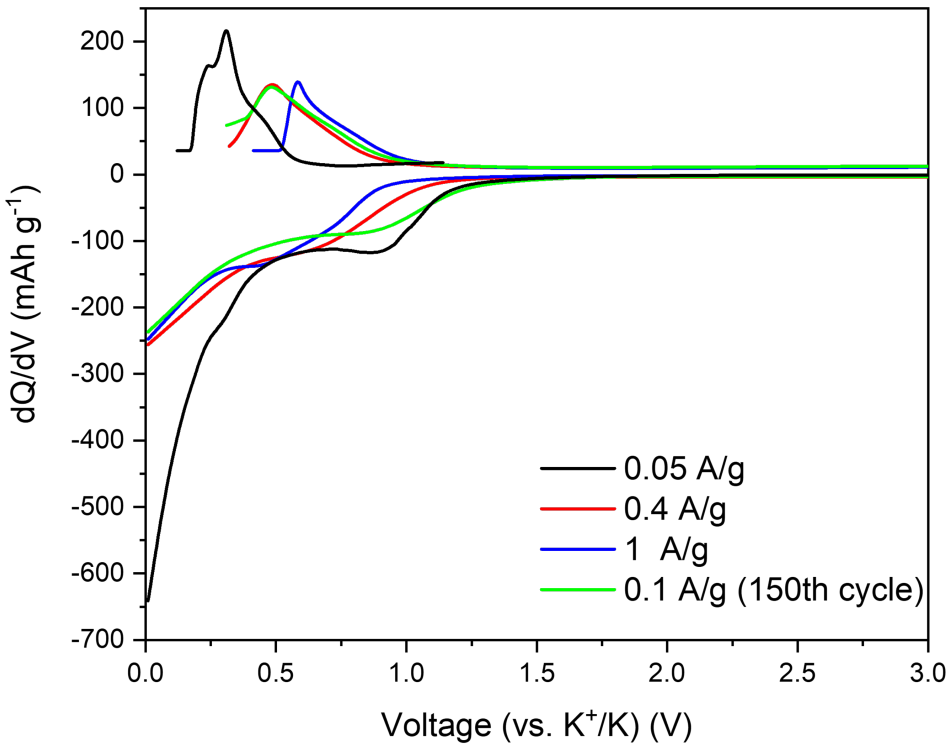

Figure 4.56: dQdV curves at different current densities for C45 with KPF_6.

4.7.3 FE-SEM

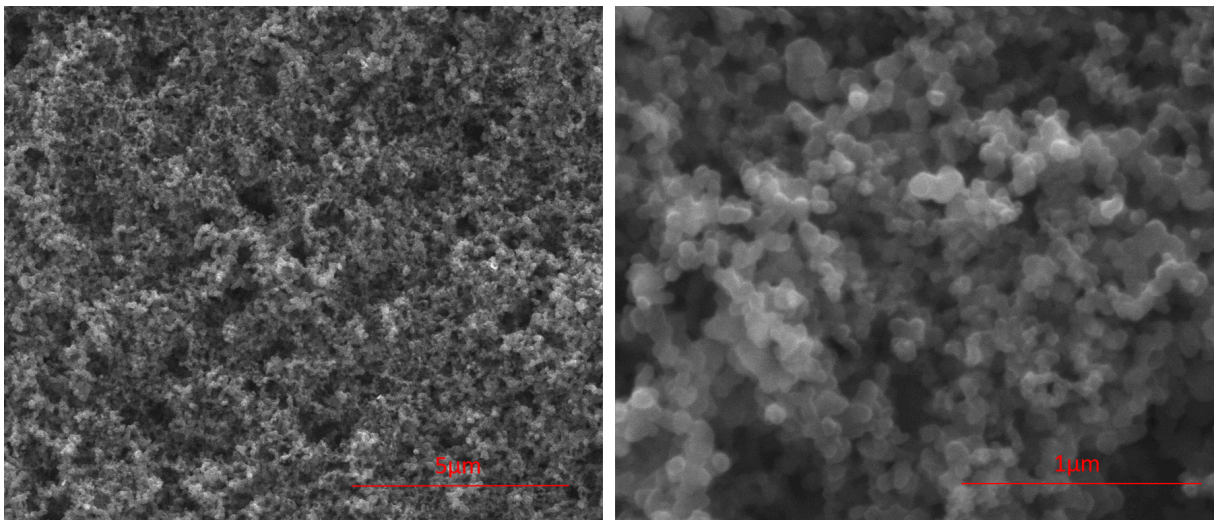

Figure 4.57: FE-SEM images at different magnification of pristine C45 electrode.

The micrographs show a material in the nano-size range. In Figure 4.57 a), the electrode is porous and very similar to SuperP.

4.7.4 Aging

This system is the last one tested and for this it did not have time to complete the 500 cycles as MoS_2 and SuperP with KPF_6. The cells have a comparable behaviour with a specific capacity higher than 160 mAh/g for the first 100 cycles. The system has an high cycle stability with a CE that gets better upon cycling. In order to explain this behaviour the Nyquist plot in Figure 4.59 can be considered. At high frequencies the formation of a semi-circle becomes more evident and correspondingly the radius of the second of semi-circle at medium frequencies decreases. This could be attributed to formation of an interface such as SEI layer that stabilizes the performance.

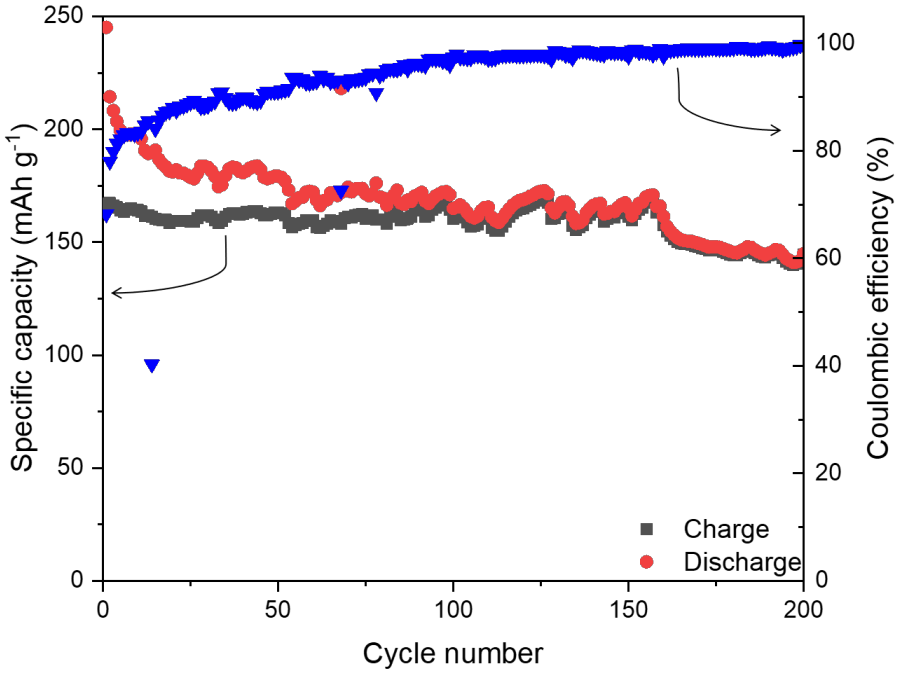

Figure 4.58: Specific capacity vs. cycle number, aging test at 0.1 A/g for C45 with KPF_6.

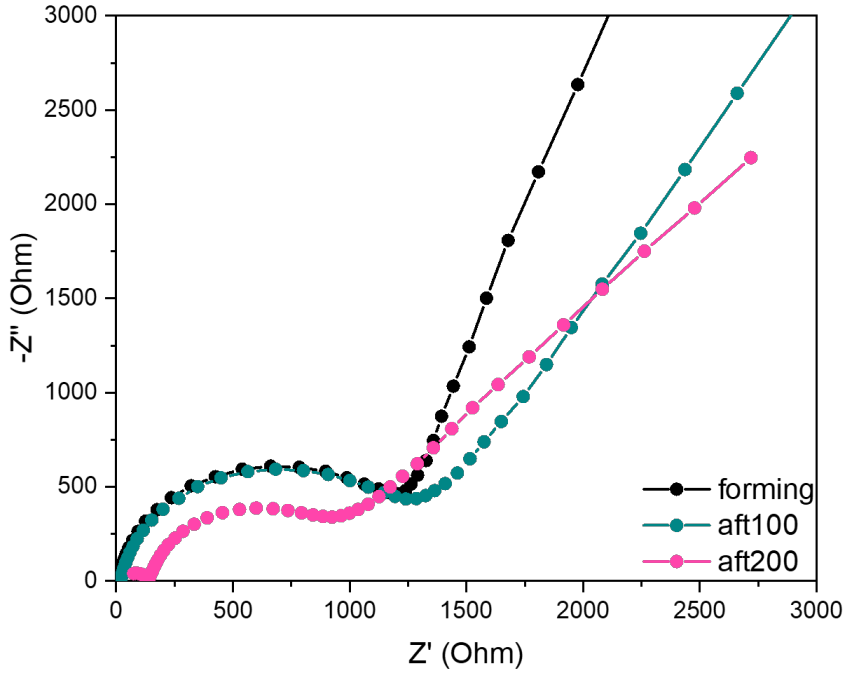

Figure 4.59: Nyquist plot recorded every 100 cycles during aging test for C45 with KPF_6.

4.8 Conclusion and future work

In this section comparison between different systems will be provided. In Figure 4.60, the electrochemical performances of the three best systems are studied and depicted.

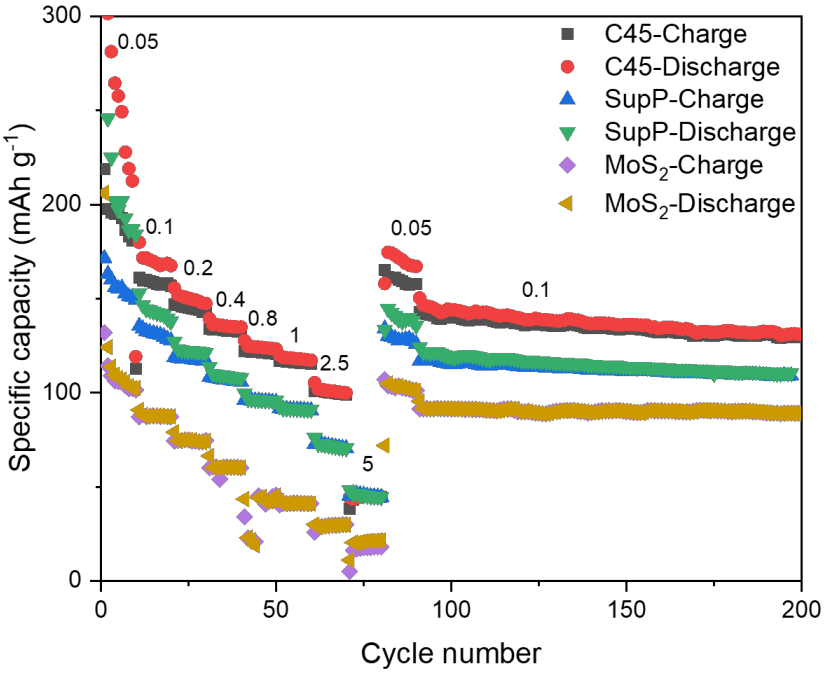

Figure 4.60: Specific capacity for coin cell at different current rates expressed in A/g, for SuperP, C45 and MOS_2 with KPF_6 in EC:DEC.

C45 shows better performance in terms of capacity, followed by SuperP. It can be noticed that the CE in the systems follow a different trend: for C45 and SuperP is higher at high current densities while in MoS_2 at low current densities. The systems act in different ways to store charge which is also evident comparing the dQ/dV vs. V curves respectively in Figure 4.7 and in Figure 4.32. In this work it is indeed demonstrated the importance of electrolyte choice and of the structure of the electrode. The first it is evident comparing the results for SuperP in KPF_6 and in KFSI which show very different behaviour in particular regarding cycle stability. The second one, it is clear comparing Graphite with C45 and SuperP. All of them belong to carbonaceous materials but the performance are completely different for amorphous carbons that are definitely better. The graphite system could be tested in a HCE electrolyte such as 3M KFSI rather than the one used in this research.

Further studies are needed for all systems. In particular, for MoS_2 it would be interesting to separate the contribution of intercalation and conversion through the choice of different cut-off voltages in order to see the relevance in cycle stability. Furthermore attempts in terms of composite, nanostructured or tuning the phase (with 2T-MoS_2 which is metallic) could be strategies to enhance performance. The mechanism in SuperP and C45 is not explained in literature as already mentioned. At this regard, a correlation

between SuperP and C45 seems to be more than justified (both are in nano-size range and classified as conductive carbon) in order to elucidate the differences. The charge discharge curve shows a similar trend with a slope like region and a quasi-plateau. The C45 material has better performances. In order to understand the causes of the differences between these two carbanaceous materials the size range therefore the pore size is taken into account. In hard carbon a lot of research focuses on the role of porosity on performances. In this context no informations are available. At the same time, these two materials have a different size range (affecting pores size). It is not easy to notice it from micrographs but in literature [91] it is found that SuperP present uniform particle sizes within the range of 50–100 nm and suffer a little agglomeration while C45 particles are in the range of 100–200 nm, so slightly larger. It is known that porosity depends on particle size, hence this fact could be the cause for their slightly different performances. At the same time it would be interesting to attribute the cathodic peak at around 0.8 V found either in SuperP with KPF_6 and in C45 with KPF_6. It is deemed to describe the mechanism of potassium storage by the moment that it is stable upon cycling.

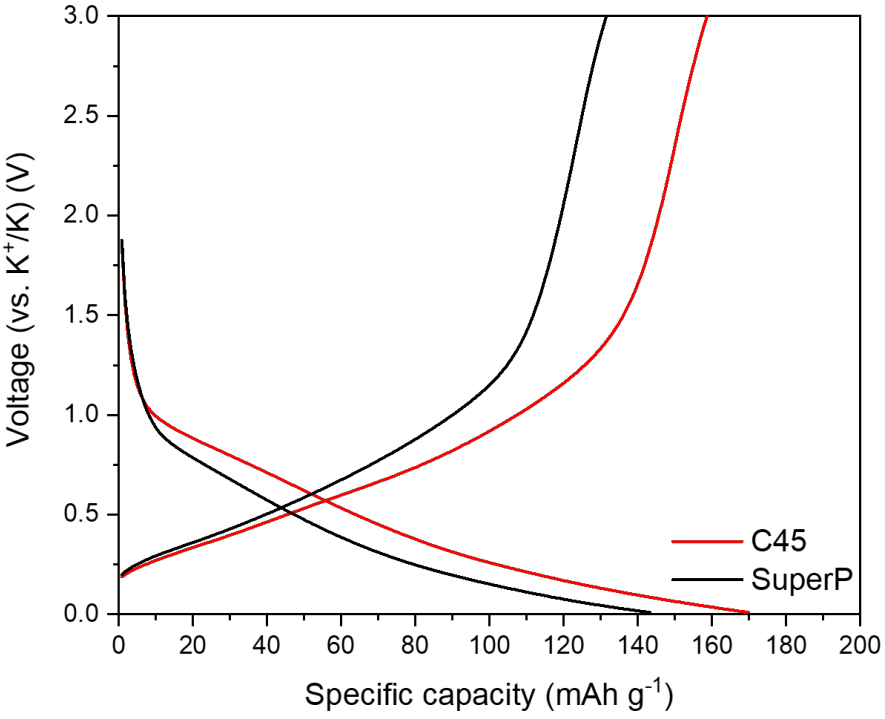

Figure 4.61: CD curves for SuperP and C45 at 0.1 A/g.

It is worth noting that rich active defect sites and large specific areas could induce an extra capacitive contribution due to the intercalation/extraction or adsorption/desorption of potassium ions that occurs at the surface or near-surface defects and nano-voids of carbon nanomaterials. Furthermore, the reaction kinetics of the potassium storage at the

surface or near-surface is faster than that of intercalation for its shortened ion and electron transportation pathway, thereby resulting in enhanced rate capability of PIBs [83]. In addition, nanoscale (hence high specific surface areas) adds a capacitive mechanism that results in an extra capacitive contribution, including pseudocapacitance and double layer.

In this research it has been confirmed the importance of morphology: in fact three carbonaceous materials have different behaviours both in performances and in mechanism to store potassium ion.
The first cycle which is attributed to the SEI layer formation is different between the different systems. In particular there is a correlation between surface area and CE in the first cycle, more surface area is responsible of lower Coulombic efficiency (see 1st cycle CE of Graphite and SuperP). Another conclusion is about the importance of electrolyte which is responsible of the stability of the system (i.e. SupP in KPF_6 and in KFSI) and performances. Aging test reveal an instability of MoS_2 which is attributed to electrolyte degradation and an unsatisfactory mechanical cohesion of the electrode. SuperP and C45 on the other hand has an extremely stable profile with an high specific capacity. C45 has two main advantages over SuperP: the solvent used is water that compared to NMP which is toxic, highly expensive and flammable while water is extremely eco-friendly. Furthermore, a water based system enhance the developing of a close-loop industrial supply chain, in which the batteries are recycled with minimal external toxic solvent through the whole system [92].

In this research, compelling results have been obtained which would justify further investigations in order to optimize the performances.

Appendix

Capacity
This parameter can be calculated at the end of discharge-charge process. The specific capacity is the capacity divided by active material mass.
Coulombic efficiency
Coulombic efficiency is the ratio between the charge extracted (C_d from the battery over the charge injected (C_i). It can be calculated dividing the specific charge capacity over the specific discharge capacity. It is an indicator of how much charge can be retrieved and used effectively in a battery: the inefficiency is related to irreversible processes, therefore it is expected a low Coulombic efficiency in the first cycles for many irreversible process (i.e. SEI formation) and then a stable value around 98% if the battery works well.
Cut-off voltage
Voltage which expresses the limit to end discharge.
Cycling stability
It is defined by the number of charging- or discharging cycles until its capacity is reduced to a certain amount of its nominal capacity (typically 50% to 80%). In this research it was compared the discharge capacity at cycle 15th with the discharge capacity of cycle 100th and 200th.
OCV
Potential difference between the electrodes of a battery or cell, measured at the terminals in a no-load condition

References

[1] (2021), [Online]. Available: https://www.climate.gov/. (accessed: 28/04/2021).

[2] (2021), [Online]. Available: https://gml.noaa.gov/ccgg/carbontracker/CT2019B_doc.php. (accessed: 28/04/2021).

[3] U. K. Carma, "Revisited: An updated database of carbon dioxide emissions from power plants worldwide. center for global development working paper 304.," 2012.

[4] (2021), [Online]. Available: https://fridaysforfuture.org/what-we-do/strike-statistics/. (accessed: 28/04/2021).

[5] (2021). "Statistical review of world energy," [Online]. Available: https://www.bp.com/en/global/corporate/energy-economics/statistical-review-of-world-energy.html. (accessed: 28/04/2021).

[6] (2021), [Online]. Available: https://news.energysage.com/behind-the-meter-overview//. (28/04/2021).

[7] I. S. Bayram and T. S. Ustun, "A survey on behind the meter energy management systems in smart grid," *Renewable Sustainable Energy Rev.*, vol. 72, pp. 1208–1232, 2017.

[8] F. Jan, S. Peter, K. Kai-Philipp, L. Jochen, H. David, W. Oliver, G. Angenendt, M. Robinius, S. Detlef, and S. Dirk Uwe, "The development of stationary battery storage systems in germany – a market review," *J. Energy Storage*, vol. 29, p. 101 153, 2020, ISSN: 2352-152X.

[9] (2021), [Online]. Available: https://www.cpuc.ca.gov/sgip/. (accessed: 28/04/2021).

[10] B.-K. Jo, S. Jung, and G. Jang, "Feasibility analysis of behind-the-meter energy storage system according to public policy on an electricity charge discount program," *Sustainability*, vol. 11, no. 1, 2019.

[11] (), [Online]. Available: https://www.iea.org/reports/sdg7-data-and-projections/access-to-electricity.

[12] R. Amirante, E. Cassone, E. Distaso, and P. Tamburrano, "Overview on recent developments in energy storage: Mechanical, electrochemical and hydrogen technologies," *Energy Convers. Manage.*, vol. 132, pp. 372–387, 2017, ISSN: 0196-8904.

[13] B. Pinnangudi, M. Kuykendal, and S. Bhadra, "4 - smart grid energy storage," in *The Power Grid*, B. W. D'Andrade, Ed., Academic Press, 2017, pp. 93–135.

[14] R. Brodd, "Nickel-based battery systems," in. Jan. 2013, pp. 423–443, ISBN: 978-1-4614-5790-9.

[15] G. Tomazic and M. Skyllas-Kazacos, "Chapter 17 - redox flow batteries," in *Electrochemical Energy Storage for Renewable Sources and Grid Balancing*, P. T. Moseley and J. Garche, Eds., Amsterdam: Elsevier, 2015, pp. 309–336, ISBN: 978-0-444-62616-5.

[16] R. Rajagopalan, Y. Tang, X. Ji, C. Jia, and H. Wang, "Advancements and challenges in potassium ion batteries: A comprehensive review," eng, *Adv. Funct. Mater.*, vol. 30, no. 12, 1 909 486–n/a, 2020, ISSN: 1616-301X.

[17] Z. Wenli, Y. Jian, W. Wenxi, B. Zahra, and N. A. Husam, "Status of rechargeable potassium batteries," *Nano Energy*, vol. 83, p. 105 792, 2021.

[18] J. Zhao, X. Zou, Y. Zhu, Y. Xu, and C. Wang, "Electrochemical intercalation of potassium into graphite," *Adv. Funct. Mater.*, vol. 26, no. 44, pp. 8103–8110, 2016.

[19] W. Zhang, J. Mao, S. Li, Z. Chen, and Z. Guo, "Phosphorus-based alloy materials for advanced potassium-ion battery anode," *J. Am. Chem. Soc.*, vol. 139, no. 9, pp. 3316–3319, 2017.

[20] M. Meshksar, F. Afshariani, and M. R. Rahimpour, "Phosphorous-based materials for k-ion batteries," in *Potassium-Ion Batteries*. John Wiley Sons, Ltd, 2020, ch. 1, pp. 1–18.

[21] T. B. Reddy, *Linden's Handbook of Batteries*. McGraw-Hill Education, 2011.

[22] R. Borah, F. Hughson, J. Johnston, and T. Nann, "On battery materials and methods," *Mater. Today Adv.*, vol. 6, p. 100 046, 2020, ISSN: 2590-0498.

[23] P. Hundekar, S. Basu, X. Fan, L. Li, A. Yoshimura, T. Gupta, V. Sarbada, A. Lakhnot, R. Jain, S. Narayanan, Y. Shi, C. Wang, and N. Koratkar, "In situ healing of dendrites in a potassium metal battery," *Proceedings of the National Academy of Sciences*, vol. 117, no. 11, pp. 5588–5594, 2020.

[24] W. Yang, J. Zhou, S. Wang, W. Zhang, Z. Wang, F. Lv, K. Wang, Q. Sun, and S. Guo, "Freestanding film made by necklace-like n-doped hollow carbon with hierarchical pores for high-performance potassium-ion storage," *Energy Environ. Sci.*, vol. 12, pp. 1605–1612, 5 2019.

[25] Z. Jian, W. Luo, and X. Ji, "Carbon electrodes for k-ion batteries," *JACS*, vol. 137, no. 36, pp. 11 566–11 569, 2015.

[26] W. Luo, J. Wan, B. Ozdemir, W. Bao, Y. Chen, J. Dai, H. Lin, Y. Xu, F. Gu, V. Barone, and L. Hu, "Potassium ion batteries with graphitic materials," *Nano letters*, vol. 15, no. 11, pp. 7671–7677, 2015, ISSN: 1530-6984.

[27] Z. Wang, S. M. Selbach, and T. Grande, "Van der waals density functional study of the energetics of alkali metal intercalation in graphite," *RSC Adv.*, vol. 4, pp. 4069–4079, 8 2014.

[28] Z. Wang, A. P. Ratvik, T. Grande, and S. M. Selbach, "Diffusion of alkali metals in the first stage graphite intercalation compounds by vdw-dft calculations," *RSC Adv.*, vol. 5, pp. 15 985–15 992, 21 2015.

[29] Z. Xu, X. Lv, J. Chen, L. Jiang, Y. Lai, and J. Li, "Dispersion-corrected dft investigation on defect chemistry and potassium migration in potassium-graphite intercalation compounds for potassium ion batteries anode materials," *Carbon*, vol. 107, pp. 885–894, 2016, ISSN: 0008-6223.

[30] S. Komaba, T. Hasegawa, M. Dahbi, and K. Kubota, "Potassium intercalation into graphite to realize high-voltage/high-power potassium-ion batteries and potassium-ion capacitors," *Electrochem. commun.*, vol. 60, pp. 172–175, 2015, ISSN: 1388-2481.

[31] Z. Tai, Q. Zhang, Y. Liu, H. Liu, and S. Dou, "Activated carbon from the graphite with increased rate capability for the potassium ion battery," *Carbon*, vol. 123, Jul. 2017.

[32] Y. An, H. Fei, G. Zeng, L. Ci, B. Xi, S. Xiong, and J. Feng, "Commercial expanded graphite as a low-cost, long-cycling life anode for potassium-ion batteries with conventional carbonate electrolyte," *J. Power Sources*, vol. 378, pp. 66–72, Feb. 2018.

[33] Y. Wang, Z. Wang, Y. Chen, H. Zhang, M. Yousaf, H. Wu, M. Zou, A. Cao, and R. P. S. Han, "Hyperporous sponge interconnected by hierarchical carbon nanotubes as a high-performance potassium-ion battery anode," *Adv. Mater.*, vol. 30, no. 32, p. 1 802 074, 2018.

[34] X. Min, J. Xiao, M. Fang, W. A. Wang, Y. Zhao, Y. Liu, A. M. Abdelkader, K. Xi, R. V. Kumar, and Z. Huang, "Potassium-ion batteries: Outlook on present and future technologies," *Energy Environ. Sci.*, vol. 14, pp. 2186–2243, 4 2021.

[35] D. A. Stevens and J. R. Dahn, "High capacity anode materials for rechargeable sodium-ion batteries," *J. Electrochem. Soc.*, vol. 147, no. 4, p. 1271, 2000.

[36] S.-S. Fan, H.-P. Liu, Q. Liu, C.-S. Ma, and T.-F. Yi, "Comprehensive insights and perspectives into the recent progress of electrode materials for non-aqueous k-ion battery," *J. Materiomics*, vol. 6, no. 2, pp. 431–454, 2020, ISSN: 2352-8478.

[37] S.-M. Xu, Y.-C. Ding, X. Liu, Q. Zhang, K.-X. Wang, and J.-S. Chen, "Boosting potassium storage capacity based on stress-induced size-dependent solid-solution behavior," *Adv. Energy Mater.*, vol. 8, no. 32, p. 1 802 175, 2018.

[38] B. Chen, D. Chao, E. Liu, M. Jaroniec, N. Zhao, and S.-Z. Qiao, "Transition metal dichalcogenides for alkali metal ion batteries: Engineering strategies at the atomic level," *Energy Environ. Sci.*, vol. 13, pp. 1096–1131, 4 2020.

[39] A. P. Nayak, S. Bhattacharyya, J. Zhu, J. Liu, X. Wu, T. Pandey, C. Jin, A. K. Singh, D. Akinwande, and J.-F. Lin, "Pressure-induced semiconducting to metallic transition in multilayered molybdenum disulphide," *Nat. commun.*, vol. 5, no. 1, pp. 3731–3731, 2014, ISSN: 2041-1723.

[40] X. Ren, Q. Zhao, W. D. McCulloch, and Y. Wu, "Mos2 as a long-life host material for potassium ion intercalation," eng, *Nano res.*, vol. 10, no. 4, pp. 1313–1321, 2017.

[41] K. Xie, K. Yuan, X. Li, W. Lu, C. Shen, C. Liang, R. Vajtai, P. Ajayan, and B. Wei, "Superior potassium ion storage via vertical mos2 "nano-rose" with expanded interlayers on graphene," *Small*, vol. 13, no. 42, p. 1 701 471, 2017.

[42] Y. Dong, Y. Xu, W. Li, Q. Fu, M. Wu, E. Manske, J. Kröger, and Y. Lei, "Insights into the crystallinity of layer-structured transition metal dichalcogenides on potassium ion battery performance: A case study of molybdenum disulfide," *Small*, vol. 15, no. 15, p. 1 900 497, 2019.

[43] S. Imtiaz, I. S. Amiinu, Y. Xu, T. Kennedy, C. Blackman, and K. M. Ryan, "Progress and perspectives on alloying-type anode materials for advanced potassium-ion batteries," *Mater. Today*, 2021.

[44] Z. Yi, N. Lin, W. Zhang, W. Wang, Y. Zhu, and Y. Qian, "Preparation of sb nanoparticles in molten salt and their potassium storage performance and mechanism," *Nanoscale*, vol. 10, pp. 13 236–13 241, 27 2018.

[45] K. Lei, C. Wang, L. Liu, Y. Luo, C. Mu, F. Li, and J. Chen, "A porous network of bismuth used as the anode material for high-energy-density potassium-ion batteries," *Angewandte Chemie International Edition*, vol. 57, no. 17, pp. 4687–4691, 2018.

[46] K. Sakaushi, E. Hosono, G. Nickerl, T. Gemming, H. Zhou, S. Kaskel, and J. Eckert, "Aromatic porous-honeycomb electrodes for a sodium-organic energy storage device," *Nat. commun.*, vol. 4, p. 1485, 2013.

[47] Q. Deng, J. Pei, C. Fan, J. Ma, B. Cao, C. Li, Y. Jin, L. Wang, and J. Li, "Potassium salts of para-aromatic dicarboxylates as the highly efficient organic anodes for low-cost k-ion batteries," *Nano Energy*, vol. 33, Jan. 2017.

[48] B. Lin, X. Zhu, L. Fang, X. Liu, S. Li, T. Zhai, L. Xue, Q. Guo, J. Xu, and H. Xia, "Birnessite nanosheet arrays with high k content as a high-capacity and ultrastable cathode for k-ion batteries," *Adv.Mater.*, vol. 31, no. 24, e1900060–n/a, 2019.

[49] M. Sha, L. Liu, H. Zhao, and Y. Lei, "Review on recent advances of cathode materials for potassium-ion batteries," *Energy Environ. Mater.*, vol. 3, no. 1, pp. 56–66, 2020.

[50] P. Zhu, D. Gastol, J. Marshall, R. Sommerville, and E. K. Vannessa Goodship, "A review of current collectors for lithium-ion batteries," *J. Power Sources*, vol. 485, p. 229 321, 2021.

[51] H. Wang, D. Zhai, and F. Kang, "Solid electrolyte interphase (sei) in potassium ion batteries," *Energy Environ. Sci.*, vol. 13, pp. 4583–4608, 12 2020.

[52] M. Winter, B. Barnett, and K. Xu, "Before li ion batteries," *Chem, rev.*, vol. 118, no. 23, pp. 11 433–11 456, 2018.

[53] T. Yamamoto, K. Matsumoto, R. Hagiwara, and T. Nohira, "Physicochemical and electrochemical properties of k[n(so2f)2]–[n-methyl-n-propylpyrrolidinium][n(so2f)2] ionic liquids for potassium-ion batteries," *J. Phys. Chem. C*, vol. 121, no. 34, pp. 18 450–18 458, 2017, ISSN: 1932-7447.

[54] L. Li, S. Zhao, Z. Hu, S.-L. Chou, and J. Chen, "Developing better ester- and ether-based electrolytes for potassium-ion batteries," *Chem. Sci.*, vol. 12, pp. 2345–2356, 7 2021.

[55] T. Hosaka, K. Kubota, H. Kojima, and S. Komaba, "Highly concentrated electrolyte solutions for 4 v class potassium-ion batteries," *Chem. Commun.*, vol. 54, pp. 8387–8390, 60 2018.

[56] K. Xu, "Nonaqueous liquid electrolytes for lithium-based rechargeable batteries," *Chem. Rev.*, vol. 104, no. 10, pp. 4303–4418, 2004.

[57] T. A. Pham, K. E. Kweon, A. Samanta, V. Lordi, and J. E. Pask, "Solvation and dynamics of sodium and potassium in ethylene carbonate from ab initio molecular dynamics simulations," *J. Phys. Chem. C*, vol. 121, no. 40, pp. 21 913–21 920, 2017.

[58] B. Li, J. Zhao, Z. Zhang, C. Zhao, P. Sun, P. Bai, J. Yang, Z. Zhou, and Y. Xu, "Electrolyte-regulated solid-electrolyte interphase enables long cycle life performance in organic cathodes for potassium-ion batteries," *Adv. Funct. Mater.*, vol. 29, no. 5, p. 1 807 137, 2019.

[59] (2021), [Online]. Available: `https://sop4cv.com/chapters/WhatIsCyclicVoltammetry.html`. (accessed: 8/05/2021).

[60] T. Kim, W. Choi, H.-C. Shin, C. Jae-Young, J. M. Kim, M.-S. Park, and W.-S. Yoon, "Applications of voltammetry in lithium ion battery research," *J. Electrochem. Sci. Technol*, vol. 11, no. 1, pp. 14–25, 2020.

[61] D. A. C. Brownson, D. K. Kampouris, and C. E. Banks, "Graphene electrochemistry: Fundamental concepts through to prominent applications," *Chem. Soc. Rev.*, vol. 41, pp. 6944–6976, 21 2012.

[62] E. Talaie, P. Bonnick, X. Sun, Q. Pang, X. Liang, and L. Nazar, "Methods and protocols for electrochemical energy storage materials research," *Chem. Mater.*, vol. 29, Sep. 2016.

[63] C. Vaalma, G. A. Giffin, D. Buchholz, and S. Passerini, "Non-aqueous k-ion battery based on layered k0.3mno2 and hard carbon/carbon black," *J. Electrochem. Soc.*, vol. 163, no. 7, A1295–A1299, 2016, ISSN: 1945-7111.

[64] L. A. Middlemiss, A. J. Rennie, R. Sayers, and A. R. West, "Characterisation of batteries by electrochemical impedance spectroscopy," *Energy Rep.*, vol. 6, pp. 232–241, 2020, 4th Annual CDT Conference in Energy Storage Its Applications.

[65] M. E. E. Alahi and S. C. Mukhopadhyay, "Interdigitated senor and electrochemical impedance spectroscopy (eis)," in *Smart Nitrate Sensor: Internet of Things Enabled Real-Time Water Quality Monitoring*. Cham: Springer International Publishing, 2019, pp. 43–52.

[66] A. R. B. Samuel Castro Pardo Pavan M. V. Raja, in. 2021.

[67] Q. Zhang, Z. Yu, P. Du, and C. Su, "Carbon nanomaterials used as conductive additives in lithium ion batteries," *Recent Pat. Nanotechnol.*, vol. 4, no. 2, 100–110, 2010.

[68] Y. Chao, "Molybdenum disulfide/carbon composites for lithium ion batteries, doctor of philosophy thesis,"

[69] M. Carboni, A. J. Naylor, M. Valvo, and R. Younesi, "Unlocking high capacities of graphite anodes for potassium-ion batteries," *RSC Adv.*, vol. 9, pp. 21 070–21 074, 36 2019.

[70] L. Deng, Y. Zhang, R. Wang, M. Feng, X. Niu, L. Tan, and Y. Zhu, "Influence of kpf 6 and kfsi on the performance of anode materials for potassium-ion batteries: A case study of mos 2," *ACS applied materials interfaces*, vol. 11, no. 25, p. 22 449, 2019.

[71] B. Jia, Q. Yu, Y. Zhao, M. Qin, W. Wang, Z. Liu, C.-Y. Lao, Y. Liu, H. Wu, Z. Zhang, and X. Qu, "Bamboo-like hollow tubes with mos2/n-doped-c interfaces boost potassium-ion storage," *Adv. Funct. Mater.*, vol. 28, no. 40, p. 1 803 409, 2018.

[72] S. Chong, L. Sun, C. Shu, S. Guo, Y. Liu, W. A. Wang, and H. K. Liu, "Chemical bonding boosts nano-rose-like mos2 anchored on reduced graphene oxide for superior potassium-ion storage," *Nano Ener.*, vol. 63, p. 103 868, 2019.

[73] J. H. Choi, G. D. Park, and Y. C. Kang, "Potassium-ion storage mechanism of mos2-ws2-c microspheres and their excellent electrochemical properties," *Chemical Engineering Journal*, vol. 408, p. 127 278, 2021.

[74] B. Silbernagel, "Lithium intercalation complexes of layered transition metal dichalcogenides: An nmr survey of physical properties," *Solid State Commun.*, vol. 17, no. 3, pp. 361–365, 1975.

[75] L. Deng, Y. Zhang, R. Wang, M. Feng, X. Niu, L. Tan, and Y. Zhu, "Influence of kpf6 and kfsi on the performance of anode materials for potassium-ion batteries: A case study of mos2," *ACS applied materials interfaces*, vol. 11, no. 25, pp. 22 449–22 456, 2019.

[76] Y. Lei, L. Qin, R. Liu, K. C. Lau, Y. Wu, D. Zhai, B. Li, and F. Kang, "Exploring stability of nonaqueous electrolytes for potassium-ion batteries," *ACS applied energy materials*, vol. 1, no. 5, pp. 1828–1833, 2018.

[77] Y. Lei, D. Han, J. Dong, L. Qin, X. Li, D. Zhai, B. Li, Y. Wu, and F. Kang, "Unveiling the influence of electrode/electrolyte interface on the capacity fading for typical graphite-based potassiumion batteries.," *Energy Storage Mater.*, vol. 24, no. 24, pp. 319–328, 2020.

[78] H. Kim, G. Yoon, K. Lim, and K. Kang, "A comparative study of graphite electrodes using the co-intercalation phenomenon for rechargeable li, na and k batteries," *Chem. Commun.*, vol. 52, pp. 12 618–12 621, 85 2016.

[79] M. Liu, L. Xing, K. Xu, H. Zhou, J. Lan, C. Wang, and W. Li, "Deciphering the paradox between the co-intercalation of sodium-solvent into graphite and its irreversible capacity," *Energy Storage Mater.*, vol. 26, Dec. 2019.

[80] Y. Li, K. Leung, and Y. Qi, "Computational exploration of the li-electrode—electrolyte interface in the presence of a nanometer thick solid-electrolyte interphase layer," *Acc. Chem. Res.*, vol. 49, pp. 2363–2370, Sep. 2016.

[81] H. Son, M.-Y. Jeong, J.-G. Han, K. Kim, K. Kim, K.-M. Jeong, and N. Choi, "Effect of reductive cyclic carbonate additives and linear carbonate co-solvents on fast chargeability of lini0.6co0.2mn0.2o2/graphite cells," *J. Power Sources*, vol. 400, pp. 147–156, 2018.

[82] "The electrochemical performance of super p carbon black in reversible li/na ion," *Sci. China Technol. Sci.*, vol. 60, no. 6, pp. 53–60, 2017.

[83] J. Zhou and S. Guo, "Carbon-based anode materials for potassium-ion batteries: From material, mechanism to performance," *SmartMat*, vol. 2, no. 2, pp. 176–201, 2021.

[84] B. Wang, Y. Peng, F. Yuan, a. L. S. Qian Liu, P. Zhang, Q. Wang, Z. Li, and Y. A. Wu, "A comprehensive review of carbons anode for potassium-ion battery: Fast kinetic, structure stability and electrochemical," *J. Power Sources*, vol. 484, p. 229 244, 2021.

[85] Y. Pan, Y. Zhang, B. S. Parimalam, C. C. Nguyen, G. Wang, and B. L. Lucht, "Investigation of the solid electrolyte interphase on hard carbon electrode for sodium ion batteries," *J. Electroanal. Chem.*, vol. 799, pp. 181–186, 2017.

[86] S. Alvin, H. S. Cahyadi, J. Hwang, W. Chang, S. K. Kwak, and J. Kim, "Revealing the intercalation mechanisms of lithium, sodium, and potassium in hard carbon," *Adv. Energy Mater.*, vol. 10, no. 20, p. 2 000 283, 2020.

[87] Y. Li, J. Zhang, and M. Chen, "Mof-derived carbon and composites as advanced anode materials for potassium ion batteries: A review," *Sustainable Materials and Technologies*, vol. 26, e00217, 2020.

[88] L. Zhao, Z. Hu, W. Lai, Y. Tao, J. Peng, Z. Miao, Y. Wang, S. Chou, H. Liu, and S. Dou, "Hard carbon anodes: Fundamental understanding and commercial perspectives for na-ion batteries beyond li-ion and k-ion counterparts," *Adv. Energy Mater.*, vol. 11, no. 1, 2 002 704–n/a, 2021.

[89] J. Yang, Z. Ju, Y. Jiang, Z. Xing, B. Xi, and X. S. Feng Jinkui, "Enhanced capacity and rate capability of nitrogen/oxygen dual-doped hard carbon in capacitive potassium-ion storage," *Adv. mater. (Weinheim)*, vol. 30, no. 4, 1 700 104–n/a, 2018.

[90] W. Wang, Z. Favors, C. Li, C. Liu, R. Ye, C. Fu, K. Bozhilov, J. Guo, M. Ozkan, and C. Ozkan, "Silicon and carbon nanocomposite spheres with enhanced electrochemical performance for full cell lithium ion batteries," *Sci. Rep.*, vol. 7, p. 44 838, Mar. 2017.

[91] R. Wang, H. Mo, S. Li, Y. Gong, B. He, and H. Wang, "Influence of conductive additives on the stability of red phosphorus-carbon anodes for sodium-ion batteries," *Sci. Rep.*, vol. 9, p. 946, Jan. 2019.

[92] J. Li, Y. Lu, T. Yang, D. Ge, D. L. Wood, and Z. Li, "Water-based electrode manufacturing and direct recycling of lithium-ion battery electrodes—a green and sustainable manufacturing system," *iScience*, vol. 23, no. 5, p. 101 081, 2020.